FINAL REPORT

SATELLITE YAW SENSOR STUDY PROGRAM

NASA Contract No. NAS 9-7999

DATE - July 1969 COLL -

BAI CORPORATION
Taylor-Reed Place
Glenbrook, Connecticut 06906
(203) 348-4277

CR-101861

TABLE OF CONTENTS

TABLE OF CONTENTS
(Continued)

TABLE OF CONTENTS
(Continued)

LIST OF ILLUSTRATIONS

LIST OF ILLUSTRATIONS
(Continued)

SECTION 1

INTRODUCTION

1.1 INTRODUCTION

This report describes all of the technical work accomplished by BAI Corporation and its two subcontractors, Barnes Engineering Company and Astro Consultants, Inc., in a feasibility study, preliminary design, breadboard construction and testing relating to the development of a satellite yaw sensor that will measure satellite yaw with respect to the surface of the earth or the moon, in either daylight or darkness.

This program can be thought of as seeking to answer four major questions:

(1) Are there thermal gradients that are adequate for sensor operation under worst case conditions (in earth orbit over the oceans and in lunar orbit at the end of the lunar night)?

(2) What are the requirements for the IR detector; can the feasibility of such a detector be demonstrated?

(3) What are the consequences of the roll rate; can methods be established for eliminating the effect of roll rate on yaw output?

(4) Can a breadboard front end operating in the visible domain be designed, built, and tested in order to establish the efficacy of basic system concepts and demonstrate the ability to achieve the required $1/4^{\circ}$ yaw sensitivity?

The success of the program can be measured by the fact that the answer to all four questions has been shown to be an unqualified yes.

The approaches and results of the program justifying this answer are summarized below:

The infrared yaw sensor operates by sensing transverse movements of thermally contrasting objects across the instrument's image plane. To obtain such thermal contrast of objects, these objects must have a temperature or emissivity difference relative to their backgrounds. To determine whether such thermal gradients would be significant enough to be detectable, two investigations were performed covering the worst casees to be expected on the lunar surface and on earth. On the earth, the worst case occurs when viewing a cloudless expanse of ocean, where thermal gradients are minimized because of the fluidity of the water. On the moon, the worst case occurs just prior to lunar dawn when the lunar terrain is coldest and temperature is lowest.

Studies by Barnes, complemented by BAI studies, indicate that on the lunar surface:

(1) All illuminated surfaces of the moon, including the region near the terminator, have adequate gradients for satisfactory functioning of the yaw sensor.

(2) Results of direct measurements as well as theoretical analyses show that rocks and discontinuities on the lunar surface cool more slowly than the surface itself, and therefore present measurable thermal gradients even at the end of the lunar night. (This conclusion is further supported by BAI analysis that suggests a cosmological basis for a thermodynamic mechanism by which such gradients can exist at the end of the lunar night.)

(3) Successful operation of the yaw sensor at lunar orbit altitudes of as low as 50 miles is expected, due to both the quantity and distribution of the rocks and discontinuities which will provide thermal gradients.

(4). No quantitative data is available regarding the presence of thermal gradients at temperatures below 120°K. It is suggested that high-resolution infrared scanners, if used aboard lunar orbiting vehicles in the Apollo program, would provide valuable design information for the yaw sensor as well as lunar horizon sensors.

Similarly, Barnes' studies indicate that on the earth's surface:

(1) The worst problem expected in orbiting the earth will occur at low altitudes over extended ocean surfaces and under cloudless conditions. Available data indicate that the yaw sensor can function satisfactorily when the $5^{\circ} \times 5^{\circ}$ pyroelectric detector array field of view spans a thermal gradient of about 0.1°C.

(2) Data obtained from TIROS satellites was evaluated to determine the probability of obtaining the above postulated cloudless conditions over an extended ocean surface. This was done to establish effectiveness of yaw sensor operation in cases where ocean thermal gradients are less than 0.1°C. For earth latitudes from 30° north to 25° south, averaged over a monthly basis, the TIROS data indicate that there is no area where an essentially cloudless condition exists. The isolated instances where the yaw sensor will view cloudless skies over an extended ocean surface are expected to persist for less than 1/10 of

an orbit. (Private communication between BAI and ESSA and several recent unpublished analyses suggest that even this conclusion of Barnes may be thought of as unduly pessimistic. For example, analysis of MRIR and HRIR data suggests that the likelihood of finding cloudless areas of sufficient magnitude as to create a yaw measurement problem is extremely low.)

The Barnes Engineering Company has generated a design for an infrared front end whose calculated Noise Equivalent Temperature Difference (NEΔT) is 0.11°C RMS (using a pyroelectric detector array), which is nine times better than the NEΔT calculated for the original proposal. Further, they have fabricated samples of some of the more critical components.

Analytic studies by Mr. Sam Pines of Astro Consultants, Inc., including computer simulation, have established that the natural roll rate of the satellite under orbital conditions has a negligible effect on yaw sensor output. Only during the execution of a satellite roll correction is there a potential influence of roll rate on yaw sensor performance. (Even this effect may well be too small to influence yaw sensor performance.) In view of the comparative infrequence and short duration of such correction, blanking of the yaw sensor during such a maneuver would be the simplest technique for eliminating any potential roll rate effect.

BAI has designed and built a breadboard front end operating in the visible domain that has demonstrated 1/8-degree sensitivity (compared to the required 1/4 degree).* In addition, BAI has designed, built, and tested breadboard versions of an improved solid-state correlator and a solid-state memory, which when incorporated in the processing electronics should further improve sensitivity.

1.2 STATEMEMENT OF WORK

1.2.1 BAI Corporation Effort

(1) Analytical Study

a. Study total system parameters including optical angular coverage, sweep rate, and total system resolution.

b. Study the effects of crosstalk due to roll rate and study methods for minimizing these effects. Produce block diagrams for a system in which roll rate effects are removed.

*Further testing, with more refined equipment, is expected to demonstrate that the actual sensitivity is significantly better than 1/8 degree. (The results of this additional testing will be the subject of a supplement to this report.)

(2) Experimental Phase

a. Design and build a visible light version of multiplexed front end using parameters determined from above study.

b. Operate the above designed front end on test stand to determine:

1) Static resolution of crosstrack displacement

2) Minimum yaw resolution under simulated orbital velocity conditions

3) Effect of forward motion rate and signal-to-noise ratio on system resolution and accuracy

4) System response time to step inputs as a function of signal-to-noise ratio, forward motion, etc.

(3) Engineering Summary and Analysis

a. Establish preliminary block diagram and layout.

b. Establish preliminary size, weight, reliability, and power requirements.

c. Establish the parameters to define the electrical and mechanical interfaces between the Barnes and BAI equipment.

d. Prepare a final report including work done by Barnes Engineering.

1.2.2 Barnes Engineering Co. Effort

(1) Investigate radiance variations on lunar and earth surface for both day and night. Review data from NASA Goddard (TIROS), ESSA, and Lowell Observatory, Flagstaff, Arizona.

(2) Produce preliminary design of optical head including layout and block diagrams. Evaluate fabrication problems of wedge-optic and detector array.

(3) Using characteristics of above design, generate sensitivity calculation to show that instrument is capable of sensing thermal gradients obtained.

(4) Establish size, weight, and power consumption of optical head.

(5) Define the Barnes-BAI interface specifying signal voltage and current output of the 20 element sequential sampler.

(6) Indicate trade-off of weight and aperture size vs. sensitivity.

1.3 SCOPE OF REPORT

This report is divided into four major sections: Section 1 is an introduction, summarizing the problems to be considered in this feasibility study and summarizing the results obtained. Section 2 describes the basic operation of the yaw sensor. As background, the BAI True Area Correlator (BAI-TAC), which forms the basis of the yaw sensor design, is described. This section then describes the operation of the yaw sensor and the derivation of its major parameter values. Section 3 is a detailed discussion of the major tasks of the program, including the tasks assigned to our two subcontractors, Barnes Engineering and Astro Consultants. Section 4 summarizes the results obtained during the program, contains a preliminary system block diagram, provides estimates of expected system performance, reliability, and configuration, and summarizes the conclusions suggested by the results and work on this program.

SECTION 2

BASIC SYSTEM OPERATION

2.1 BAI TRUE AREA CORRELATOR

The core of the yaw sensor is an adaptation of the basic BAI True Area Correlator (BAI-TAC), an electro-optical pattern matching or correlating device in which an optical scanner and an electronic correlator are married to develop the capability of "memorizing" a scene using either visible light or infrared. By means of the correlator, the memorized information can be compared to scenes that are viewed at a later time. This comparison yields the degree of correlation and also relative orientation of the new scene with respect to the one that was memorized.

In its standard instrumentation, the BAI-TAC consists of three basic elements:

(1) A scanner assembly that scans an area on the ground and converts the viewed scene into an electrical analog. This analog can be considered the "signature" of the viewed area. The scanner assembly consists of imaging optics, a scanner, a detector, and associated processing circuitry.

(2) A memory system that can store one or more such "signatures".

(3) A correlator that compares two such "signatures" for degree of similarity. The output of the correlator is an error signal that indicates the magnitude and relative phase of any mismatch between the two "signatures". This is directly convertible into displacement information normally resolved into three components: X, Y, and θ (yaw).

The basic elements of the BAI system (when instrumented to provide an annular scan, which is its most typical configuration) are shown in Figure 2.1. The moving aperture of the scanner passes a portion of the energy (flux) of the image formed by the imaging optics. The energy passing through the slit is collected and focused on a detecting element. As the image varies in intensity, the flux passing through the aperture varies proportionally; this variation is sensed by the detector, producing a video rate electrical analog of the energy variations in the area of the image scanned. This video signal, when processed, is a quantized modulated pulse train called a scene analog whose pulse spacing and duration depend upon the characteristics of the original video signal.

When two scene analogs are compared by the correlator, the correlator output is normally presented in the form of voltages that are proportional to the

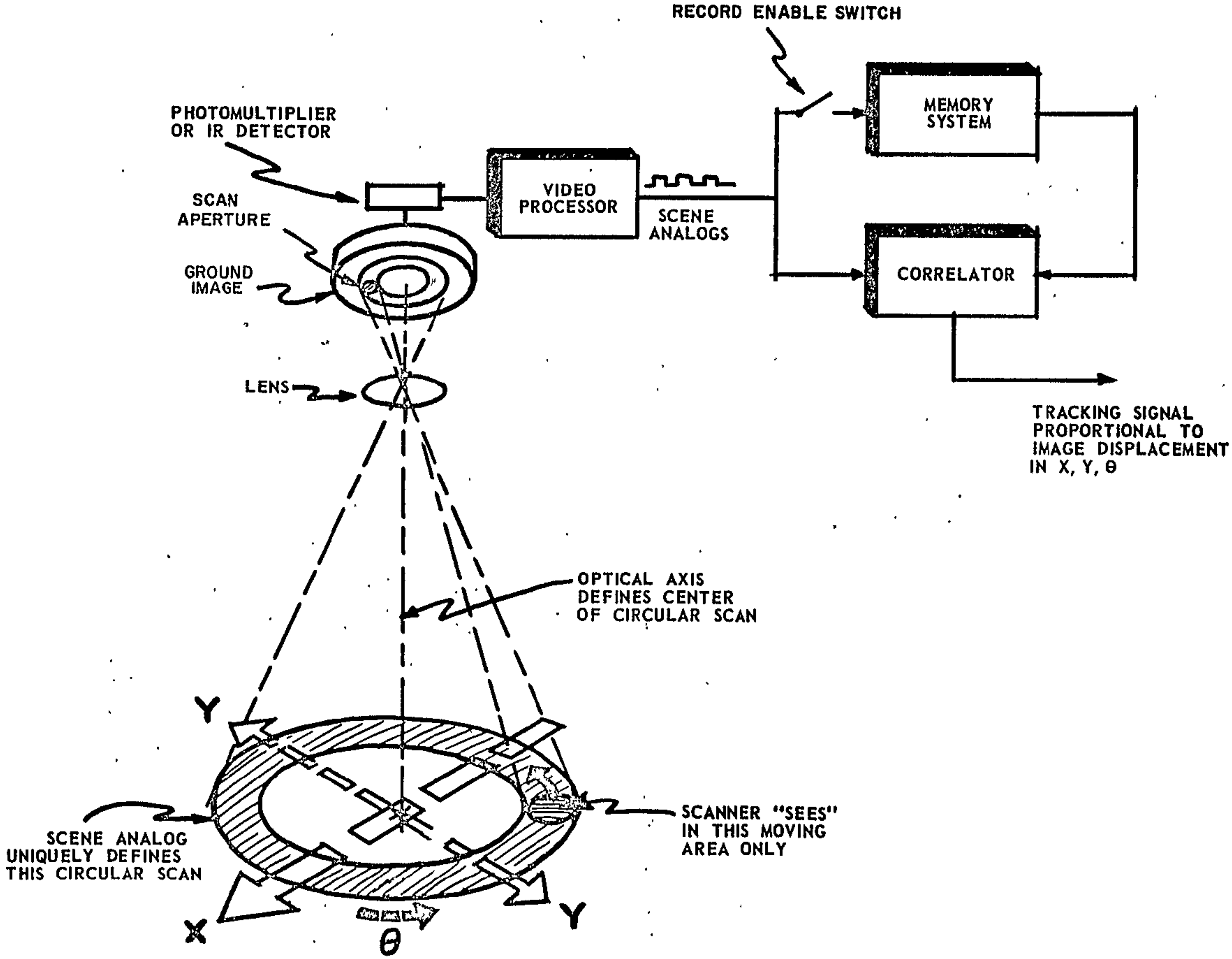

Figure 2.1. BAT-TAC, Simplified Block Diagram ("Standard" Annular Scan Shown)

displacements between the two scenes. If there is no displacement between the two scenes, that is, if they coincide perfectly, the output of the correlator will be zero.. Displacements of as little as one micron (40 microinches) in the image plane will generate error signals that can be used to control a closed loop servo.

2.2 USE OF THE BAI-TAC TO MEASURE ANGULAR RATE OF MOTION

The BAI-TAC output signal is a time-varying signal representing the direction and magnitude of image displacement in the scanner plane. By phase detecting this output signal with respect to some arbitrary axes, we can resolve it into two orthogonal components that we may call X and Y displacements. In V/H applications one of the axes is chosen so that it is parallel to the vehicle heading (providing forward displacement), and the other axis is parallel to the vehicle pitch axis (providing lateral displacement or crab angle).

2.3 BASIC YAW SENSOR OPERATION

2.3.1 Introduction

Since only one of the above mentioned displacement components is required for the yaw sensor, it is possible to design a variation of the standard BAI scanner such that the desired output is isolated in the video as it is originally generated. This requires a scan that is effectively linear in the direction of the displacement to be measured. BAI had previously developed such a scanner for operation with a photomultiplier in the visible domain. The yaw sensor scanner is based on this concept, but modified in implementation to allow use of uncooled infrared detectors.

2.3.2 Scanner-Detector

The requirement that the yaw sensor operate on both the light and dark side of the moon and earth predicates the use of an infrared detector. Since uncooled IR detector elements are quite slow, a mechanical scanner used with a single detector would have too slow a response to be of use in a practical V/H or yaw measuring system. If, however, an array of detectors is allowed to look out at the world continuously, and the outputs are then sampled by means of a multiplexer, a relatively high speed scan can be used even with quite slow speed detectors.

Therefore, the yaw sensor system uses a scan technique that conceptually is almost identical to linear scanners built by BAI as a variation of the BAI standard annular scanner, but modified in mechanization to take advantage of the basic differences (particularly in response time) between IR detectors and visible light photomultipliers. We have used an array of IR detectors electronically multiplexed, thus providing the concomitant advantage of eliminating mechanical motion, motors, bearings, lubrication problems, etc.

2.3.3 Correlator and Memory

The electronic processing used in the yaw sensor system is very similar to the processing used so successfully in previous BAI area correlators. The block diagram of the processor differs little from that of past correlators. One major difference in design and instrumentation is in the memory technique. Further, integrated circuits in place of discrete components enhance performance and reliability.

Previous BAI area scanner-correlators, typically the V/H sensor system used with such conspicuous success on the Lunar Orbiter, used a magnetic memory drum mounted on the same motor shaft as the mechanical scanner to obtain phase coherence between the information being read from memory and the real-time information being read by the scanner.

Since the yaw sensor requires no rotating components, a solid-state memory of suitable length and resolution to store the memorized scene analog without loss in sensitivity or accuracy due to quantizing is used. Our past experience has shown that when scanning through 360^{o} with an aperture of roughly 3^{o}, we must resolve approximately one part in 10,000. This corresponds to resolving approximately 100 elements in the processing for each aperture width. Extrapolating from this, we have designed a memory system with 100 resolution elements in the processing electronics for each aperture width in the scanner, which means that for 20 elements in the scanning mosaic, we require approximately 2,000 resolution elements in the memory.

Thus, in terms of the block diagram, the system corresponds to the systems built by BAI in the past with the exceptions noted above, that is, that the phase-sensitive detectors required for resolving the error signal into its orthogonal components have been eliminated,* the rotating drum memory is replaced by a solid-state memory that has comparable resolution, and integrated circuits replace discrete components.

The design philosophy followed in this program has the advantage of incorporating a technology that has been proven in existing BAI area correlators and scanners, but eliminating the need for any moving parts without requiring a development of new components or new component technology. It is an approach that salvages all of the known advantages of previous BAI

*Since only the component of the image motion showing yaw is required.

systems and adds to these the strong advantages of small, low power, high reliability, all solid state, integrated circuit components. The use of high reliability integrated circuits in place of the previously used rotating drum memory and the discrete component correlator has the additional advantage of enhancing system performance by reducing the noise contribution of these two system components. (This is discussed in more detail in Sections 3.3, 3.7, and 3.8.)

2.4 OPERATING PARAMETERS

Basic operating parameters of the yaw sensor were established in the original BAI proposal. The underlying design philosophy for the yaw sensor involved modeling it as far as possible upon standard BAI scanner-correlator designs, particularly the Lunar Orbiter V/H sensor instrumentation. This allowed us to make use of all the then extant BAI correlator technology and predict yaw sensor performance by analogy to existing BAI systems. Thus, we could have a high degree of confidence that the yaw sensor built on such design bases would perform quite closely to that predicted; this indeed turned out to be the case.

The following paragraphs summarize the development of basic operating parameters given in the proposal.

2.4.1 The IR Detector Array

The scanner upon which the IR detector array is modeled is equivalent to the pertinent portion of a rotating disk that scans an annular region in the focal plane of an optical system corresponding to scanning an annular region on the ground that has an included angle of 15° with an excluded center portion of 5°. (See Figure 2.2.) By noting that the two opposite quadrants of the annulus centered on the cross-track axis provide the along-track motion (the two quadrants being redundant) and the other two quadrants, the cross-track motion and further that both the information content of the signal generated by the scan as well as the error resolving circuitry are cosine functions, it is seen that 90% of the cross-track motion is measured in the 45° sectors centered on the line of flight. (The distribution of information is illustrated in Figure 2.3.) Among the advantages obtained from using this small a segment of the annulus is that in this smaller sector, a roughly linear relationship exists between the time displacement of the electrical signal and the spatial displacement of the scanned image. This linearity significantly reduces complexity in signal processing and allows the use of simple shift registers or similarly simple systems for the memory functions.

As shown in the proposal, the 45° sector corresponds to an included angle of view of 5° while the along-track dimension of the sector is the same as for

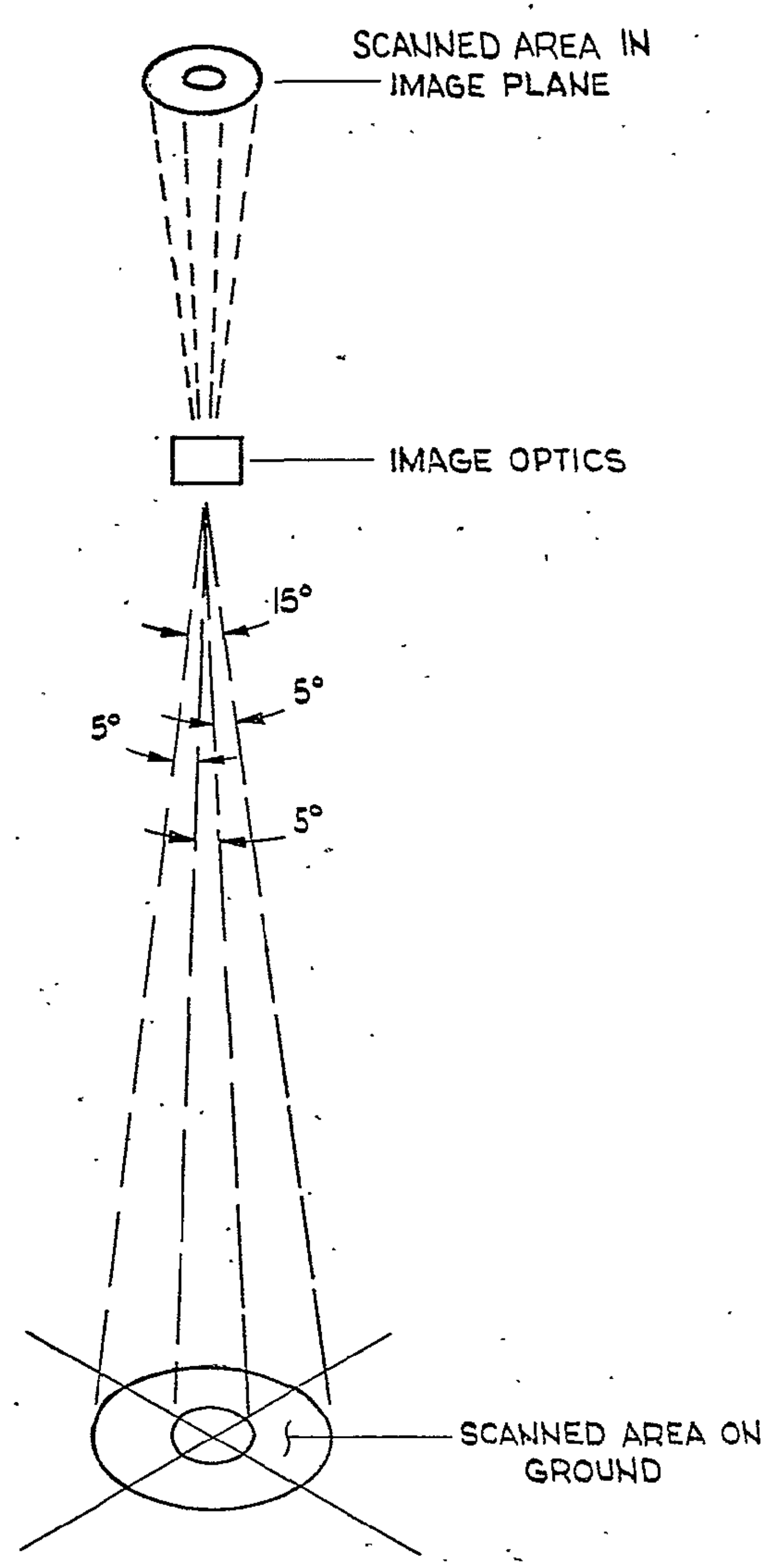

Figure 2.2. Annular Scan Chosen as "Base Reference" for Determining Yaw Sensor Parameters by Extrapolation

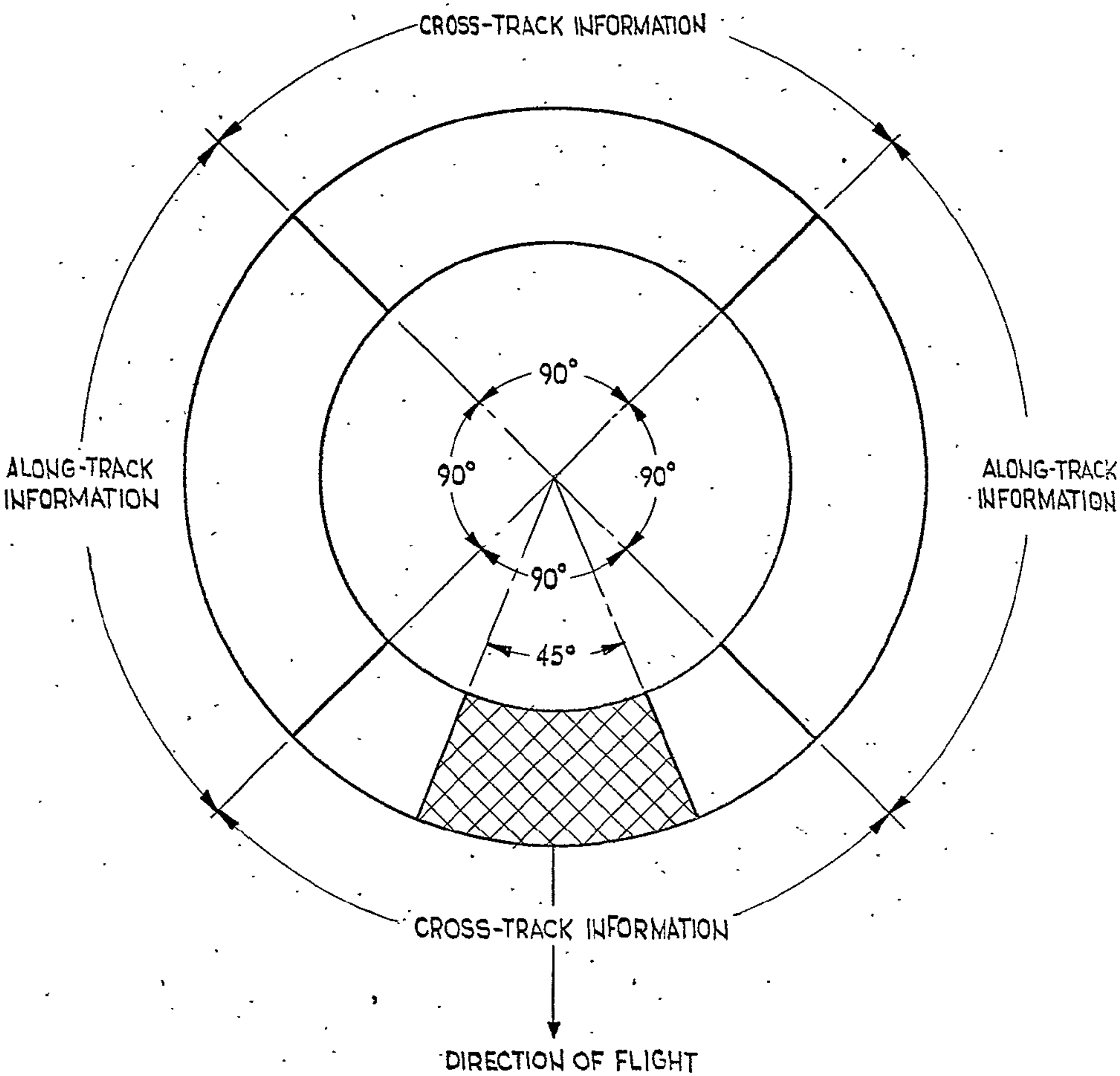

Figure 2.3. View of Scanned Area of Image Plane Showing Information Content of Basic Annular Scan

the basic annulus, namely, an included angle of 5°. Hence, we arrive at a basic scanner configuration with a subtended angle of 5° x 5°. If we divide the scanner into 20 static elements, each element having 1/4° subtended angle, we then have a reasonable synthesis of the type of scanning aperture used typically on the Lunar Orbiter system, substituting 20 separate detectors that are multiplexed for a single, continuously moving aperture (see Figure 2.4).*

The choice of a 5° length for the individual detector elements is based on the amount of forward vehicle motion that can be allowed before decorrelation between the new and the memorized information becomes too great to generate a usable correlation signal. Correlation can be maintained with an image displacement in excess of 10 percent of the image area, so we can easily track an image while it moves 0.5° in the along-track direction. It is during this period of tracking that cross-track motion can be measured.

2.4.2 Scanning Rate

The scanning rate of the yaw sensor system is selected to be the same as the Lunar Orbiter system. In Lunar Orbiter, a 10-millisecond scan was used. In the yaw sensor system, the IR detector mosaic is multiplexed at a 2-kc rate. Since the mosaic has 20 elements, each of its elements is also sampled every 10 milliseconds. This scanning rate represents a sound engineering compromise between signal-to-noise considerations, multiplexing problems, speed of response of the detector elements, and required response time of the sensor itself.

2.4.3 System Sensitivity

Under worst case conditions (particularly in regard to the minimum temperature differential that will be experienced and the tracking distance), the proposal predicted a yaw sensitivity of 0.25°. (In actual operation under most conditions

---

*A standard annular scanner of this sort as made by BAI would have a scanning aperture of about 3°, providing 15 resolution elements within the 45° portion of the total scan. Using 20 separate detectors to cover a comparable area results in a quantizing effect which, according to Shannon's Sampling Theorem, introduces a loss of resolution of at least a factor of 2. If we wish to be very conservative, we can postulate a resolution loss of as much as 4. Therefore, if we consider resolution elements to be equivalent to a discernible aperture displacement in the standard, continuously moving aperture version, we have 20/4 or 5 resolution elements. Thus, there is a difference in resolution of a factor of 15/5 or 3 in favor of the standard BAI scanner. The effect of this on system performance is considered below.

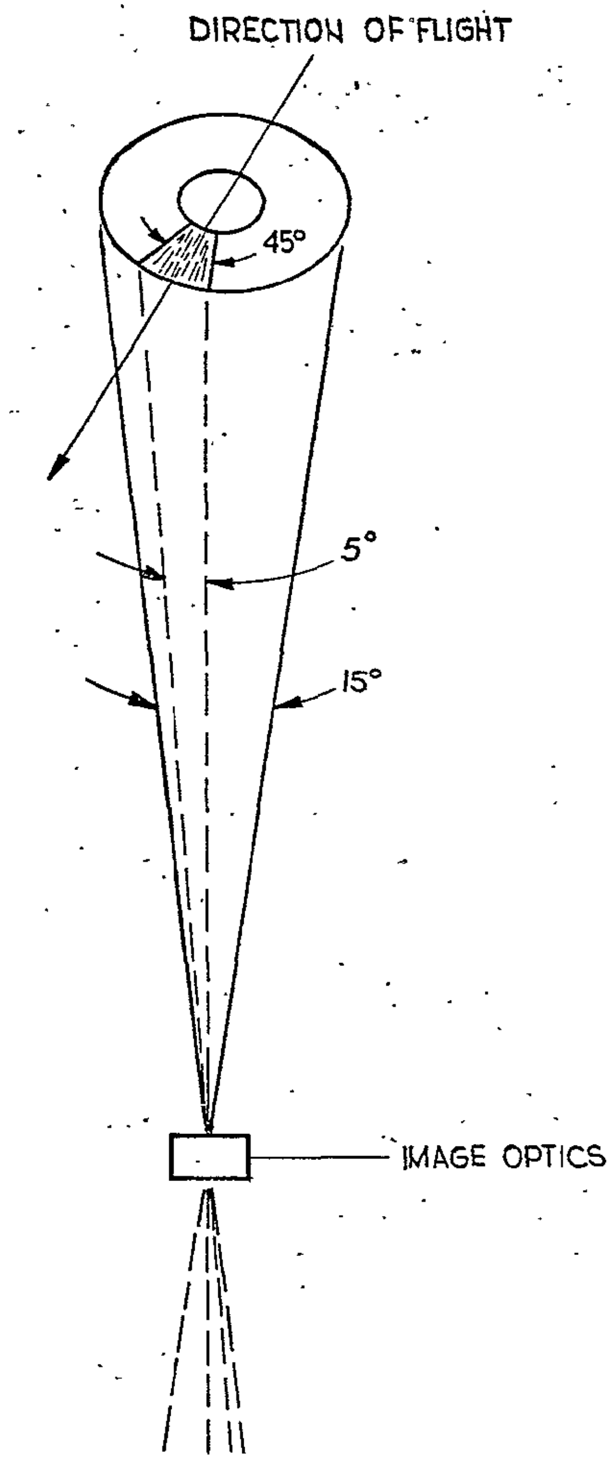

Figure 2.4. 45° Sector of Annulus Divided into 20 Elements

significantly better sensitivity can be expected.) This sensitivity was extrapolated from that of known systems, particularly the Lunar Orbiter wherein 1 micron displacements were detectable in the image plane; laboratory testing of the breadboard indicates that this prediction was quite conservative.

Parameter differences between the yaw sensor and Lunar Orbiter system affecting resolution are signal-to-noise ratio and aperture resolution. The yaw sensor S/N level at the output of the video preamplifier is 10 times lower than that of the Lunar Orbiter, resulting in a 2.5 times loss in sensitivity as determined by laboratory data. Aperture resolution is 3 times worse. Hence, the yaw sensor is 2.5 x 3 = 7.5 times less sensitive than the Lunar Orbiter sensitivity of 1 micron, resulting in a yaw sensor sensitivity of 7.5 microns at the image plane. With a lens system of 8-1/2 inch focal length, and knowing that we can track an image during an along-track displacement of 0.5° without decorrelation, the proposal demonstrates that a 7.5 micron resolution at the image plane is equivalent to a yaw sensitivity of approximately 0.25°. Test results with the breadboard visible-light system demonstrates a system sensitivity of at least $1/8^{\circ}$. (More stringent testing using an improved memory is expected to demonstrate that the sensitivity is a good deal better than this. Data resulting from this testing will be submitted as a supplement to this report.)

SECTION 3

DETAILED DISCUSSION OF PROGRAM

3.1 INVESTIGATION OF TARGET RADIATION CHARACTERISTICS*

In evaluating the feasibility of developing an infrared yaw sensor that produces informational outputs from sensed radiation gradients, the target characteristics must be known or at least accurately estimated. In particular, it is the worst-case radiation gradient in conjunction with the angular subtense of each of the sensor's 20 elemental fields of view ($0.25^\circ \times 5^\circ$) that set the criterion. In the course of the program, the literature relating to the thermal characteristics of both the moon and earth was surveyed. In addition, consultations were held with Dr. J. Salisbury and Mr. G. R. Hunt of the Lunar and Planetary Research Branch of the Space Physics Laboratory AFCRL, Bedford, Massachusetts.

3.1.1 Lunar Thermal Gradients

The Space Physics Laboratory has conducted and mapped the results of high-resolution scans made across the dark lunar surface from earth-based telescopes. Although telescope resolution was only 8 miles as opposed to the 0.218 mile subtense yielded by a 0.25° sensor element at a 50-mile altitude, the measurements did indicate that, near the terminator, an extremely wide dynamic temperature range exists that encompasses illuminated and shadowed surfaces (Figure 3.1).

Near the terminator, in a linear distance of approximately 160 miles on the lunar surface, the temperature increased from 154°K to 261°K, a range equivalent to a signal ratio of 8:1. With the proposed sensor, this large change in signal would, of course, only be significant at higher orbital altitudes where the field of view covers surface dimensions of 160 or more miles. However, near the terminator in a surface dimension of approximately 16 miles (the spatial subtense of 5° for an orbit altitude of 100 miles), the signal ratio is approximately 1.6:1. Near the subpolar point a gradient of only 1°C occurs in approximately 16 miles (see Figure 3.2). If it is assumed that this is a linear gradient, a difference of only 0.05°C would appear between adjacent 0.25° elemental fields of view. However, these gradients occur for a background temperature near 400°K. At this target temperature, the yaw sensor has a Noise Equivalent Temperature Difference (NEΔT) of $\angle$ 0.001 (see Figure 3.3).

---

*The major portion of Section 3.1 was prepared by Barnes Engineering Co. Complementary additional studies by BAI are described in Sections 3.1.2 and 3.1.4.

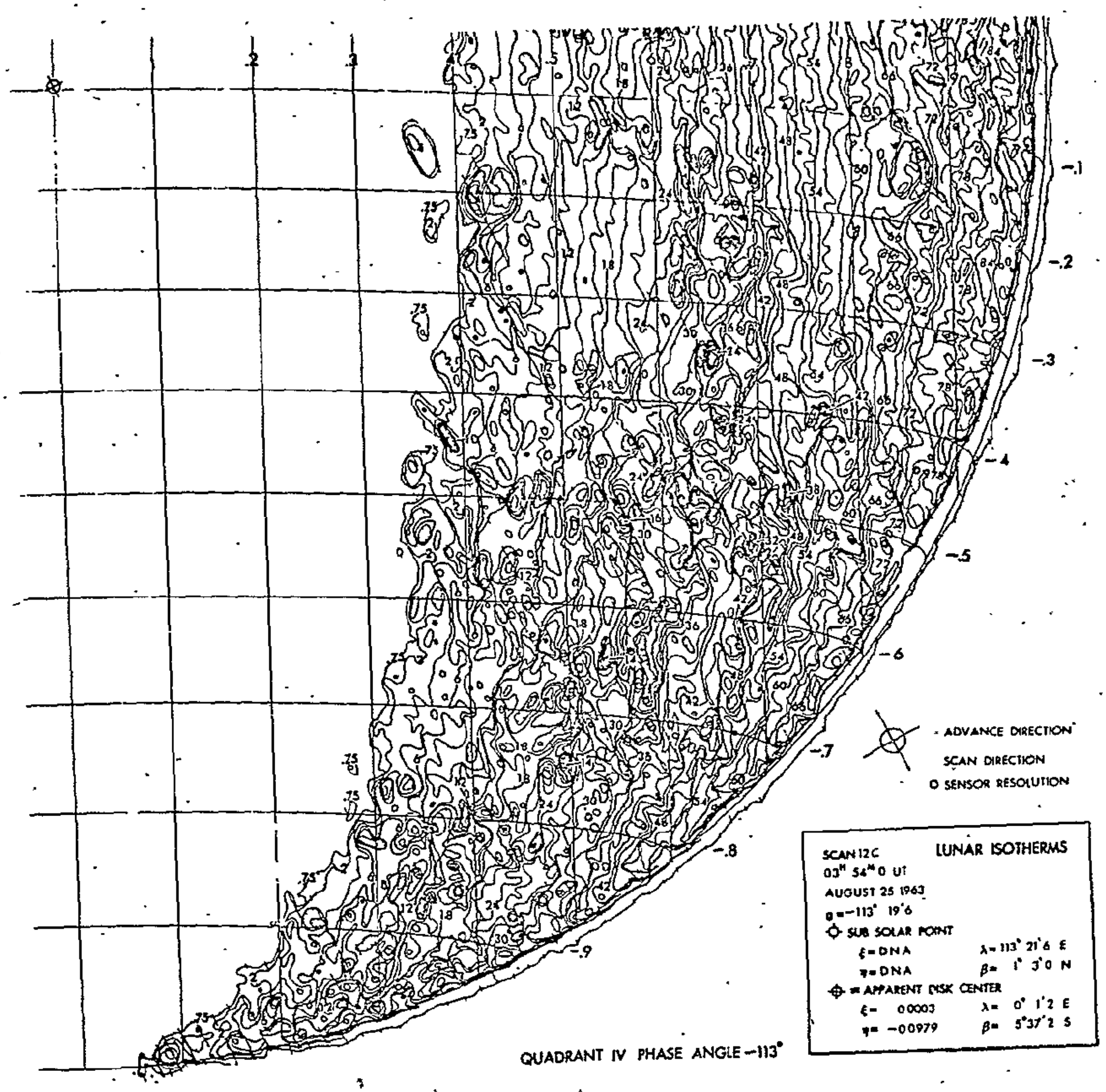

THERMAL CALIBRATION DATA

Contour Number	Temperature °K	Contour Number	Temperature °K	Contour Number	Temperature °K	Contour Number	Temperature °K
.75	154.7	32	277.2	64	324.2	96	359.5
2	174.9	34	280.8	66	326.6	98	361.5
4	192.7	36	284.3	68	329.1		
6	204.9	38	287.6	70	331.4		
8	214.6	40	290.8	72	333.8		
10	222.7	42	294.0	74	336.1		
12	229.8	44	297.1	76	338.3		
14	236.2	46	300.0	78	340.6		
16	242.0	48	303.0	80	342.8		
18	247.3	50	305.8	82	345.0		
20	252.3	52	308.6	84	347.1		
22	257.0	54	311.3	86	349.2		
24	261.4	56	314.0	88	351.3		
26	265.6	58	316.6	90	353.4		
28	269.7	60	319.2	92	355.5		
30	273.5	62	321.8	94	357.5		

Figure 3.I. Lunar Isotherms

(From Saari and Shorthill - "Isothermal and Isophtic Atlas of the Moon: Contours through a Lunation," Boeing Scientific Research Labs., p. 192, Sept. 1967.

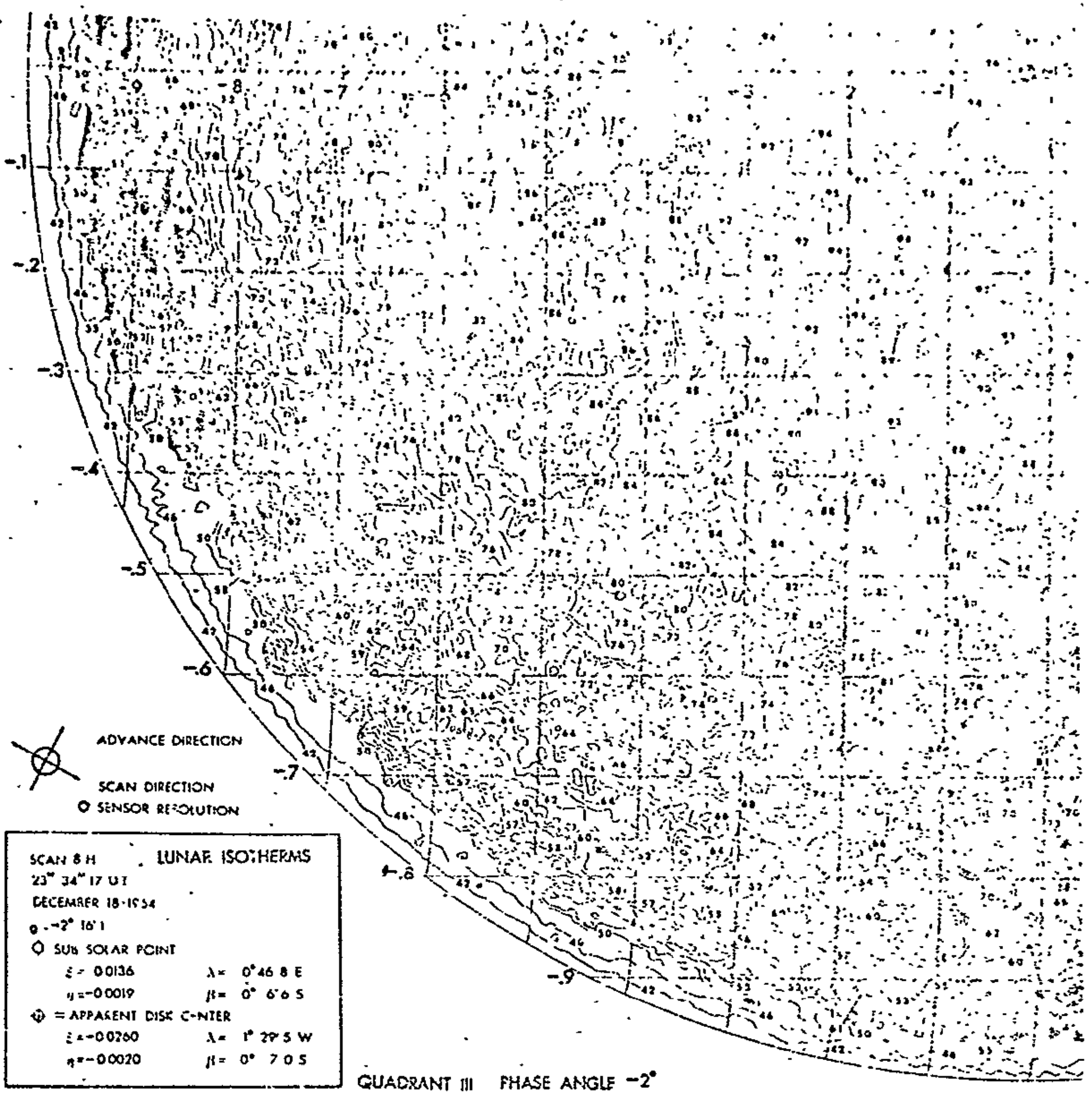

THERMAL CALIBRATION DATA

Contour Number	Temperature °K	Contour Number	Temperature °K	Contour Number	Temperature °K	Contour Number	Temperature °K	Contour Number	Temperature °K
.75	161.7	34	304.1	58	346.2	74	369.3	90	390.2
2	183.9	36	308.2	59	347.8	75	370.[illegible]	91	391.4
4	203.7	38	312.1	60	349.3	76	372.1	92	392.6
6	217.3	40	315.9	61	350.8	77	373.4	93	393.9
*10	237.4	42	319.5	62	352.3	78	374.7	94	395.1
12	245.6	44	323.1	63	353.8	79	376.1	95	396.3
14	252.7	46	326.7	64	355.2	80	377.6	96	397.5
16	259.3	48	330.1	65	356.7	81	378.7	97	398.7
18	265.4	50	333.4	66	358.1	82	380.0	98	399.9
20	271.1	**51	335.1	67	359.6	83	381.3	99	401.1
22	276.5	52	336.7	68	361.0	84	[illegible]	100	402.3
24	281.7	53	338.3	69	362.4	85	383.[illegible]	101	403.[illegible]
26	286.5	54	340.0	70	363.8	86	385.1		
28	291.2	55	341.5	71	365.2	87	386.4		
30	295.7	56	343.1	72	366.6	88	387.7		
32	300.0	57	344.7	73	368.0	89	388.9		

*Note level Number 8 not contoured.

**Note change in levels contoured from Number 51 on.

FIGURE 3.2.2 Lunar Isotherms

(From Saari and Shorthill - op. cit.)

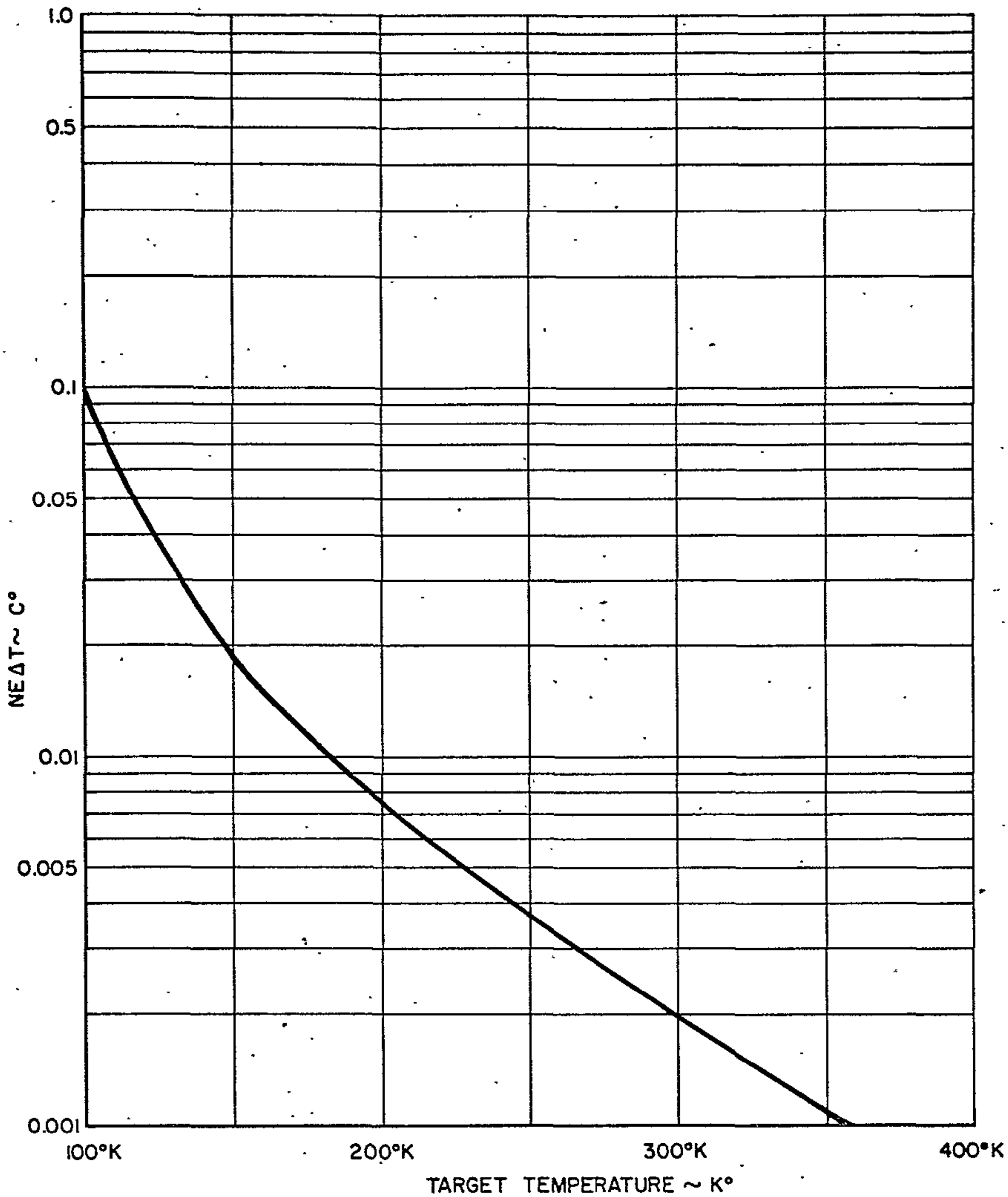

Figure 3.3. RMS NOISE EQUIVALENT TEMPERATURE DIFFERENCE (NEΔT) FOR A 0.25 x 1° BLACKBODY TARGET AT VARIOUS TEMPERATURES

A22389

In regard to thermal gradients over lunar surface dimensions of less than 8 miles, the only available data is that obtained by the Surveyor spacecraft series.

Thermal gradients in the vicinity of the Surveyor spacecraft landing site during the lunar night were very coarsely estimated by calculating the radiant heat exchange between the lunar surface and two thermal compartments located within 120^{o} about the spacecraft's vertical axis. The temperatures of these thermal compartments were monitored through the lunar night, and the results of these measurements are shown in Figures 3.4 and 3.5, which were obtained from "Surveyor VI Mission Report, Part II: Science Results," JPL Technical Report 32-1262, January 10, 1968. As discussed above, these telemetered measurements do not represent exact quantitative data. However, one of the conclusions that was drawn by the Surveyor experimenters has direct applicability to the yaw sensor; i.e., there are rocks on the lunar surface that cool more slowly than the surrounding surface.

Additional support for this conclusion is borne out experimentally by the lunar thermograms taken by Salisbury and Hunt.* In their experiment, the crater was scanned up to 97 hours after lunar sunset and showed a significant thermal contrast to its background. See Figures 3.6, 3.7, and 3.8. A theoretical analysis also supports this conclusion, as is shown in Figures 3.9 and 3.10.

In view of the above discussion, the following conclusions relative to the presence of gradients on the lunar surface can be drawn.

(1) In the region near the terminator and on all the illuminated surfaces of the moon, gradients adequate to allow the yaw sensor to function satisfactorily do exist.

(2) Although no direct lunar radiometric measurements with elemental surface resolutions of less than 8 miles have been conducted, results from the Surveyor VI spacecraft and other theoretical analyses indicate that rocks and discontinuities on the lunar surface cool more slowly than the surface after sunset and would therefore present a thermal gradient. (See Section 3.1.2 for a cosmologically based discussion supporting this conclusion.)

(3) The quantity and distribution of lunar rocks and small discontinuities are sufficient to produce the spatial gradients and therefore thermal gradients that will allow successful operation of the yaw sensor at lunar orbit altitudes as low as 50 miles. (See Figure 3.11.)

---

*"Infrared Images of TYCHO on the Dark Moon," J. W. Salisbury and G. R. Hunt, Science, Vol. 155, pp. 1098 - 1100, 1967.

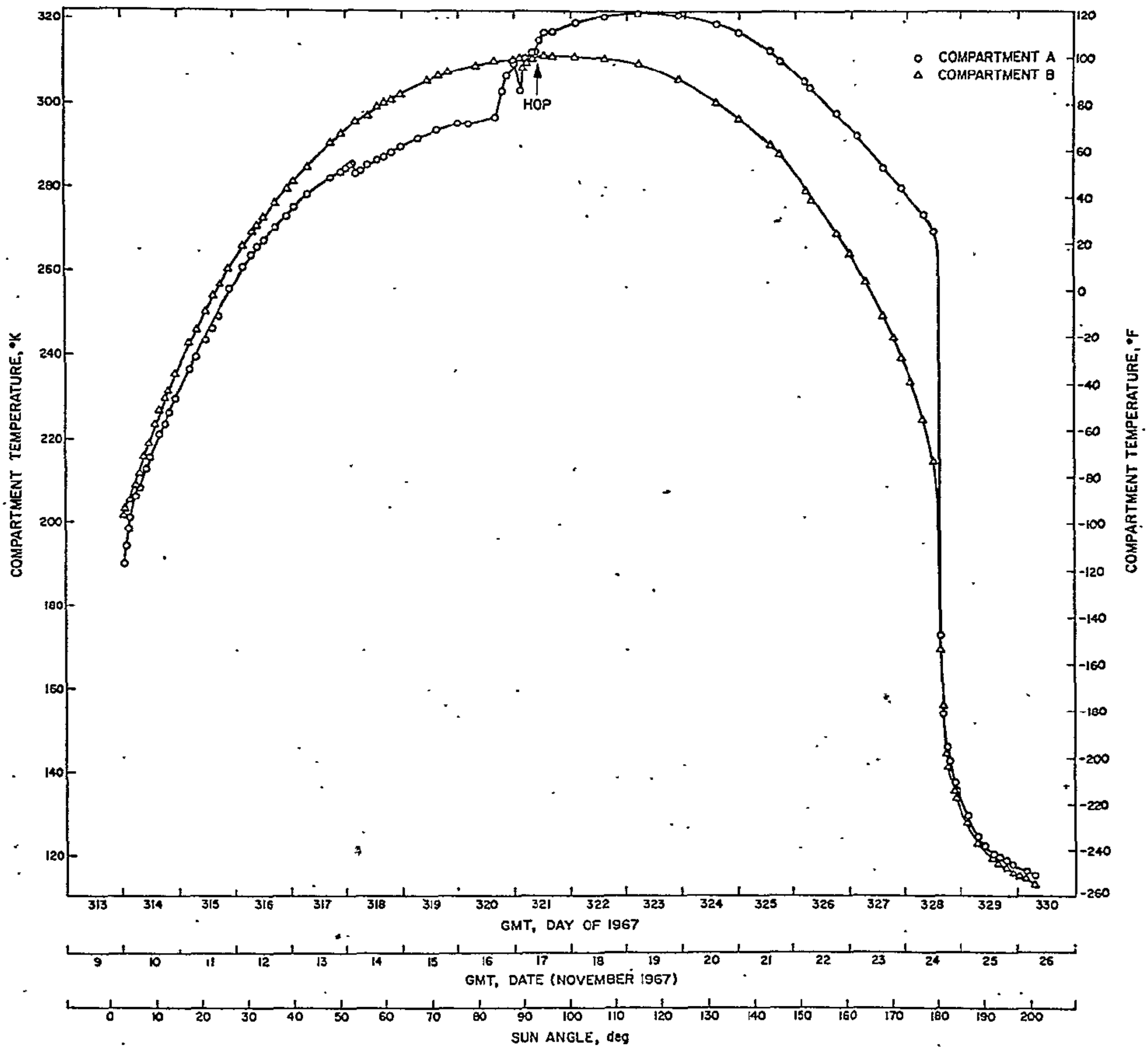

Figure 3.4. **Temperatures of outboard faces of compartments A and B,** Surveyor VI

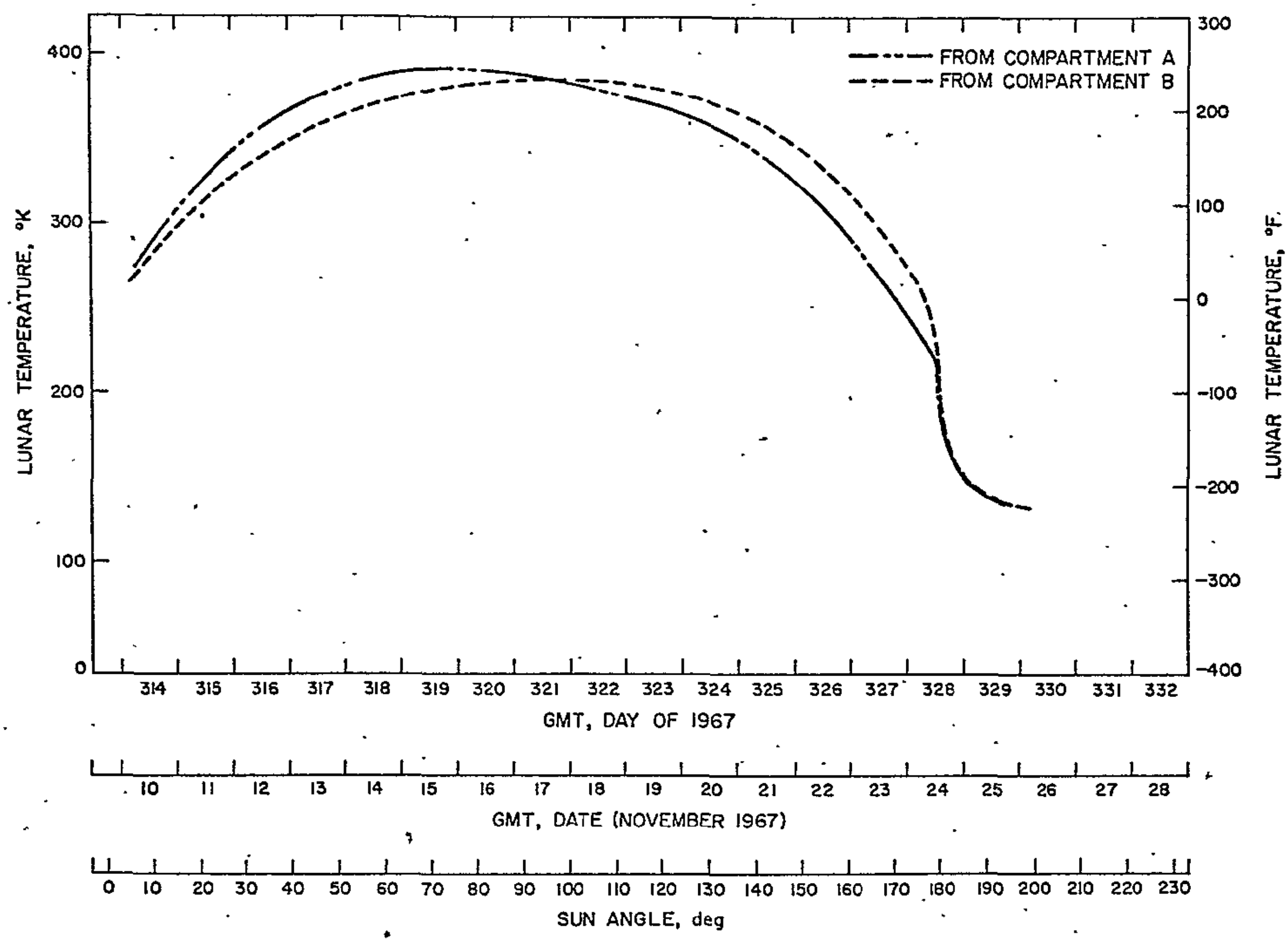

Figure 3.5.7 **Lunar surface brightness temperatures, as calculated from compartment A and B telemetry data,** Surveyor VI

JPL TECHNICAL REPORT 32-1262

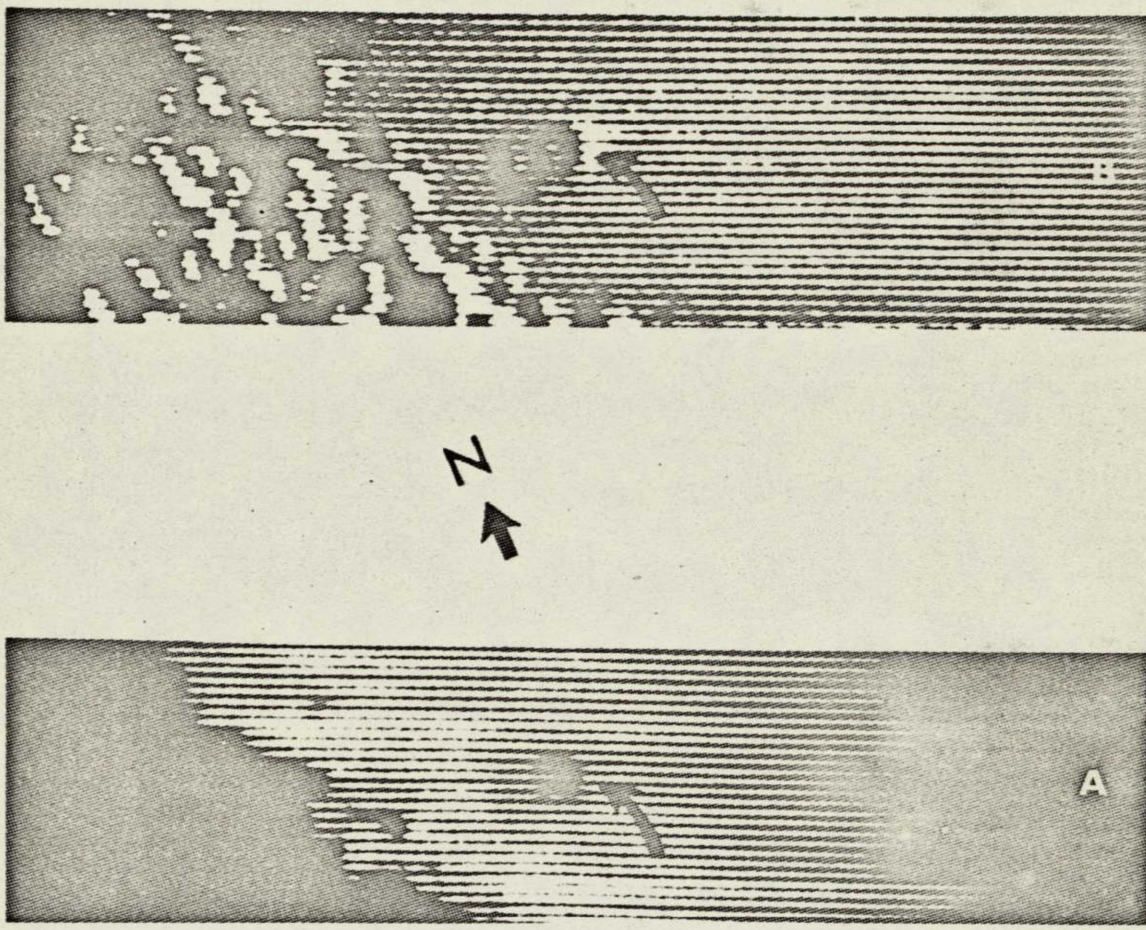

Figure 3.6. Infrared images of Tycho (curved arrow) obtained on 8 October 1966. Image A was produced using conventional radiometric techniques at 1003 U.T. Image B was produced using a thermal enhancement technique at 0946 U.T. Tycho had not been illuminated for approximately 22 hours.

(From Salisbury and Hunt - op. cit.)

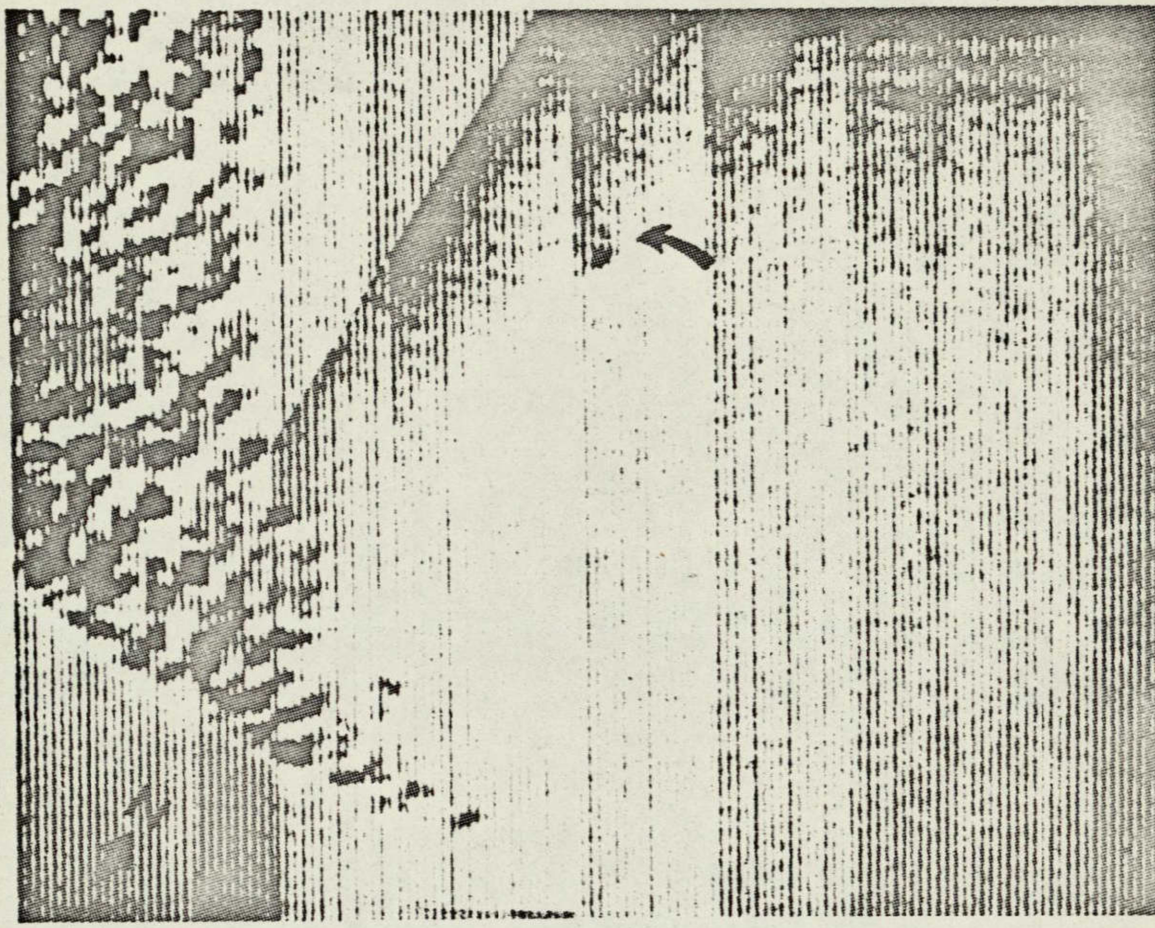

Figure 3.7. A mosaic of 2 infrared images showing both Tycho (curved arrow) and the terminator. The images were obtained on 9 October 1966 using a thermal enhancement technique. The image on which Tycho is shown was produced 0958 U.T., when Tycho had not been illuminated for approximately 46 hours.

(From Salisbury and Hunt - op. cit.)

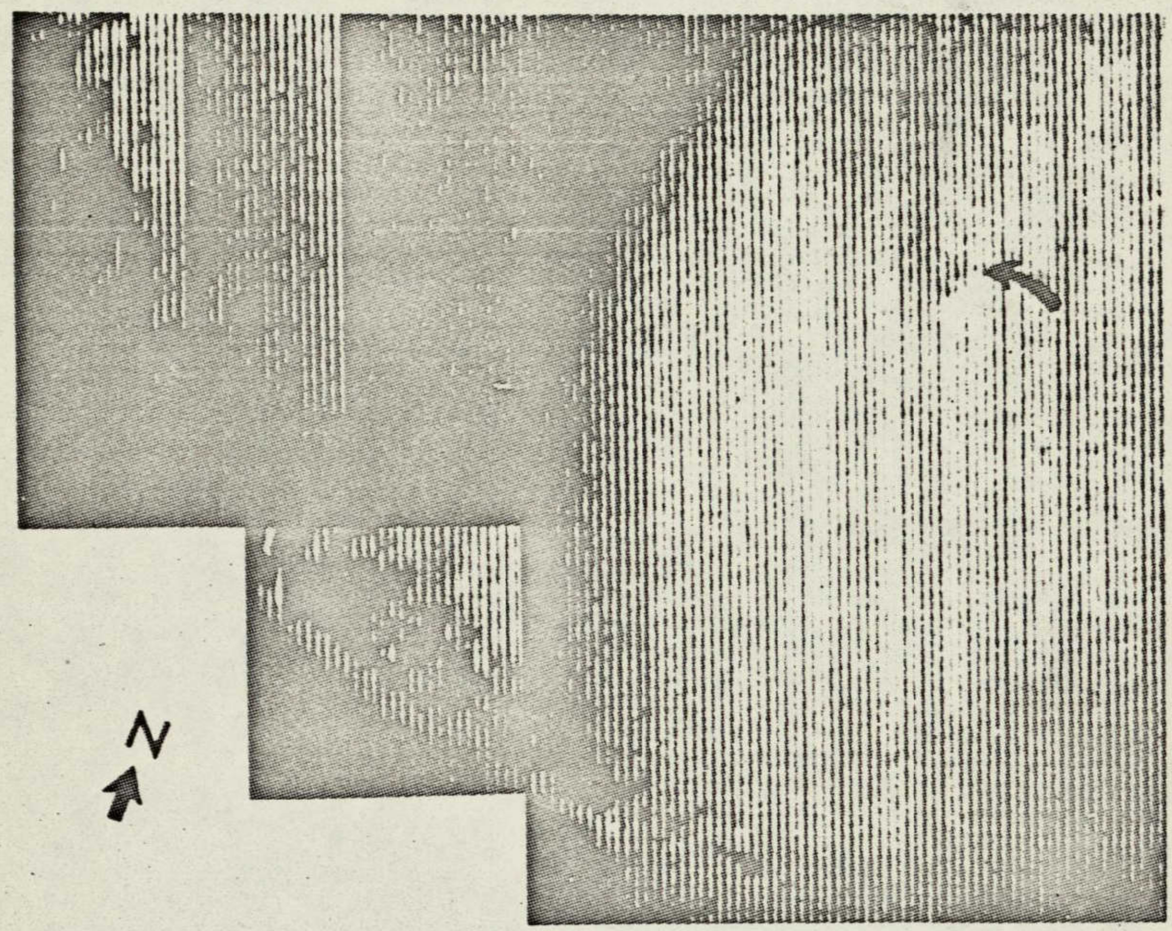

Figure 3.8. A mosaic of 3 infrared images showing both Tycho and the terminator. The images were obtained on 11 October 1966 using a thermal enhancement technique. The image on which Tycho is shown was produced at 1220 U.T., when Tycho had not been illuminated for approximately 97 hours.

(From Salisbury and Hunt - op. cit.)

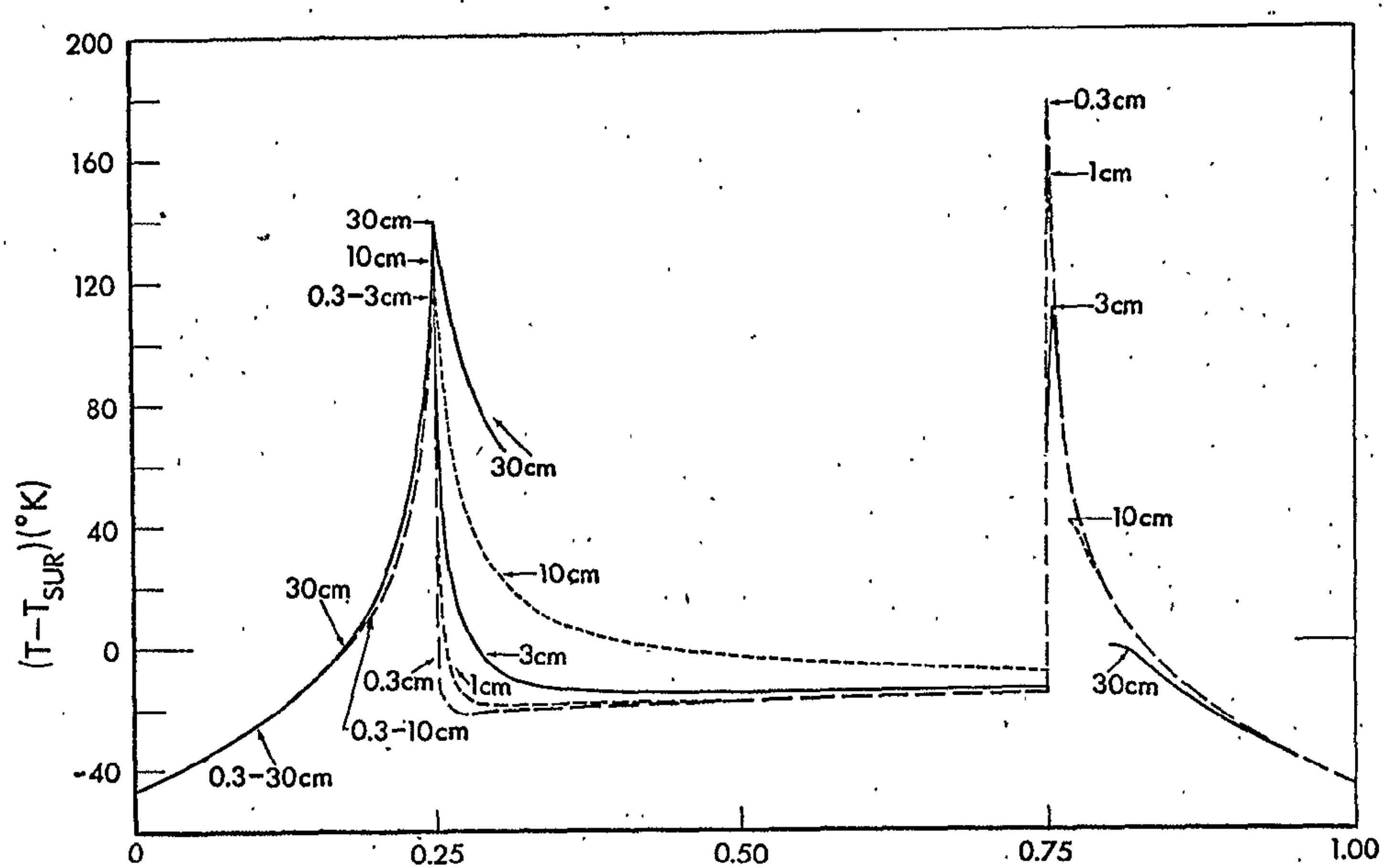

Figure 3.9. Difference between small rock temperature T and surface temperature T_{sur} of a region on the lunar equator during a synodic month (after Roelof, 1968).

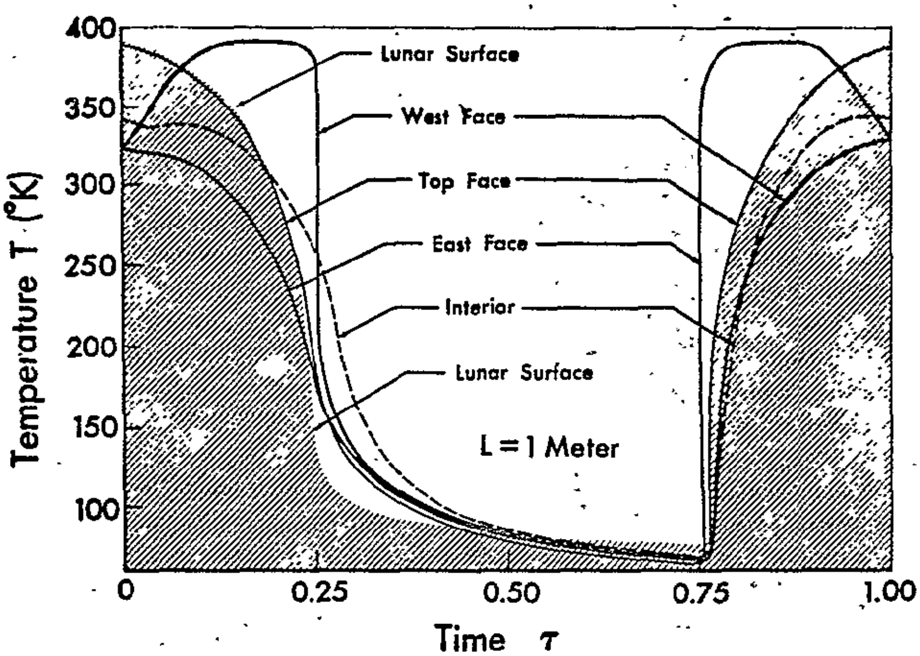

Figure .3.10. Thermal history of a 1 meter basaltic cube on the lunar equator during a synodic month (after Roelof, 1968).

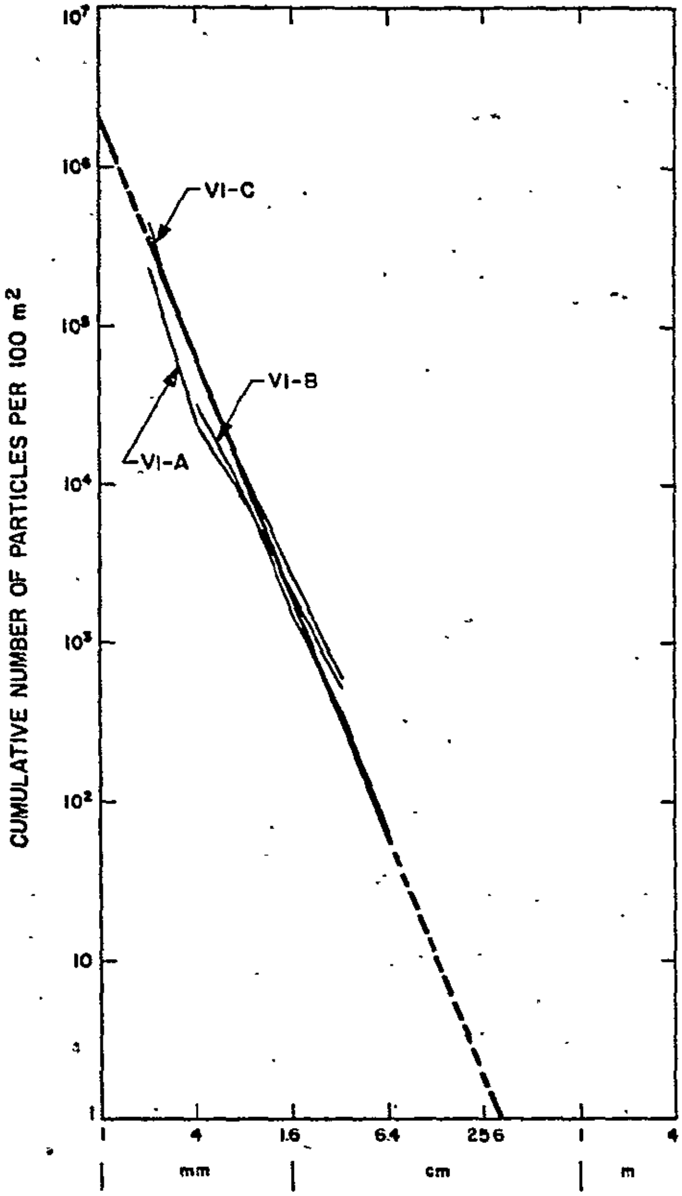

Figure 3.11. **Cumulative size-frequency distribution of fragments determined for three sample areas from *Surveyor VI* pictures.**

(From JPL Technical Report 32-1262)

(4) No quantitative results are available regarding lunar thermal gradients for surface temperatures below 120°K, nor can these be obtained from earth-based telescopes due to the sensitivity limitation of detectors, optical resolution limit of telescopes and interference effects from the earth atmosphere. Such data could only be obtained by high-resolution scanning IR radiometry from lunar orbiting vehicles. Such instrumentation, if it is not now aboard lunar orbiting missions in the Apollo program, would be a desirable payload to provide design information for the yaw sensor as well as any lunar horizon sensors that are contemplated.

3.1.2 Lunar Thermal Gradients: Supplemental BAI Study

3.1.2.1 Introduction

In the Barnes' report on lunar gradients (Section 3.1.1 above), the conclusion is made that the rocks on the lunar surface will be warmer than their surrounding area even at the end of the lunar night. Since the success of the instrument is predicated on this temperature difference, BAI has made some preliminary calculations to determine from a cosmological point of view a thermodynamic mechanism by which such a variation in temperature could exist at the end of the lunar night. The calculations are strictly first cut and have been made entirely for the purpose of establishing the credibility of the required temperature difference under the specified circumstances. These calculations, reproduced below, show that if the moon is considered to be infinitely conductive, the variations in temperature between lunar day and lunar night cannot affect the surface for a depth any greater than about 2 meters. Therefore, under practical conditions of finite conductivity, this skin depth could not be much greater than 10 meters. Thus the entire phenomenon of heating and cooling takes place in a very thin layer, and a rock that can be expected to have an appreciable temperature difference from that of surrounding dust need only extend into the lunar surface a distance of between 1 to 10 meters. In fact, our calculations show that if a rock does indeed extend into the lunar surface by this amount, then the temperature difference between the rock and surrounding dust, etc., will of necessity be greater than the minimum required temperature difference for the yaw sensor even at the end of the lunar night.

These calculations are predicated upon a completely evenly illuminated lunar surface, which is a pessimistic approximation since it ignores the temperature variations resulting from the shadowing effect of large lunar promontories. This shadowing effect would of course produce an even more optimistic picture than that resulting from calculations based simply on a lunar surface that enters the lunar night after having received equal solar radiation over its entire surface during the lunar day.

3.1.2.2 Analysis

The moon's infrared radiance differences are generated by its basic radiative mechanism, which is that of a relatively warm sphere of rock and dust radiating into the cryogenic coldness of the stellar sphere. The rate at which a patch of lunar surface radiates is proportional to two factors: the infrared emissivity of the surface and the thermal conductivity of the substratum. Infrared data on various dusts, sands, and rocks taken here on earth shows that their thermal emissivity is rarely under 0.5: hence, it is unlikely that the lunar surface emissivity will vary by more than a factor of 2. On the other hand, the thermal conductivity of terrestrial dusts and sands is typically a factor of 10 lower than that of rocks. Thus it is likely that the infrared radiance gradients on the surface of the moon are principally determined by local thermal conductivities (bare rock should appear warm, and deep dust should appear cool) and that radiance variations of the order of 10% exist over rocky areas.

Earth-based radiometric measurements* have shown that the lunar surface cools about 300°K during the lunar night as the moon's surface loses heat by radiation into space. We can develop a cosmological argument based on this fact that indicates that relatively large local gradients in infrared radiance can be caused entirely by variations in thermal conductivity in the topmost few feet of the lunar crust.

We will first show the untenability of the concept that a large percentage of the moon's mass acts as a thermal reservoir for providing energy to be radiated from the surface. From the calculation establishing this, we will then approximate the probable percentage of the moon's mass that is active in providing thermal energy to be radiated during the lunar night. From this approximation we can determine the order of magnitude of the skin depth affected by the difference in radiation received throughout the lunar day-night cycle.

For the purposes of this discussion we will model** the moon as a sphere with radius = 2×10^8cm, mass = 7×10^{25}gm, heat capacity*** = 1 watt sec/gm°K,

---

*J.J. Raimond, Hemel en Dampk. 48, 81 (1950).
J. H. Piddington & H. C. Minnett, Aust. J. Sci. Res. 2, 63 (1949).
E. Pettit (and S. B. Nicholson), Ap. J. 71, 102 (1930); 91, 408 (1940).

**"Astrophysical Quantities" by C. W. Allen; Athlone Press, University of London, 1955; see pages 162-163.

***Handbook of Chemistry and Physics - 29th Edition, 1945; Chemical Rubber Publishing Company, Cleveland, Ohio. See pages 1818-1820 titled "Heat Conductivity - Various Solids," and pages 1740-1741 titled "Specific Heat of Alloys and Various Solids."

surface emissivity* = 1, moon temperature = 400°K, and infinite thermal conductivity.

Based on this model, the moon radiates heat at a rate of:

$$4\pi(2 \times 10^8)^2 cm^2 \times 5.7 \times 10^{-12} \frac{watts}{cm^2 deg^4} \times T^4 deg^4 = 3 \times 10^6 T^4 watts$$

and its temperature T drops as a rate of:

$$\left[7 \times 10^{25} gm \times 1 \text{ watt sec/gm}^oK\right]^{-1} = 1 \times 10^{-26} \frac{^oK/sec}{watt}$$

$$\therefore \frac{dT}{dt} = 3 \times 10^{-20} T^4 \ ^oK/sec$$

$$\therefore \int \frac{dT}{T^4} = \int 3 \times 10^{-20} dt$$

$$\text{or } \frac{1}{T^3} - \frac{1}{400^3} = 9 \times 10^{-20} t$$

$$\text{but } \frac{1}{T^3} - \frac{1}{400^3} \doteq \frac{3\Delta T}{T^4} \text{ for small } \Delta T$$

$$\text{and } 10 \text{ days} = 10^6 \text{ seconds}$$

$$\therefore \Delta T = \frac{400^4}{3} \times 9 \times 10^{-20} \times 10^6 = 8 \times 10^{-4} \ ^oK$$

Thus we see that the moon's surface would cool no more than 10^{-3}°K during the lunar night if the thermal impedance of its bulk were negligible compared to the thermal impedance of its surface. However, it is well known that the moon's surface temperature drops from about 400°K at lunar noon to about 100°K during the lunar night.** Therefore, we are led to the conclusion that only a small part of the mass of the moon enters into the day-night temperature cycle and that this fraction of the moon's mass represents only the superficial stratum.

---

*"Handbook of Military Infrared" edited by W. L. Wolfe; Office of Naval Research, 1965; see Section 5.8 titled "Spectral Radiance of Terrain" (pages 142-173).

**"Astrophysical Quantities" by C. W. Allen; Athlone Press, University of London, 1955; see pages 162-163.

We can approximate the effective skin depth of the lunar thermal skin (i.e., the lunar analog of the permafrost depth) by noting that a skin depth d on a sphere of radius r contains a fraction of the sphere volume given by:

$$\frac{4\pi r^2 d}{\frac{4}{3}\pi r^3} = \frac{3d}{r}$$

Hence the lunar thermal skin depth is given by:

$$\frac{3d}{r} = \frac{8 \times 10^{-4}\ {}^{\circ}K}{400^{\circ}K - 100^{\circ}K} = \frac{3d}{2 \times 10^{8} cm}$$

$$d = 200 \text{ cm}$$

This indicates that roughly the top two meters of the moon are substantially involved in its monthly temperature cycle.

Several pertinent studies have been found in the literature that substantiate the BAI analysis of the probable lunar temperature variations and gradients. It is worth noting that from this information, it is possible to estimate the threshold sensitivity (in terms of detectable temperature differential within the area examined as defined by the instrument's angular intercepts) for any instrument designed to measure IR radiation from the lunar surface.

A paper from "Technology Review", 69, 23-30, 7/67 substantiates the preceding BAI lunar thermal analysis. The following points made in this paper concerning the nature of the lunar surface are particularly pertinent:

...Theory indicates that bare rock surfaces and boulders can contribute to anomalous thermal behavior...
...the surface must be a very good insulator, better, in fact, than most terrestrial insulators...
...the temperature at a meter or so below the surface remains constant, at about 240°K...
...the surface consists of loosely packed material, with low overall density...
...the density of the surface does not exceed one gram per cubic centimeter-less than half that of terrestrial soil or rock...
...indicating an increasing degree of compactness with depth...
...the lunar density under some meters of surface material probably compares with that of compacted terrestrial soil or rock...
...there are many rocks, particularly near certain craters...they appear to be scattered haphazardly over the surface...

...the young primary impact craters, which have not yet been strongly "weathered" by the erosive action of falling particles, probably contain more bare rock, in walls, floors, or rock debris, than older craters...

A paper appearing in the Astrophysical Journal, 139, 734-750, 2/15/64, provides information relating to the material composition of the moon's surface. This is particularly pertinent when considering the chosen angular coverage of the proposed yaw sensor detector elements and their intercepts on the lunar surface. To show this pertinence, the worst case analysis of the proposed yaw sensor detector array has been reworked in light of the information given in these papers, as follows.

The yaw sensor design using a pyroelectric detector has a calculated Noise Equivalent Temperature Difference of 0.11°K subtending 0.25° x 5° angles in a 100°K field of view. This sensitivity level will be used in a worst case analysis of the estimated infrared signal based on current estimates concerning the nature of the lunar surface.

The worst-case operating conditions for the infrared yaw sensor occur over those portions of the lunar surface that are at the end of the lunar night. The lunar surface temperature in those areas has dropped to approximately 100°K. The infrared radiance gradients in these areas are generated principally by thermal conductivity variations in the top meter of thickness of the moon's surface. The moon's temperature at depths below this top meter is constant at about 240°K and does not vary from day to night.

The thermal conductivity of lunar dust is probably an order of magnitude lower than the thermal conductivity of lunar rock. A substantial fraction of the moon's surface is probably covered by a dust layer over 10 cm thick. Therefore, areas of the lunar surface consisting of substantially bare rock a meter or more in depth will probably have a surface temperature roughly 10°K hotter than the 100°K surroundings at the end of the lunar night.*

The yaw sensor's 0.25° x 5° field of view will intercept a 0.44 km x 8.7 km rectangle on the surface of the moon at an assumed orbit altitude of 100 kilometers, and will exhibit a NEΔT of 0.11°K in sensing this surface area. The successful operation of the yaw sensor under worst case conditions will depend on variations in the amount of bare rock present of the order of $\frac{0.11°K}{10°K}$ or 1% of a 0.44 km x 8.7 km patch of lunar surface.

This variation is equivalent to a rocky area of 8.7 km x 0.44 km x 0.01 = 0.038 km^2, equivalent to a square that is 0.2 km on a side.

It has been shown that erosion processes on the lunar surface that transform conductive bare rock surfaces to insulated dust-covered surfaces "appear to

---

*The addition of a 10-cm layer of superficial dust on top of a one-meter-deep rock roughly doubles the thermal impedance of the stratum, halves the heat flow, and hence (by the Stefan-Boltzman Fourth Power Law of blackbody radiation) reduces the absolute surface temperature by 50%/4 = 12-1/2% of 100°K.

be bracketed in the 0.01 km - 1 km range."* This size range is consistent with that required for operation of the yaw sensor under worst case conditions.

3.1.2.3 Conclusion

It can easily be shown that for the temperatures of interest here, a ten percent variation in average thermal conductivity will produce a ten percent change in infrared radiance gradients** corresponding to a 2-1/2°K blackbody temperature change at 100°K. If we postulate that the moon is made of material similar to that which comprises the surface of the earth, then the mechanism for establishing this 10% variation in thermal conductivity is readily available. The thermal conductivity of terrestrial dusts and sands is typically a factor 10 lower than that of terrestrial rocks. Therefore, the requirement for establishing the postulated ten percent variation in average thermoconductivity is met if the 1 to 10 meter layer of interest on the lunar surface has a larger proportion of rock in one area than in another. This degree of inhomogeneity of the lunar surface must be sufficiently widely distributed to provide a temperature gradient over the area being examined by the yaw sensor, typically, about 5 miles by 5 miles (50-mile altitude). It would certainly seem that such a requirement is quite undemanding.

3.1.3 Thermal Gradients on the Earth

The major problem in earth orbit will occur at low orbital altitudes when sensing the ocean far from a land mass and under cloudless conditions. Very little measurement data on real-time thermal gradients in ocean centers exist, since this information can be readily obtained only from satellites. Quite extensive data exists based on airborne radiometric measurements of sea water temperature near the shores of the United States. Figures 3.12 and 3.13 represent satellite data on water temperatures at the center of the Altantic Ocean and airborne measurement data taken over a relatively short period of time on Lake Ontario. Figure 3.14 represents sea-water-temperature measurements taken off the east coast of the United States. The proposed $5^{\circ} \times 5^{\circ}$ field of view composed of 20 elemental $0.25^{\circ} \times 5^{\circ}$ fields of view, when superimposed on these thermal contour maps, span a thermal gradient of about 0.1°C. This thermal gradient results in a ΔT between the adjacent elements of only 0.005°C, which is, however, greater than the achievable $NE\Delta T$ of the yaw sensor (using a pyroelectric detector array) for 274°K - 284°K blackbody target temperatures. (See Figure 3.3.) It can therefore be concluded that for unclouded conditions over the ocean, the yaw sensor can operate successfully.

*"Surface Temperature Variations During the Lunar Nighttime" by B. C. Murray and R. L. Wildey; Astrophysical Journal, Vol. 139, pp 734-750, 2/15/64.
**Spectral Variation of Blackbody Radiation by M. G. Dreyfus; Applied Optics, 2, 1113-1115, 11/63.

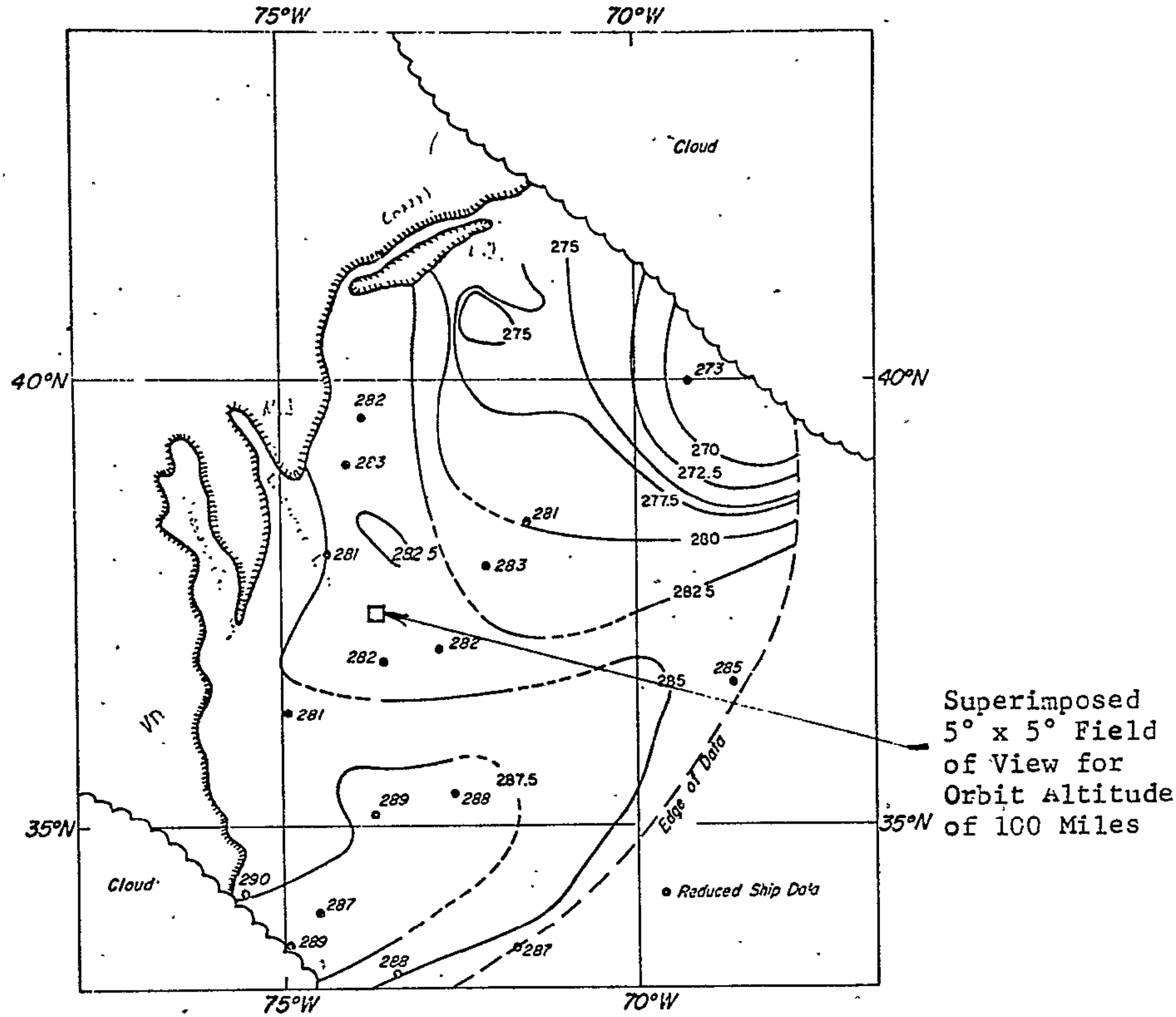

Figure 3.12. Real Time Data, Sea Surface Temperature, Pass 106-D (26 June 1963), TIROS VII

(Weiss - "Access to Water Resources using Infrared Remote Sensing of Water Surface Temperature," M. Weiss, presented at the Canadian Aeronautics and Space Institute Avionics Symposium on Avionics and Natural Resources, Chateau Laurier, Ottawa, January 15 - 16, 1968.)

Superimposed 5° x 5°
Field of View for Orbit
Altitude of 100 Miles

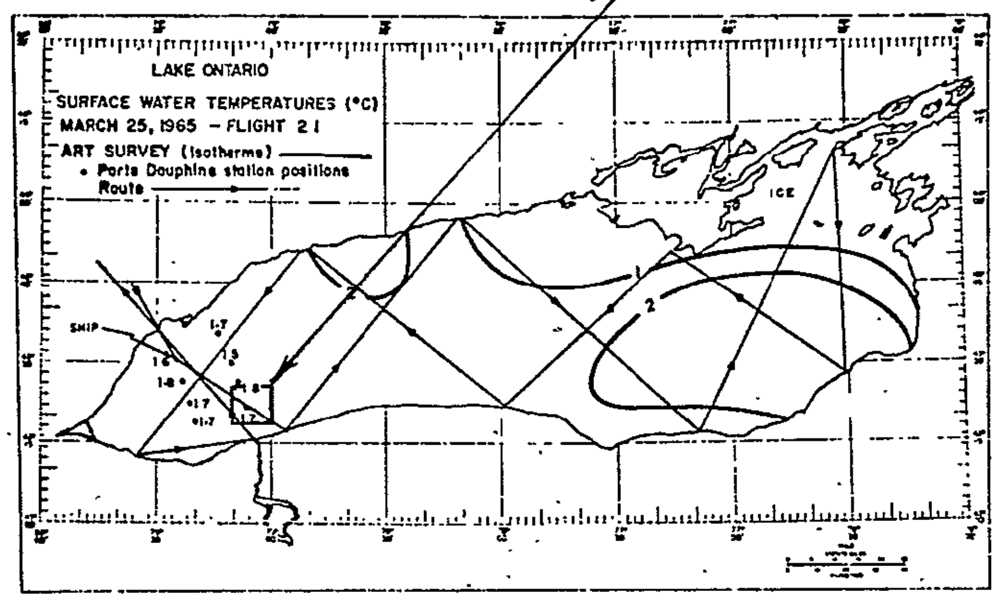

Figure 3.13. ART Survey, Lake Ontario, March 25, 1965

(Weiss - op. cit.)

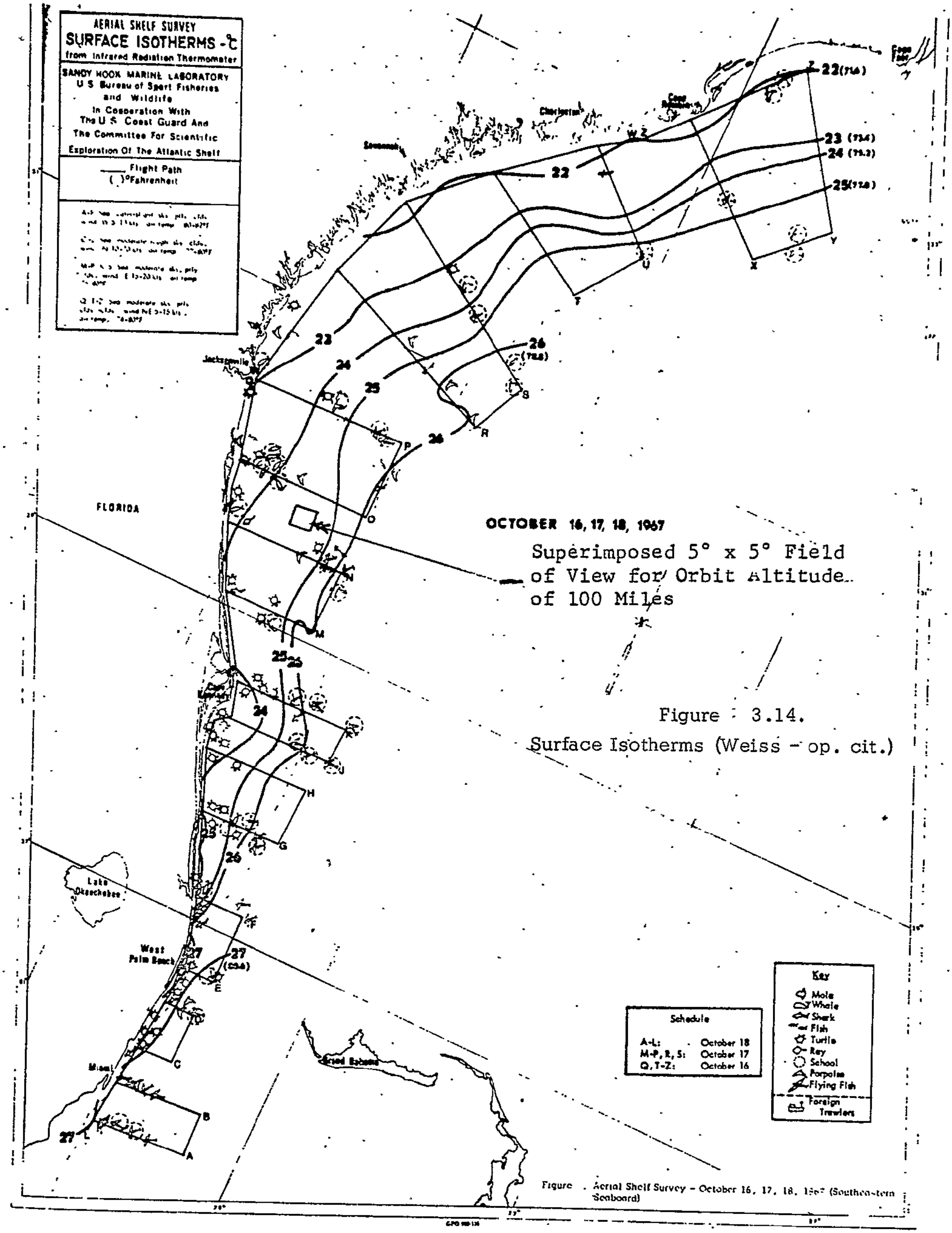

Superimposed 5° x 5° Field of View for Orbit Altitude of 100 Miles

Figure 3.14.
Surface Isotherms (Weiss - op. cit.)

For ocean thermal gradients of less than 0.1°C, the question that must be evaluated is the probability of obtaining clear skies over an extended surface on the ocean. The best data relative to this question has been obtained from TIROS satellites.* Some results from these satellites are presented in Figures 3.15, 3.16, 3.17, 3.18, and 3.19 for earth latitudes from 30° north to 25° south averaged over a monthly basis. These data indicate that there is no area on the earth in this latitude region where an essentially cloudless condition exists. Since most clouds are above 2,000 feet, this guarantees sharp thermal gradients of at least 5°C above the sea-water temperature, which will be entirely sufficient for yaw sensor operation. There will, of course, be isolated instances where the yaw sensor will view cloudless conditions. However, this is expected to persist for less than 1/10 of an orbit. (Even this expectation might be thought unduly pessimistic. See Section 3.1.4, below.)

3.1.4 Thermal Gradients on Earth: Supplemental BAI Study

Barnes points out that the thermal gradients in the ocean's surface may be too small to be sensed by the proposed yaw sensor and predicates success upon the presence of clouds within the field of view. (See Section 3.1.3, above.) Again, in an attempt to establish confidence in the probability of success of the yaw sensor under these adverse conditions, BAI has made some additional investigations in this area.

It should be noted that the requirement for establishing a trackable image is merely a requirement that a measurable temperature difference exist between the image on <u>any</u> two staves across the entire surface of the IR detector; thus the system requirements become much simpler than might appear at first. In other words, what is necessary when the yaw sensor is operating at about a 400-mile altitude is that within a rectangle of about 40 miles by 40 miles there be one area of approximately 2 miles by 40 miles that has cloud cover different from that of another rectangle 2 miles by 40 miles.

Recent unpublished analyses have been made of the spatial distribution of infrared cloud radiance by the University of Wisconsin and by the National Environmental Satellite Center of ESSA**. These analyses have consisted of histograms of apparent infrared temperature versus frequency of occurrence in the radiometric data telemetered from two infrared radiometers, the MRIR (Medium Resolution Infrared Radiometer) and the HRIR (High Resolution Infrared Radiometer), put into orbit by NASA-Goddard.

---

*Obtained from the U. S. Weather Bureau.

**Private communication 8/7/68 from Dr. William L. Smith, National Environmental Satellite Center, ESSA, Suitland, Md.

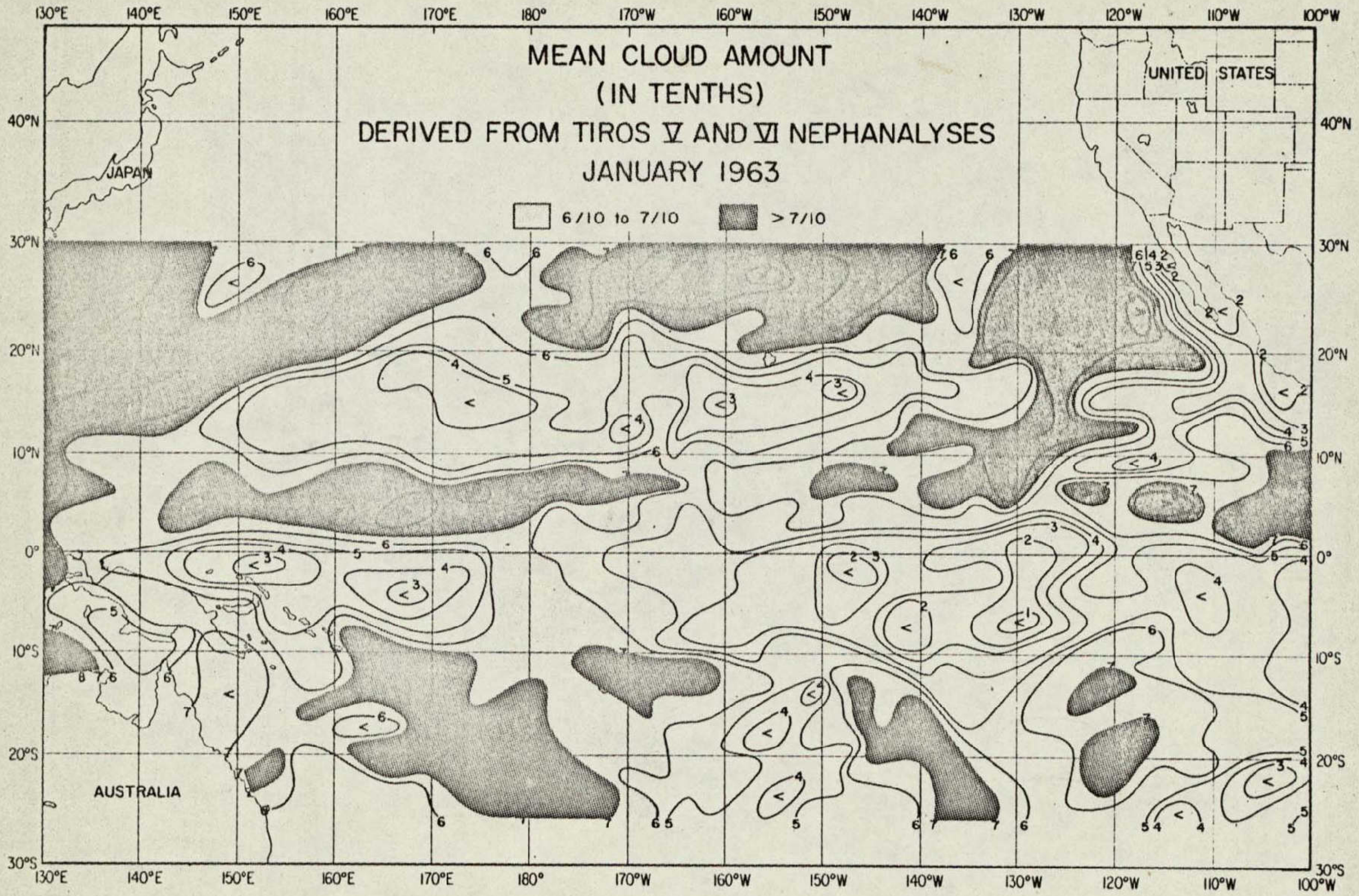
MEAN CLOUD AMOUNT
(IN TENTHS)
DERIVED FROM TIROS V AND VI NEPHANALYSES
JANUARY 1963
6/10 to 7/10
>7/10
JAPAN
UNITED STATES
AUSTRALIA
130°E
140°E
150°E
160°E
170°E
180°
170°W
160°W
150°W
140°W
130°W
120°W
110°W
100°W
40°N
30°N
20°N
10°N
0°
10°S
20°S
30°S

Figure 3.15.

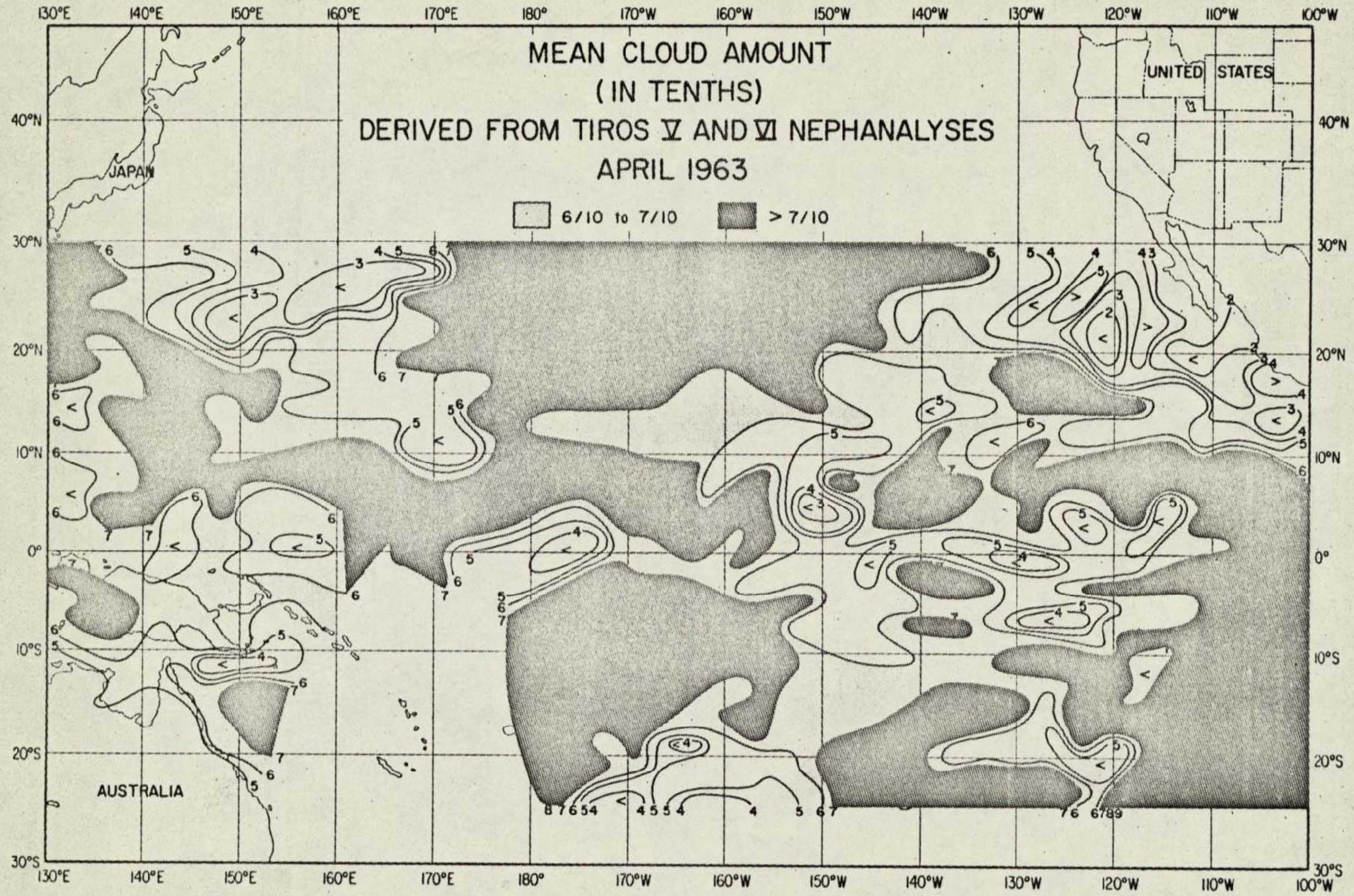
MEAN CLOUD AMOUNT
(IN TENTHS)
DERIVED FROM TIROS V AND VI NEPHANALYSES
APRIL 1963
6/10 to 7/10
> 7/10
JAPAN
UNITED STATES
AUSTRALIA
130°E
140°E
150°E
160°E
170°E
180°
170°W
160°W
150°W
140°W
130°W
120°W
110°W
100°W
40°N
30°N
20°N
10°N
0°
10°S
20°S
30°S

Figure 3.16.

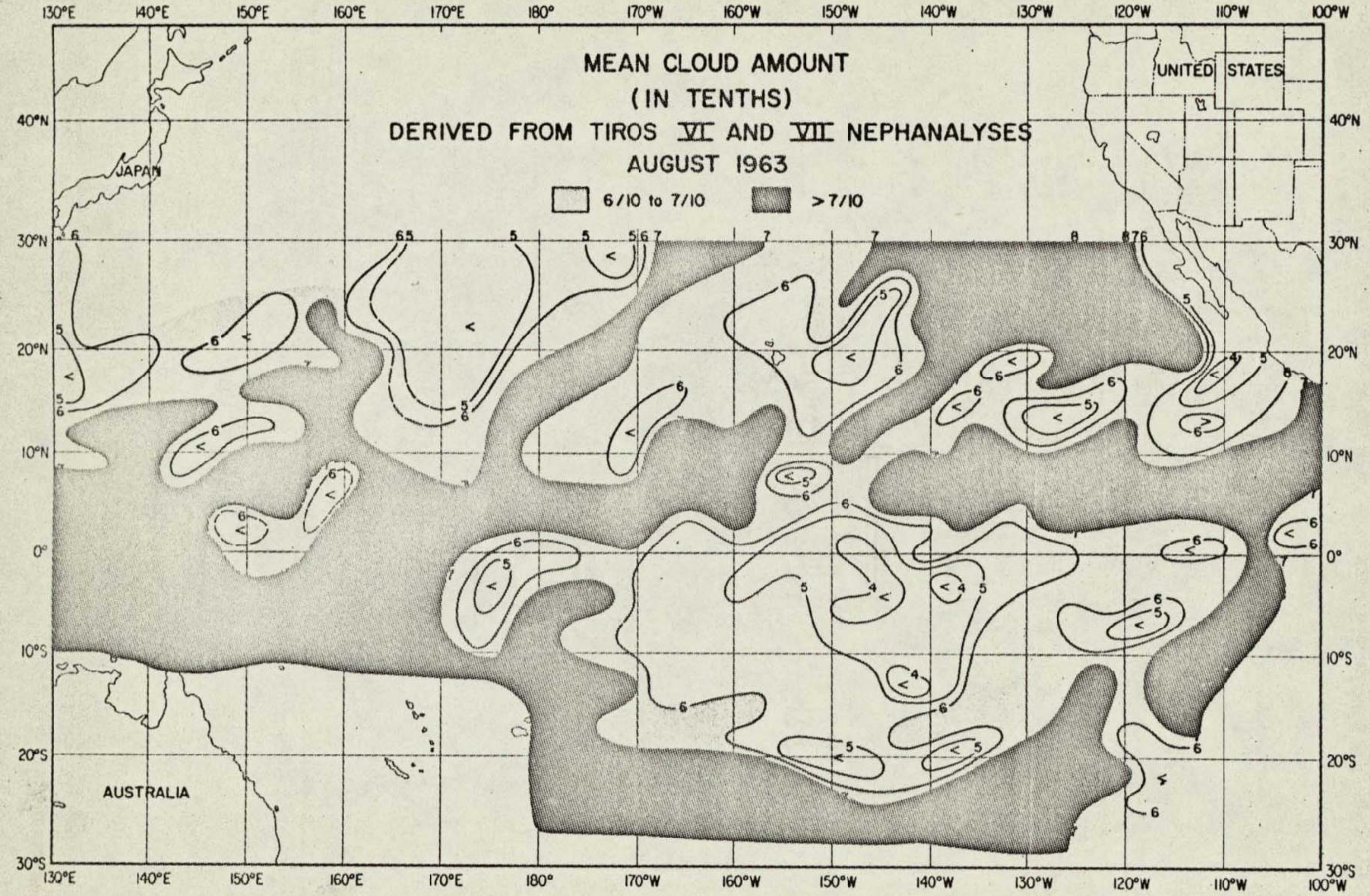
MEAN CLOUD AMOUNT
(IN TENTHS)
DERIVED FROM TIROS VI AND VII NEPHANALYSES
AUGUST 1963
6/10 to 7/10
>7/10
JAPAN
UNITED STATES
AUSTRALIA
130°E
140°E
150°E
160°E
170°E
180°
170°W
160°W
150°W
140°W
130°W
120°W
110°W
100°W
40°N
30°N
20°N
10°N
0°
10°S
20°S
30°S

Figure 3.17.

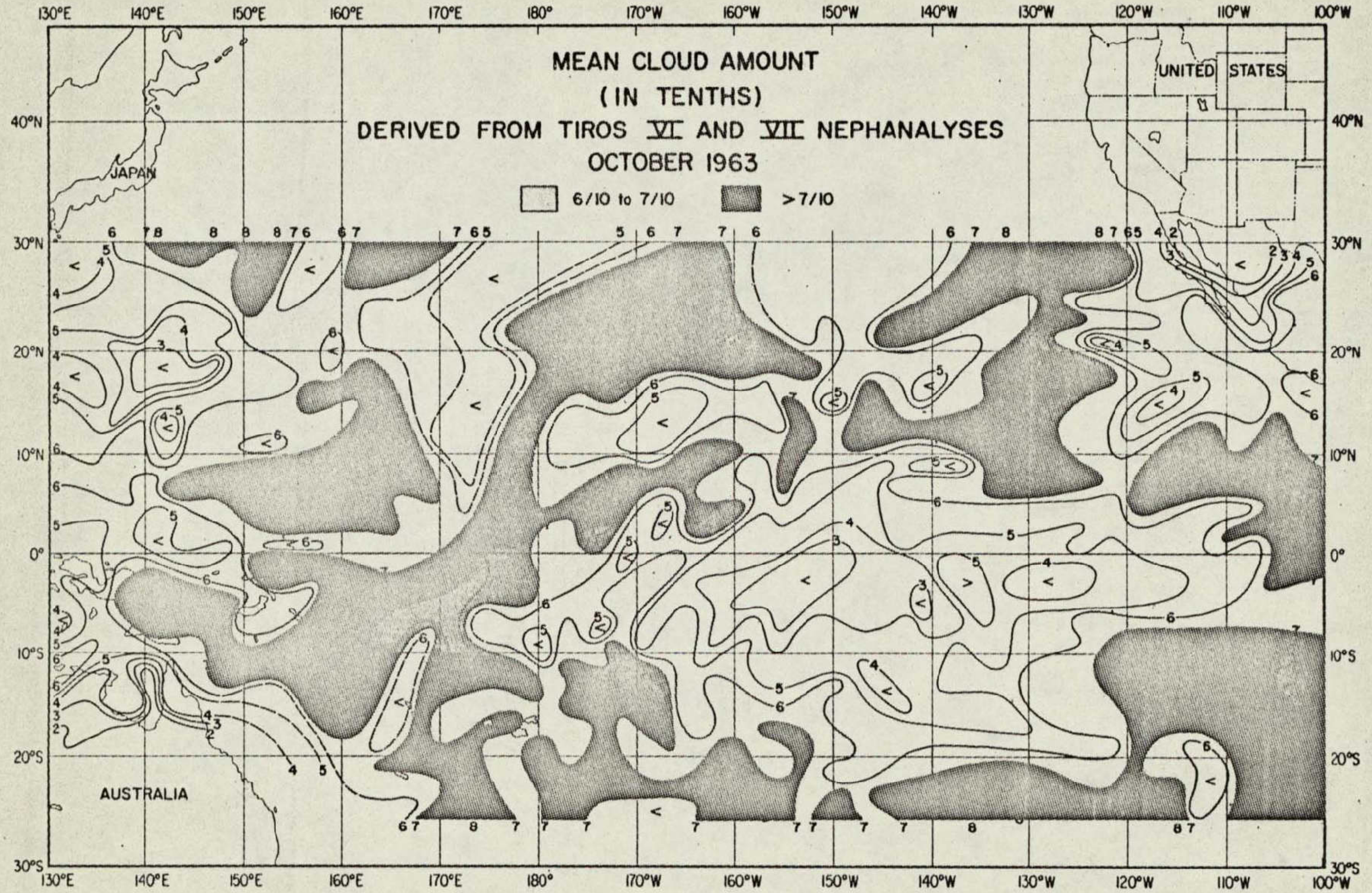
MEAN CLOUD AMOUNT
(IN TENTHS)
DERIVED FROM TIROS VI AND VII NEPHANALYSES
OCTOBER 1963
6/10 to 7/10
>7/10
JAPAN
UNITED STATES
AUSTRALIA
130°E
140°E
150°E
160°E
170°E
180°
170°W
160°W
150°W
140°W
130°W
120°W
110°W
100°W
40°N
30°N
20°N
10°N
0°
10°S
20°S
30°S

Figure 3 .18.

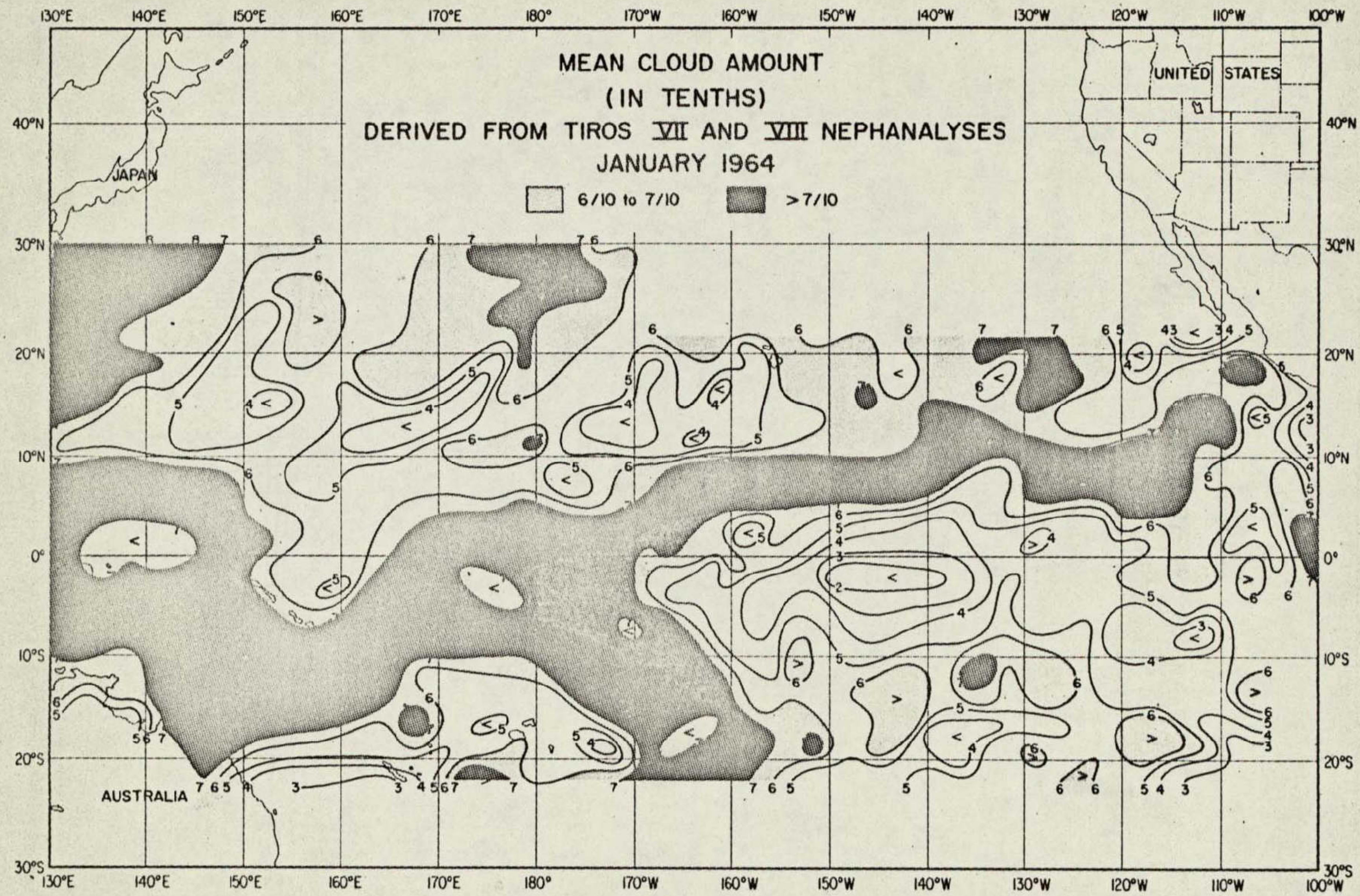
MEAN CLOUD AMOUNT
(IN TENTHS)
DERIVED FROM TIROS VII AND VIII NEPHANALYSES
JANUARY 1964
6/10 to 7/10
>7/10
JAPAN
UNITED STATES
AUSTRALIA
130°E
140°E
150°E
160°E
170°E
180°
170°W
160°W
150°W
140°W
130°W
120°W
110°W
100°W
40°N
30°N
20°N
10°N
0°
10°S
20°S
30°S

Figure 3.19.

The MRIR has a field of view 25 miles in diameter on the surface of the earth. Its histograms show a broad spectrum of apparent temperatures with high frequencies, indicating that the average cloud cell is less than 25 miles in diameter.

The HRIR has a field of view 5 miles in diameter. Its histograms show two discrete temperature levels appearing with high frequency, one corresponding to the surface of the earth, and the other to the cloud temperature. This indicates that the average cloud cell is of the order of 5 miles in diameter. From these histograms and the analyses made thereon, the probability of finding an area over the ocean sufficiently cloudless to create a yaw measurement problem is extremely low.

3.2 PRELIMINARY DESIGN OF IR FRONT END*

3.2.1 Effects on System Design Parameters of Thermistor Detector vs. Pyroelectric Detector

Although initially the use of a thermistor bolometer detector was intended for the yaw sensor, we felt that considerable simplification and cost reduction would be obtained if a pyroelectric sensor array were used. The use of a thermistor detector requires individual preamplifiers for each channel due to the high impedances of this detector. On the other hand, pyroelectric detector arrays have been fabricated incorporating an output transistor for each detector, thus providing each with a low output impedance. This has allowed the successful sampling of multi-element detector arrays at the detector level using a MOSFET sampler, a technique that has been completely developed on a current program at Barnes.

The simplifications achieved in the use of a pyroelectric detector were discussed in the Barnes Second and Third Monthly Progress Reports, and are briefly reviewed here. For economic production, the 20-element thermistor array should have been defined on a single 20 mm by 20 mm flake. A thermistor flake of these dimensions, however, would have had an unacceptable signal-to-noise performance level. The alternative was to combine four 10 mm x 10 mm thermistor flakes and to define an array of 10 active and 10 compensator flakes by depositing a grid of gold leads. The four 10 mm x 10 mm flakes would then have been mounted on a common heat sink, and adjacent elemental flakes connected together to form the required 20 mm by 20 mm array.

---

*Section 3.2 was prepared by Barnes Engineering Co., with the exception of a supplemental study of the pyroelectric detector array conducted by BAI and described in Section 3.2.3.2.

However, it was found that when this array was combined with the trough pyramid optics described in the proposal, the field of view relative sensitivity was reduced due to vignetting of the pyramid optic at either edge of the entrance aperture as shown in Figure 3.20. The fabrication requirements for the type of lens needed to eliminate this vignetting were considered impractical.

None of these drawbacks occur with the pyroelectric detector, since this detector can be fabricated on a single flake, thus eliminating about 120 connections. In addition, no passive elements are needed in the pyroelectric detector array, permitting butting elemental fields of view with simplified pyramid optics.

3.2.2 Yaw Sensor System with Thermistor Array

A preliminary design prepared for the optical head to be used with the thermistor detector array is shown in Figure 3.21. The yaw sensor head consists of a lens, the detector array, a preamplifier assembly, a preamplifier output sampling switch, and a power supply.

The optical design comprises an all-reflective Cassegrain objective system. A wedge reflective optic is combined with the 20-element thermistor array to obtain twenty 0.25° by 5° elemental butting fields of view. Figure 3.22 shows a detailed view of this detector array assembly. The purpose of the reflective wedge is to increase the detector effective dimension in one direction to provide increased optical gain, low optical cross-talk and high optical quality. In addition, space was allowed for the reference thermistor flakes associated with the active thermistor elements, thus inherently providing for the butting fields of view.

The main problem anticipated with the reflective wedge optic was the construction, because of the small dimensions and relatively smooth surface required.

3.2.2.1 Electronic Processing Using Thermistor Detector

The electronic processing circuit must amplify and sequentially sample the signal of each elemental detector. The design originally proposed is shown in Figure 3.23 [illegible]

Each preamplifier is a Fairchild "Microamp" 709 integrated circuit with a parametric amplifier input stage. Each preamplifier has an electrical bandwidth of 0.01 to 16 cps, achieved with the aid of coupling capacitors allowed by the high input impedance of the input field effect transistor. The ac coupling of the preamplifiers eliminates any dc drift terms in the detector

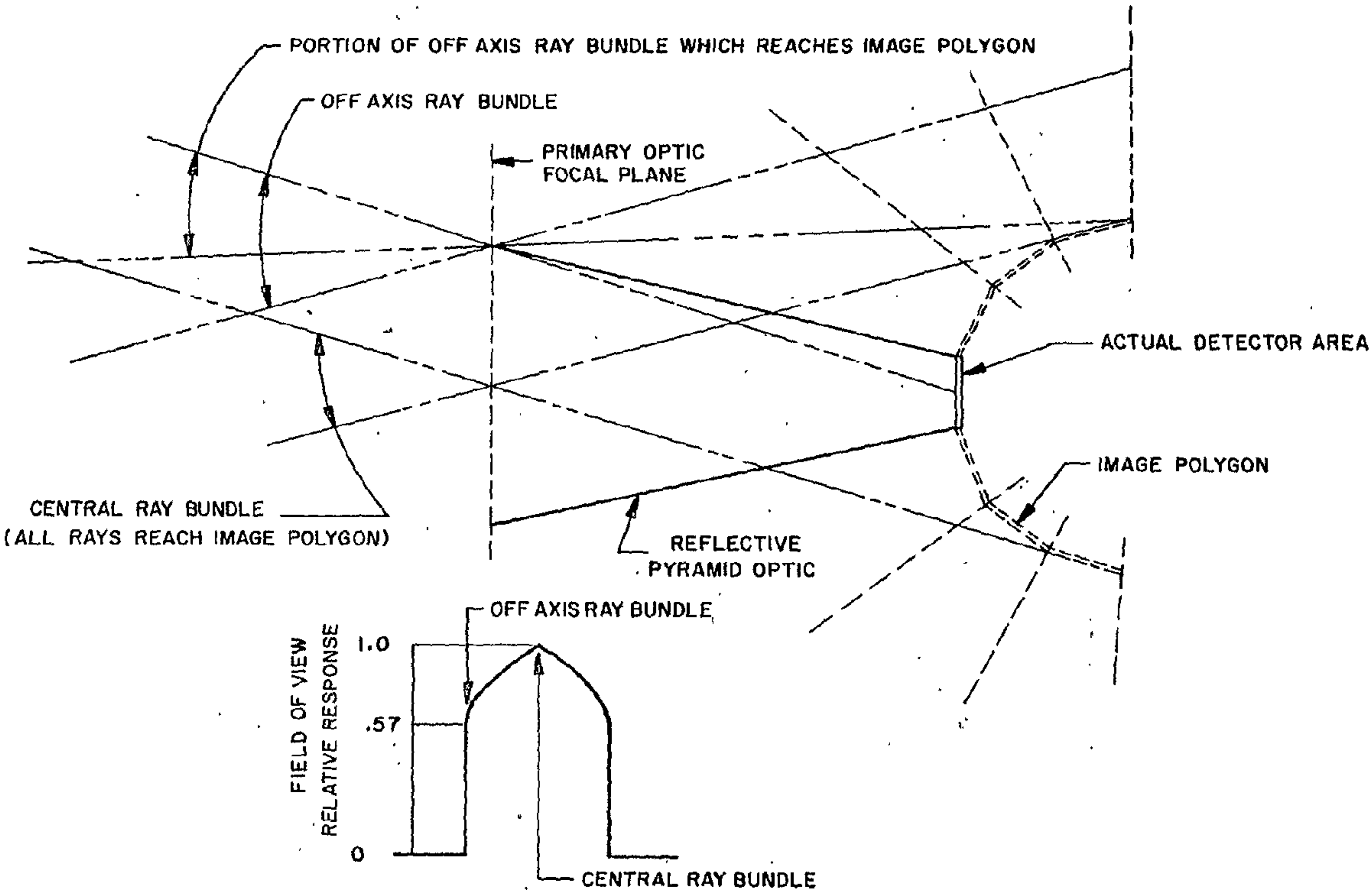

Figure 3.20. FIELD OF VIEW VIGNETTING BY PYRAMID OPTIC FOR THERMISTOR ARRAY

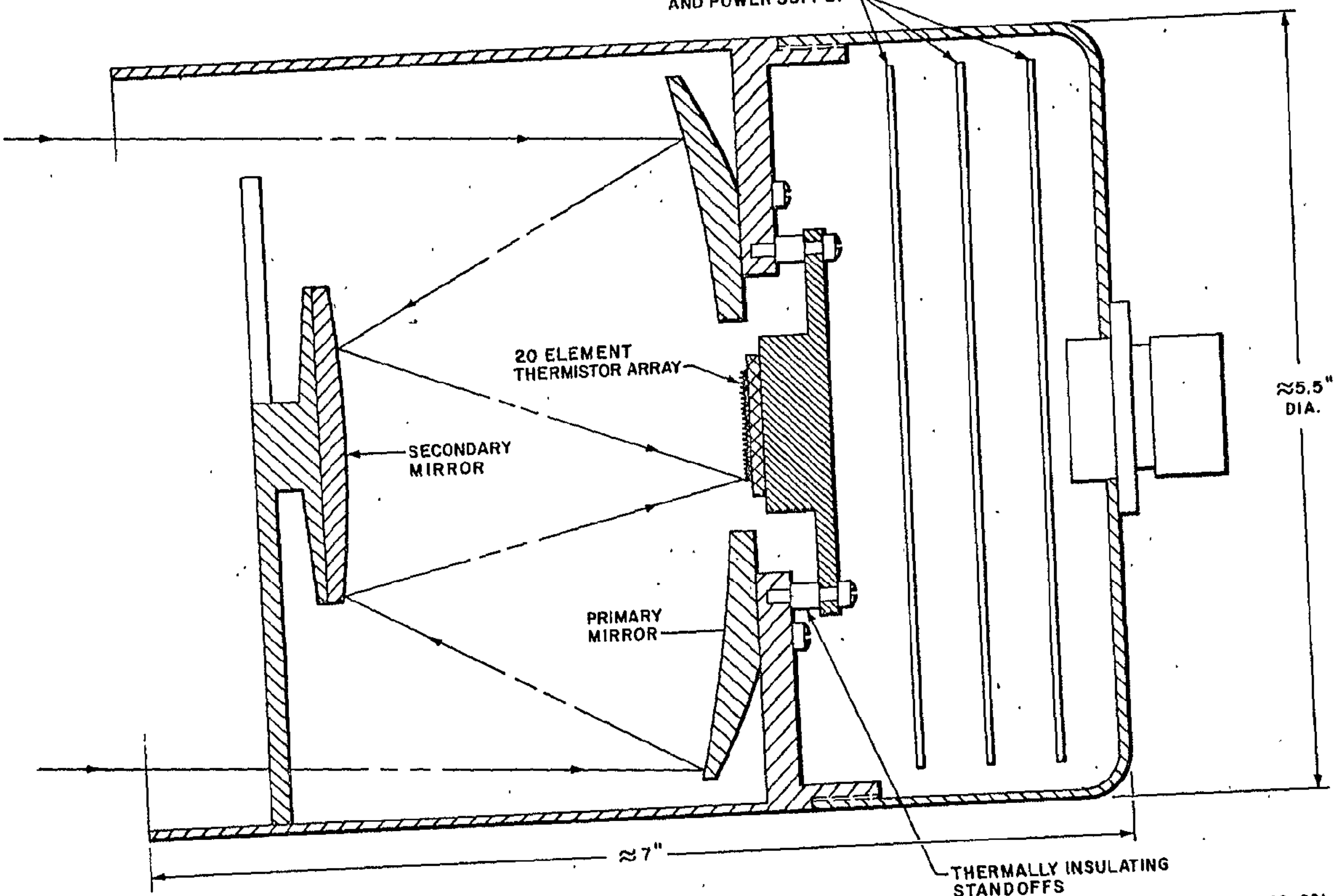

Figure 3.21. YAW SENSOR OPTICAL HEAD, PRELIMINARY CONFIGURATION, THERMISTOR ARRAY

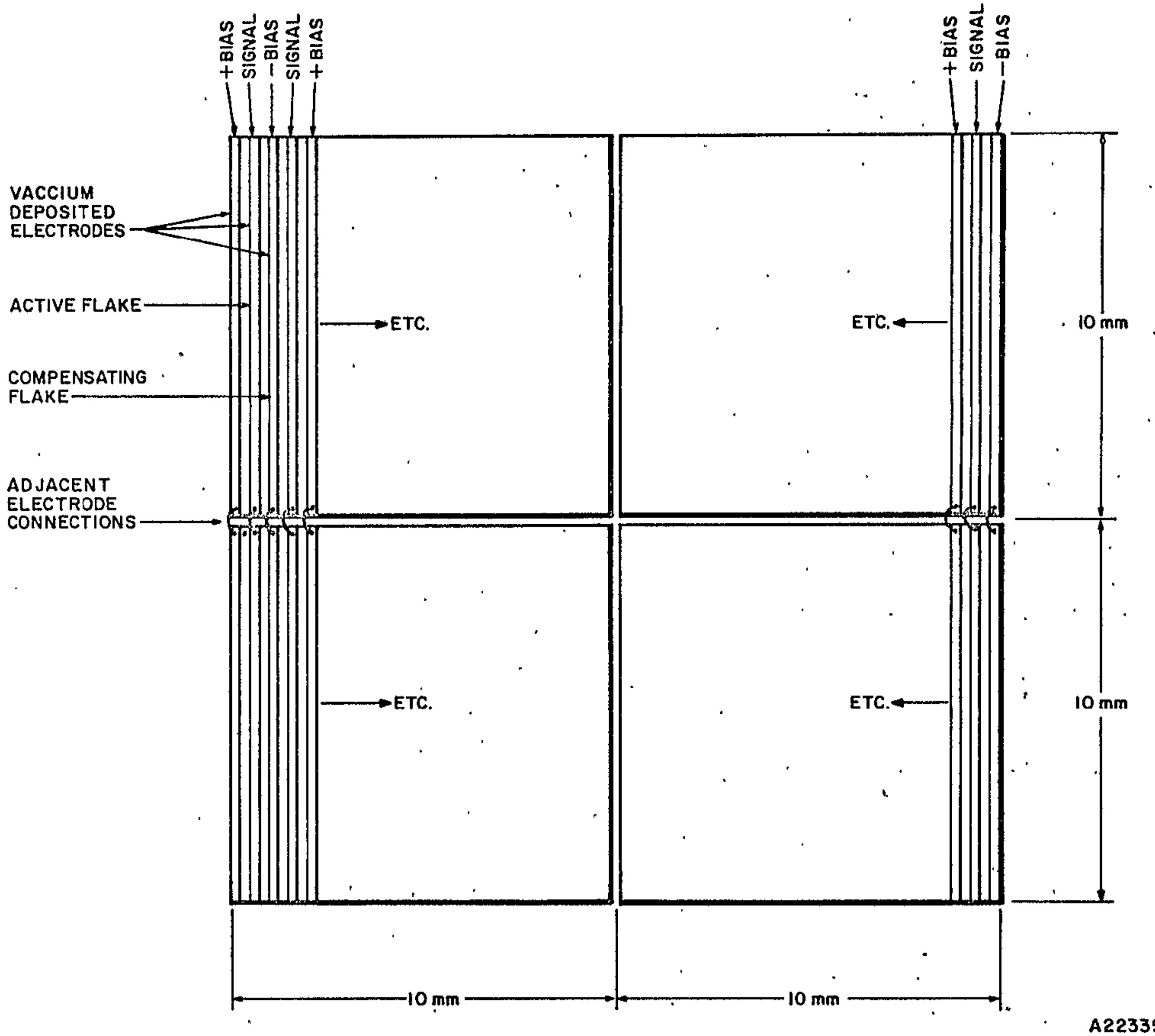

Figure 3.22. THERMISTOR ARRAY CONFIGURATION

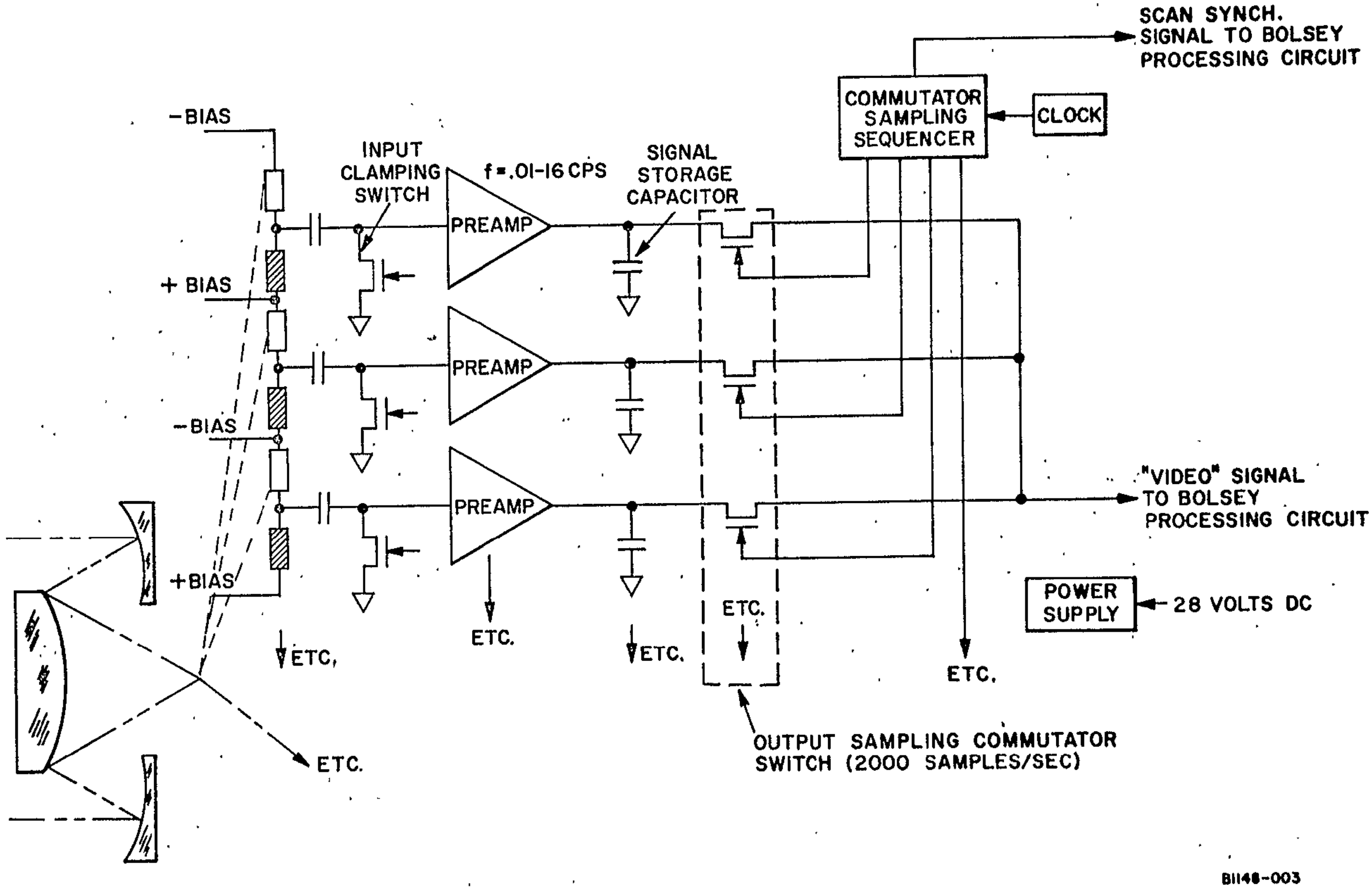

Figure 3.23. **YAW SENSOR OPTICAL HEAD BLOCK DIAGRAM**
WITH THERMISTOR DETECTOR ARRAY

array or preamplifiers. Each preamplifier signal is integrated in an output capacitor for the array sampling period of 0.01 second, and the voltage of each capacitor is then sequentially read out by a high level electronic sampling switch. This arrangement results in the highest overall signal-to-noise ratio. At the end of each electronic sampling sequence, all of the input and output capacitors are discharged, thus eliminating any dc voltage build-up and subsequent saturation of the BAI processing electronics.

3.2.3 Pyroelectric System - Optical Design

After the decision was reached to include the pyroelectric detector array into the yaw sensor study, an optical and an electronic system compatible with this array were designed.

Figure 3.24 is a layout drawing of the yaw sensor optical head. In this design, a flat folding mirror is used so that the yaw sensor occupies a minimum volume. The "stretched-out" or unfolded configuration of the optical head is shown in Figure 3.25.

The optical system consists of:

(1) An entrance aperture plate having dimensions of 0.6" x 7.6".

(2) A primary spherical mirror having dimensions of 2.5" x 9.5" and a focal length of 15". *

(3) A silicon field lens with spherical surfaces. This lens performs the dual function of a field lens and a field flattener. Silicon, because it is transparent to infrared radiation out to about 100 microns, is suitable for use on the cold side of the moon.

(4) A reflective pyramid optic assembly used to cause the 0.027" x 1.2" dimensions of the pyroelectric detector array to subtend the desired $5^{\circ} \times 5^{\circ}$ field.

A computer ray trace was made on the primary spherical mirror and the pyramid optic assembly. The optical aberrations over the $5^{\circ} \times 5^{\circ}$ field of the yaw sensor at the entrance plane to the pyramid optic are shown in Figure 3.27.

The reason for the aperture high aspect ratio can be seen in the ray traces shown in Figure 3.26. A discussion of the dimensions used in the optical system is given in the Barnes Fourth Monthly Progress Report.

In the plane defined by the 0.6" aperture dimension, the pyramid optic assembly produces an image polygon of the entire detector array. The field lens produces

*The field lens results in an effective focal length of approximately 13.8".

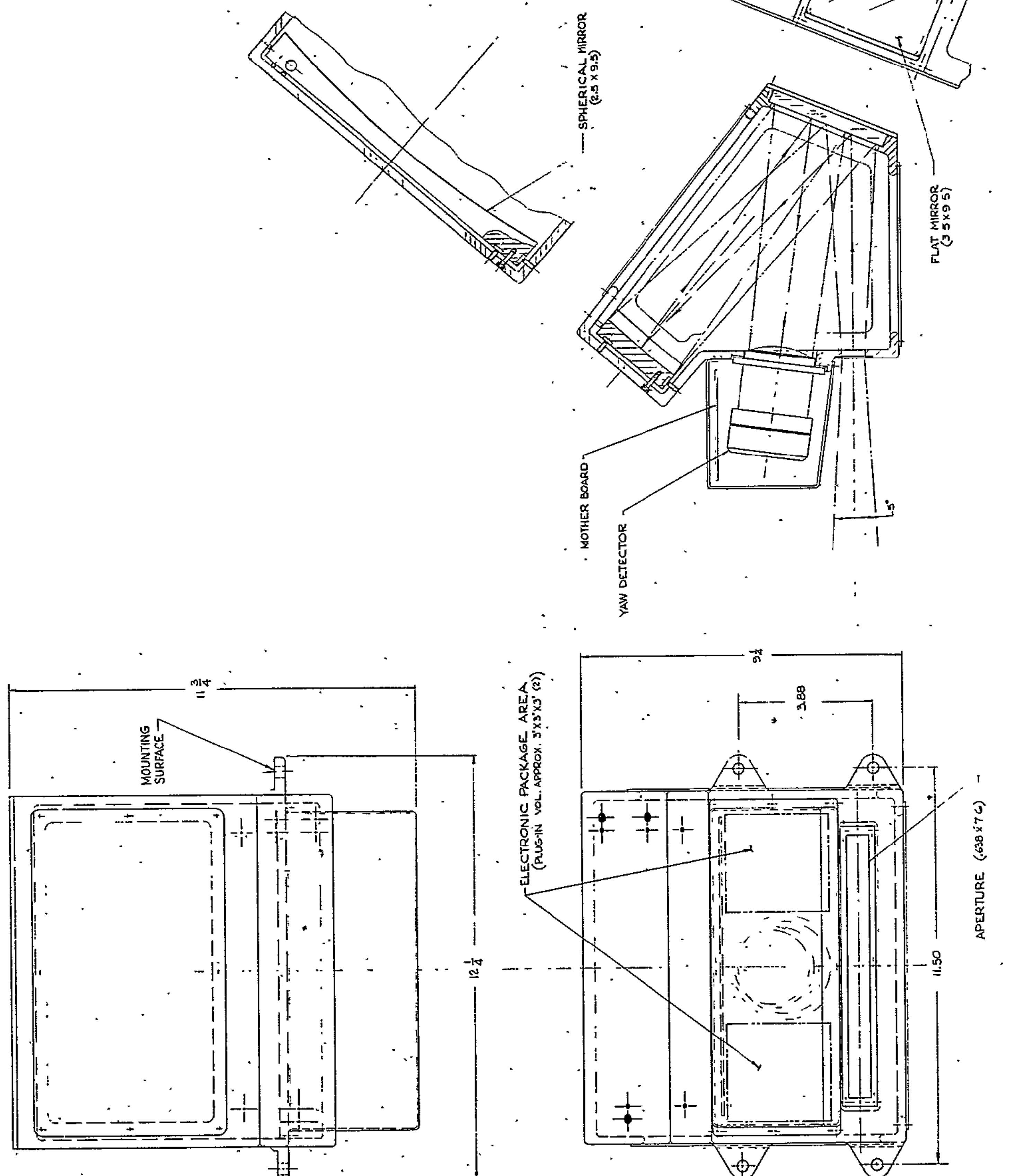

Figure 3.24. Yaw Sensor Optical Head, Preliminary Configuration, Pyroelectric Array

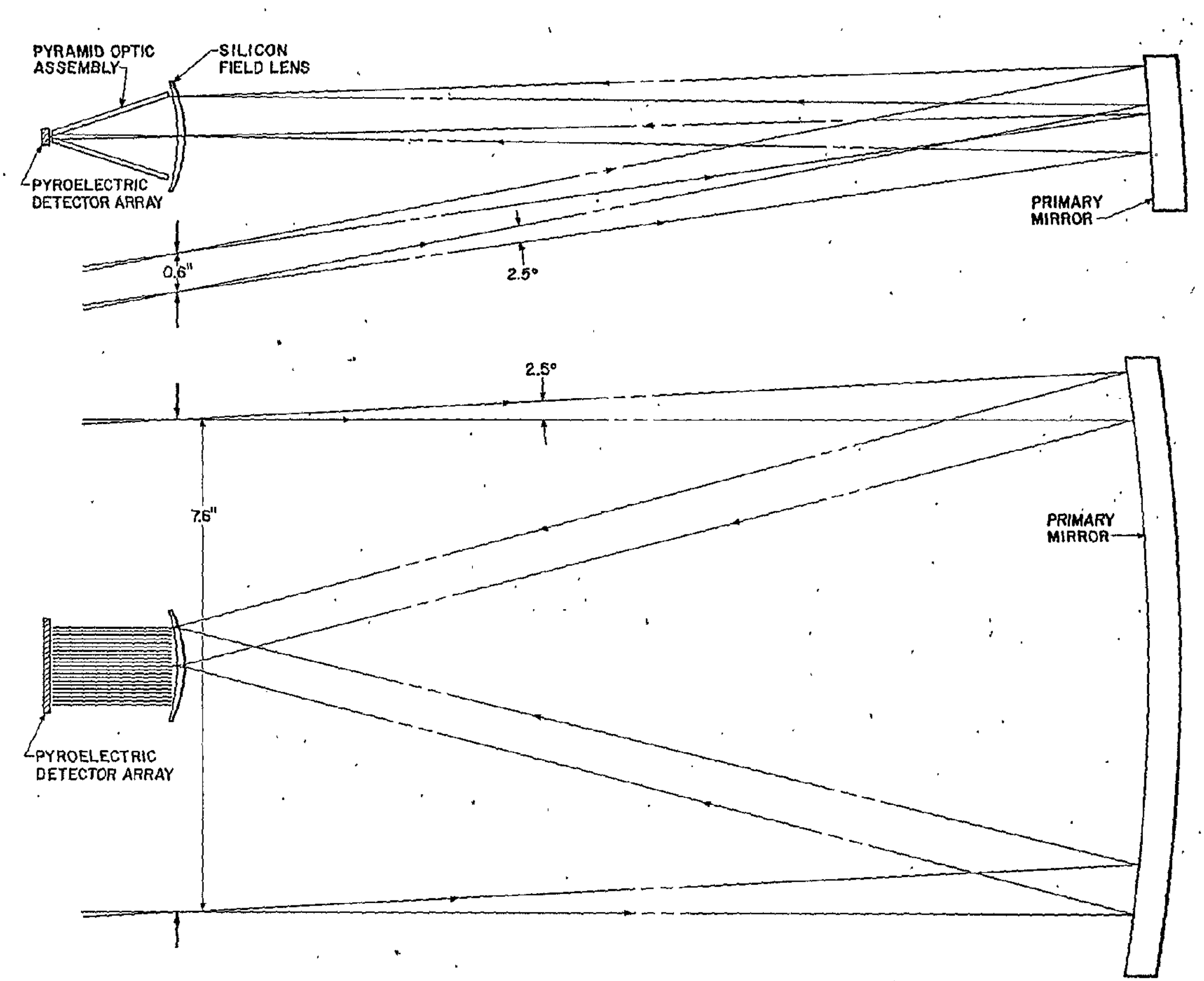

C22350

FIGURE 3.25. OPTICAL LAYOUT OF YAW SENSOR

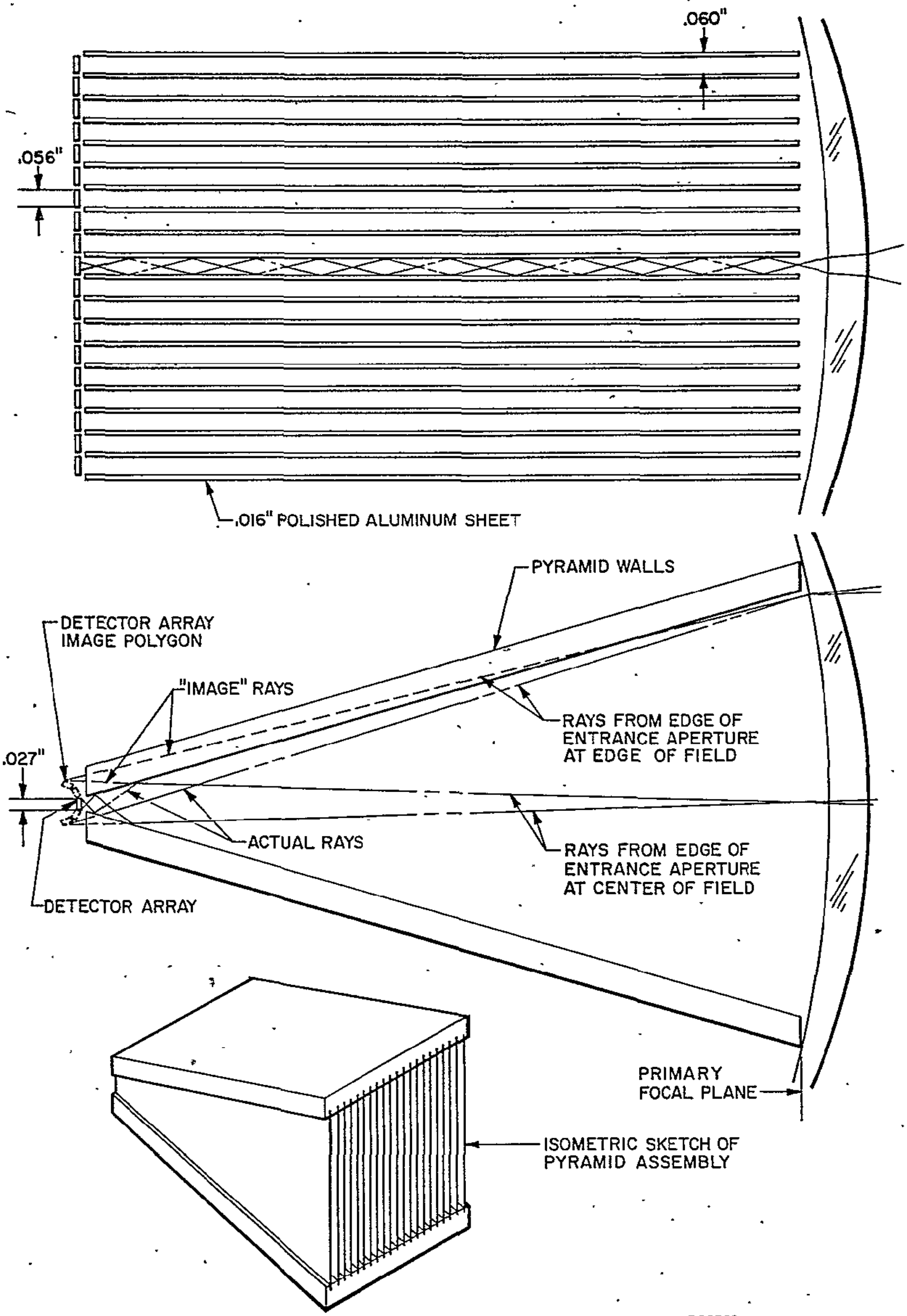

FIGURE 3.26. PYRAMID OPTIC DETAIL

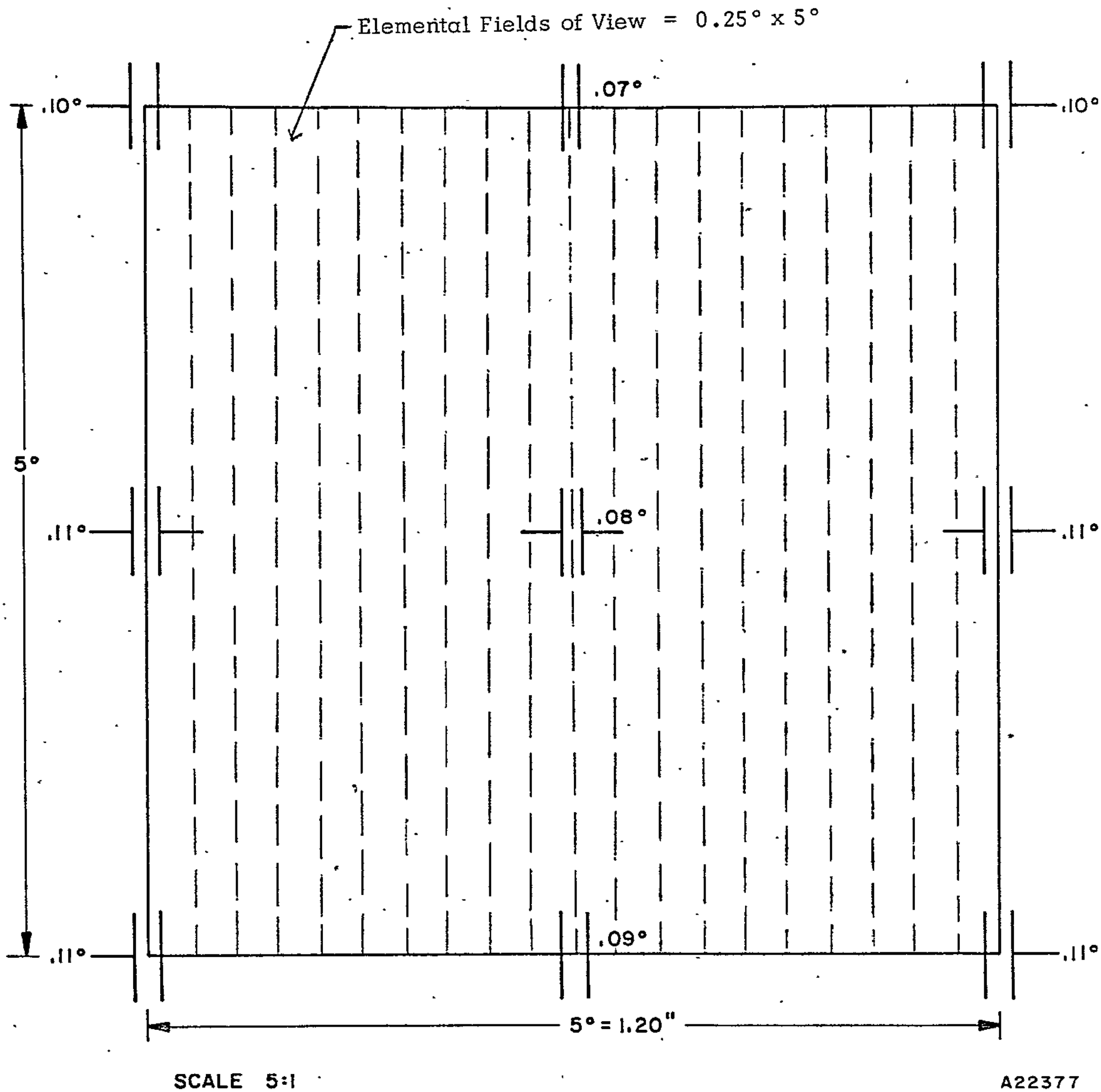

Figure 3.27 UNIDIRECTIONAL OPTICAL ABERRATIONS FOR IR YAW SENSOR

an image of the entrance aperture on this image polygon. This in effect causes all rays from the entrance aperture within $\pm 2.5^{\circ}$ of the optical axis to reach the detector array.

In the orthogonal plane, the field lens performs essentially no function, since the 0.016" thick flat vanes situated between adjacent pyroelectric detector elements serve to transfer any ray entering the pyramid assembly to the appropriate detector element.

The method of fabricating the vane assembly is indicated in the isometric drawing shown in Figure 3.26. It will be composed of two polished plates each having twenty milled slots, 0.016" wide on 0.060" centers. The vanes will be fabricated from 0.016" thick polished aluminum sheets having a triangular shape, and will be inserted and epoxied into these slots as indicated in the isometric drawing.

Detail drawings for this reflective vane assembly were generated, and the required parts were machined.

Figure 3.28 shows the assembled reflective pyramid optic. The assembly of this unit is relatively straightforward so that its fabrication is definitely feasible. The pyramid optic assembly also provided the expected image polygon so that it should provide the theoretically expected optical gain. The detail drawings for the components of this reflected pyramid are included in the Barnes' Sixth Monthly Progress Report. These drawings have taken into account the lead connections to the 20-element detector array.

Figure 3.29 shows the assembly drawing of the pyroelectric array, pyramid optic assembly, and field lens.

3.2.3.1 Pyroelectric Detector Array

The pyroelectric detector array that is proposed for use in the yaw sensor has been developed at Barnes under another contract. Therefore, it this array is used in the yaw sensor, the nonrecurring cost involved in fabricating a special pyroelectric array would be eliminated. This array is presently composed of ten 0.026" x 0.026" elements.

As can be seen in Figure 3.30, this array would be modified by connecting together pairs of adjacent elements, thereby resulting in a 5-element pyroelectric detector array on a single substrate with each element having dimensions of 0.026" x 0.056". Four of these substrates would then be mounted together end to end to form the required 20-element pyroelectric array.

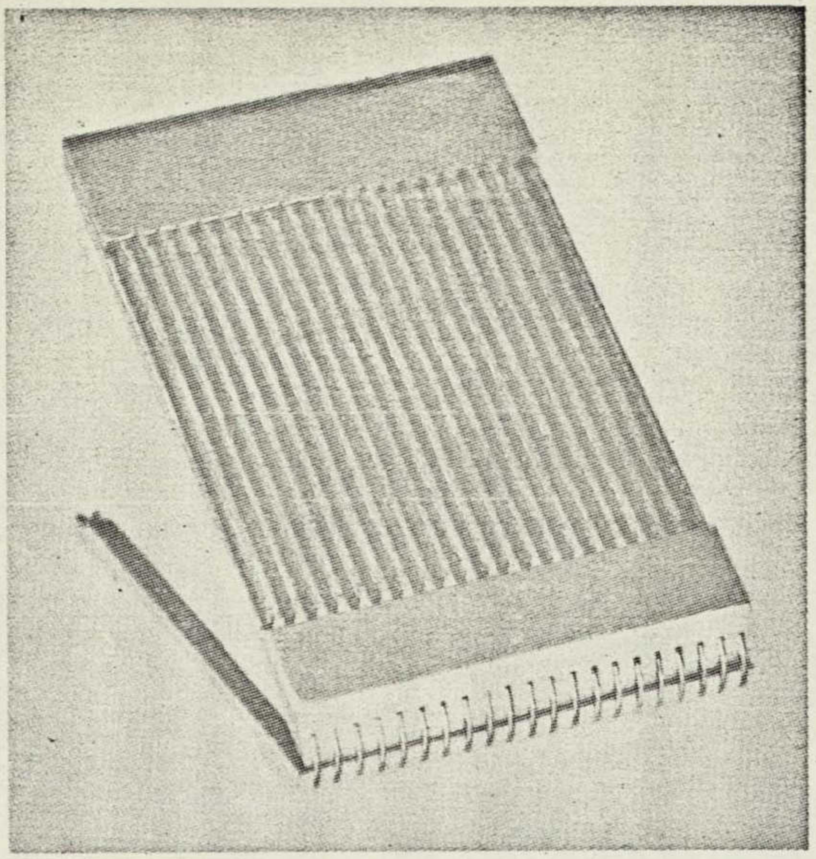

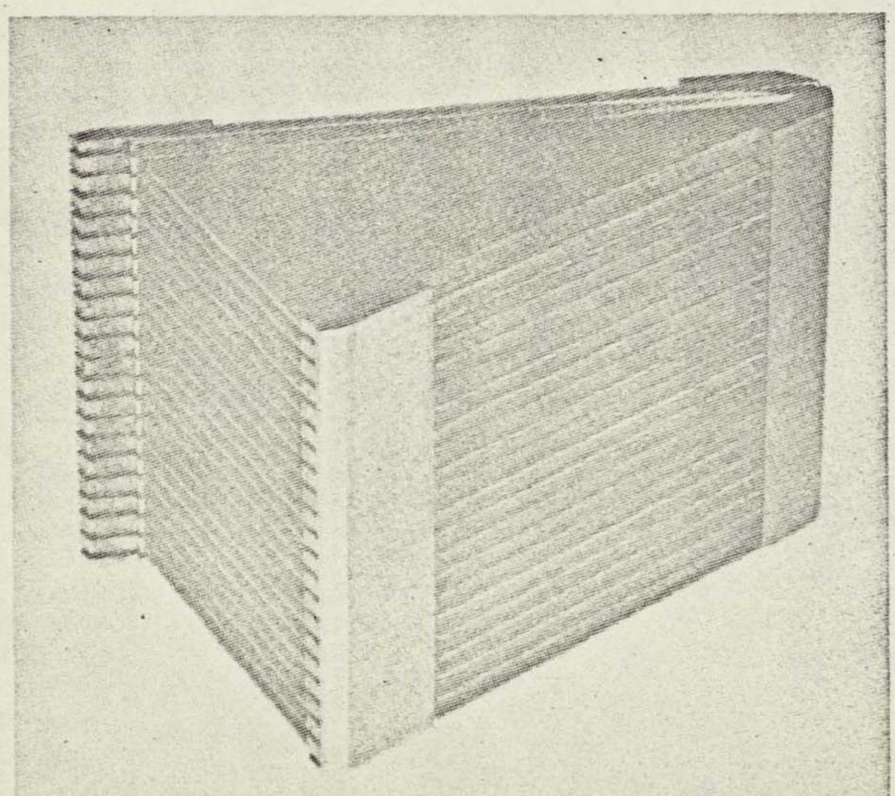

Figure 3.28. INFRARED YAW SENSOR, REFLECTIVE PYRAMID OPTIC

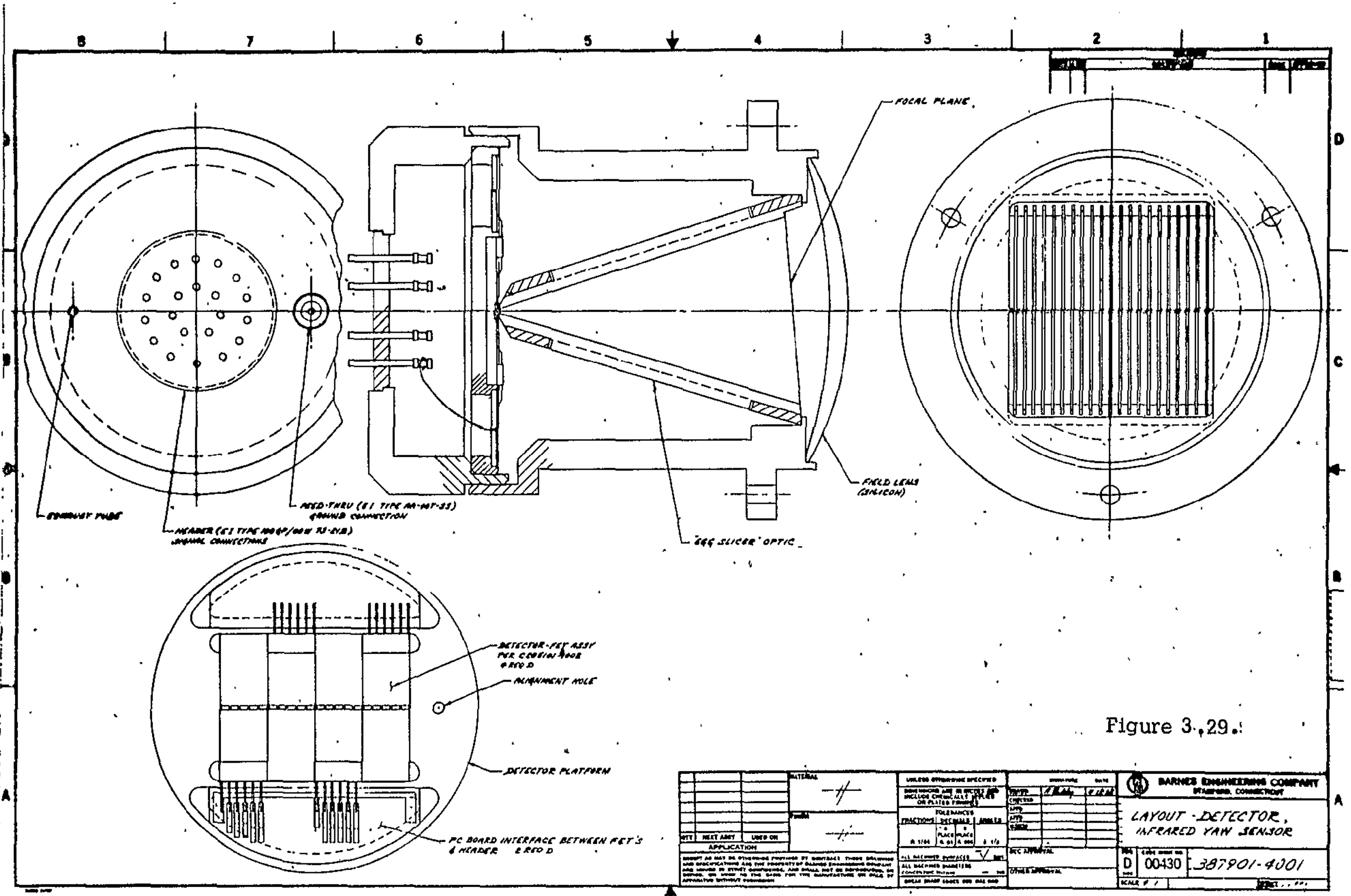
FOCAL PLANE
FIELD LENS (SILICON)
"EGG SLICER" OPTIC
FEED-THRU (E I TYPE AA-14T-33) GROUND CONNECTION
HEADER (E I TYPE 1006P/NEW 73-21B) SIGNAL CONNECTIONS
DETECTOR PLATFORM
ALIGNMENT HOLE
PC BOARD INTERFACE BETWEEN FET'S & HEADER 2 REQ D
APPLICATION
BARNES ENGINEERING COMPANY
STAMFORD, CONNECTICUT
LAYOUT - DETECTOR, INFRARED YAW SENSOR
D
00430
387901-4001

Figure 3.29.

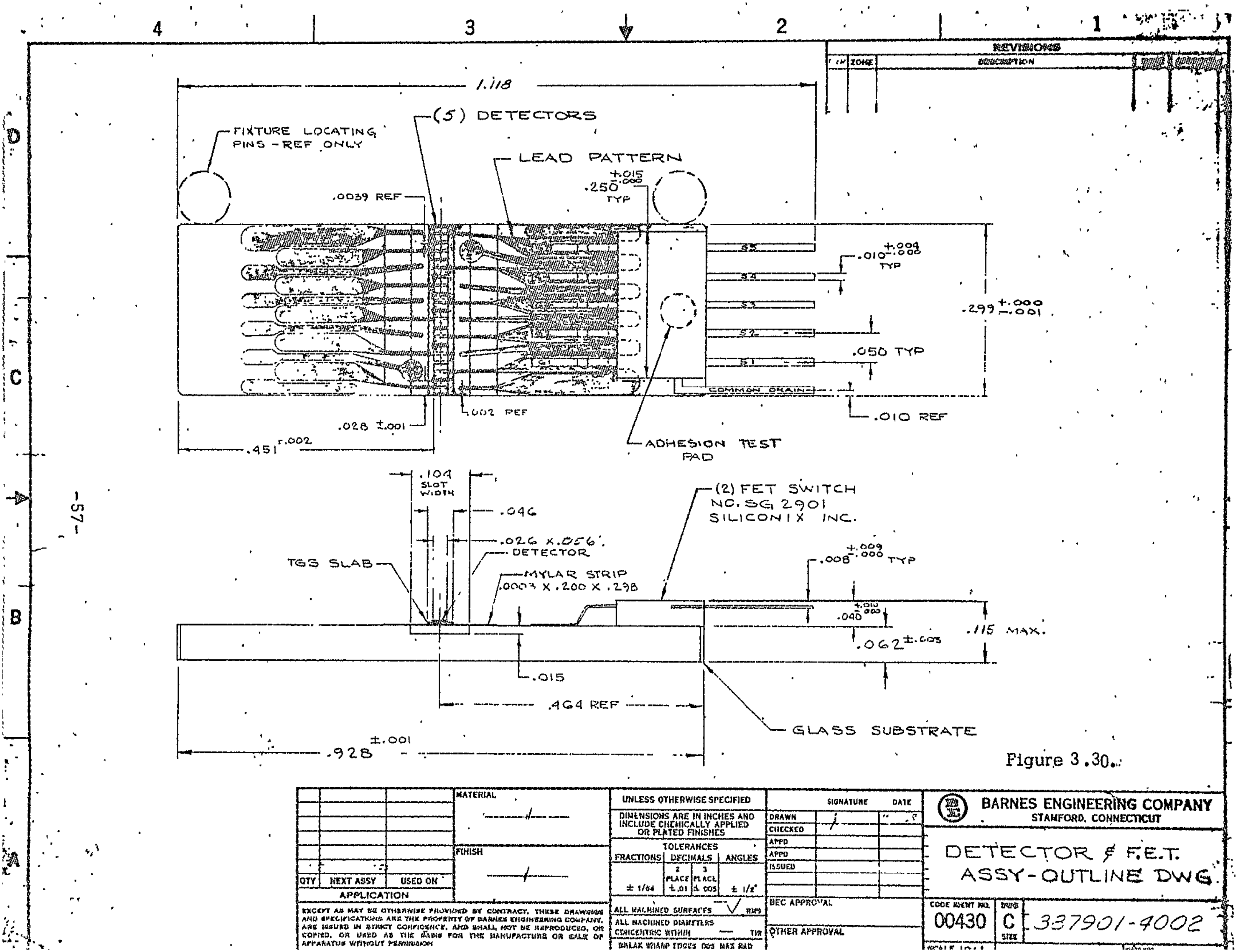
1.118
(5) DETECTORS
FIXTURE LOCATING PINS - REF ONLY
LEAD PATTERN
.0039 REF
.250 +.015 -.000 TYP
S5
S4
S3
S2
S1
COMMON DRAIN
.010 +.004 -.000 TYP
.299 +.000 -.001
.050 TYP
.010 REF
.002 REF
.028 ±.001
.451 ±.002
ADHESION TEST PAD
.104 SLOT WIDTH
.046
.026 X .056 DETECTOR
TGS SLAB
MYLAR STRIP .0003 X .200 X .298
(2) FET SWITCH NO. SG 2901 SILICONIX INC.
.008 +.009 -.000 TYP
.040 +.010 -.000
.115 MAX.
.062 ±.005
.015
.464 REF
GLASS SUBSTRATE
.928 ±.001
REVISIONS
ZONE
DESCRIPTION
MATERIAL
FINISH
QTY
NEXT ASSY
USED ON
APPLICATION
UNLESS OTHERWISE SPECIFIED
DIMENSIONS ARE IN INCHES AND INCLUDE CHEMICALLY APPLIED OR PLATED FINISHES
TOLERANCES
FRACTIONS
DECIMALS
ANGLES
2 PLACE
3 PLACE
± 1/64
±.01
±.005
± 1/2°
ALL MACHINED SURFACES
ALL MACHINED DIAMETERS CONCENTRIC WITHIN
BREAK SHARP EDGES .005 MAX RAD
SIGNATURE
DATE
DRAWN
CHECKED
APPD
APPD
ISSUED
BEC APPROVAL
OTHER APPROVAL
BARNES ENGINEERING COMPANY
STAMFORD, CONNECTICUT
DETECTOR & F.E.T. ASSY-OUTLINE DWG.
CODE IDENT NO.
00430
SIZE
C
337901-4002
EXCEPT AS MAY BE OTHERWISE PROVIDED BY CONTRACT, THESE DRAWINGS AND SPECIFICATIONS ARE THE PROPERTY OF BARNES ENGINEERING COMPANY, ARE ISSUED IN STRICT CONFIDENCE, AND SHALL NOT BE REPRODUCED, OR COPIED, OR USED AS THE BASIS FOR THE MANUFACTURE OR SALE OF APPARATUS WITHOUT PERMISSION

Figure 3.30.

As can be seen in Figure 3.30, the array is designed to mate with multiple field effect transistor elements housed in a "flat-pack" housing. These FET's provide the first amplifier stage (shown in Figure 3.31) for each pyroelectric element.

3.2.3.2 Pyroelectric Detector Array: Supplemental BAI Study

Since the cost of developing tooling, etc., for the pyroelectric array is very high, the Barnes effort has concentrated on an attempt to provide a design that will meet the requirements of the yaw sensor front end without requiring the development of a new pyroelectric configuration. This goal has a very high probability of being met by the use of an optical system that images the information from the predetermined angular intercepts onto an existing pyroelectric configuration. It should be noted that this optical design is universal and can be used regardless of the type detector that is finally chosen for the system. The use of a catadioptric array of this sort coupled with pyramidal optics provides a rather unusual appearance. For this reason, we felt that a discussion of the factors leading to this design might be very helpful.

The optical design uses a rectanguloid telescope (15" x 7.6" x 0.6") with a rectangular primary mirror (7.6" x 0.6"). This large anamorphism in the optical package is a logical consequence of the overall system requirements and is calculated to maximize system performance and to minimize system size.

The optical head is designed to gather infrared flux through a rectangular entrance pupil (a 7.6" x 0.6" aperture stop); it delivers this flux to a focal plane where it is divided into twenty adjacent 0.066" x 1.3" strips by twenty rectangular field stops. The long axis of each field stop is perpendicular to the long axis of the entrance pupil. The flux from each 0.066" x 1.3" field stop is then condensed onto an infrared detector that is 1.4 mm x 0.66 mm in size with its long axis parallel to the long axis of the entrance pupil. Thus the infrared flux is channeled through three rectangular stops: the aperture stop, a field stop, and a detector; it should be noted that the product of corresponding aspect ratios of these three stops is close to unity:

$$\frac{7.6''}{0.6''} \times \frac{0.066''}{1.3''} \times \frac{0.66\text{ mm}}{1.4\text{ mm}} = 3$$

It can be shown that achievement of maximum system sensitivity requires that the product of the aspect ratios of these three stops should approximate unity.* In principle, departures from a unity product sacrifice system sensitivity by the square root of the product. These design criteria are consequences of

*A general theorem demonstrating this is proved in Appendix 3.

Lagrange's Law*, **, which states that the angle of convergence of a flux ray on any image plane is inversely proportional to the linear size of the image at that focal plane. In practice it is frequently desirable to use system aspect products of the order of 4 due to engineering constructional constraints and reliability considerations; however, aspect products of as much as 9 are rarely justifiable since they produce such a large loss of sensitivity.

It must be appreciated that system requirements of the yaw-sensor dictate that the intercepts of each detector be $1/4^{\circ} \times 5^{\circ}$, an aspect ratio of 20:1. As pointed out above, maximum sensitivity required that the dissymmetry product of the system elements approach unity. This is achieved by the optical system proposed by Barnes in which the product of interest is:

$$\frac{7.6''}{0.6''} \times \frac{0.66 \text{ mm}}{1.4 \text{ mm}} = 6:1$$

which, when multiplied by the dissymmetry required of the field of view gives $\frac{6}{20} = 0.3$, a value 3 times away from unity. Thus, we make a permissible sacrifice of a factor of $\sqrt{3}$ in signal-to-noise in order to significantly simplify the system optics.

3.2.4 Electronic Design - Pyroelectric Detector

The electronic processing circuitry for the optical head amplifies the signal present at the output of each of the 20 elemental pyroelectric detectors, and sequentially samples the amplified signal output of each detector in the 20-element array. The resulting multiplexed signal is amplified to a suitable level in a logarithmic amplifier. The signal output of the logarithmic amplifier is then buffered and presented as the "video" output of the optical head.

3.2.4.1 Preamplifier

The output of each of the twenty detectors in the array is fed into a preamplifier similar to the one shown in Figure 3.31. The preamplifier consists of only two stages: a gain stage and an impedance buffer. Between these two stages and following the buffer stage are RC networks used to provide the required treble boost frequency response for the detector-amplifier system.

---

*"The Principles of Optics" by A. C. Hardy & F. H. Perrin: McGraw Hill Book Company, N. Y., 1932, see pages 43 and 93.

**"Wedge-Immersed Thermistor Bolometer" by M. G. Dreyfus; Applied Optics, Vol. 1, pages 615-619, September 1962.

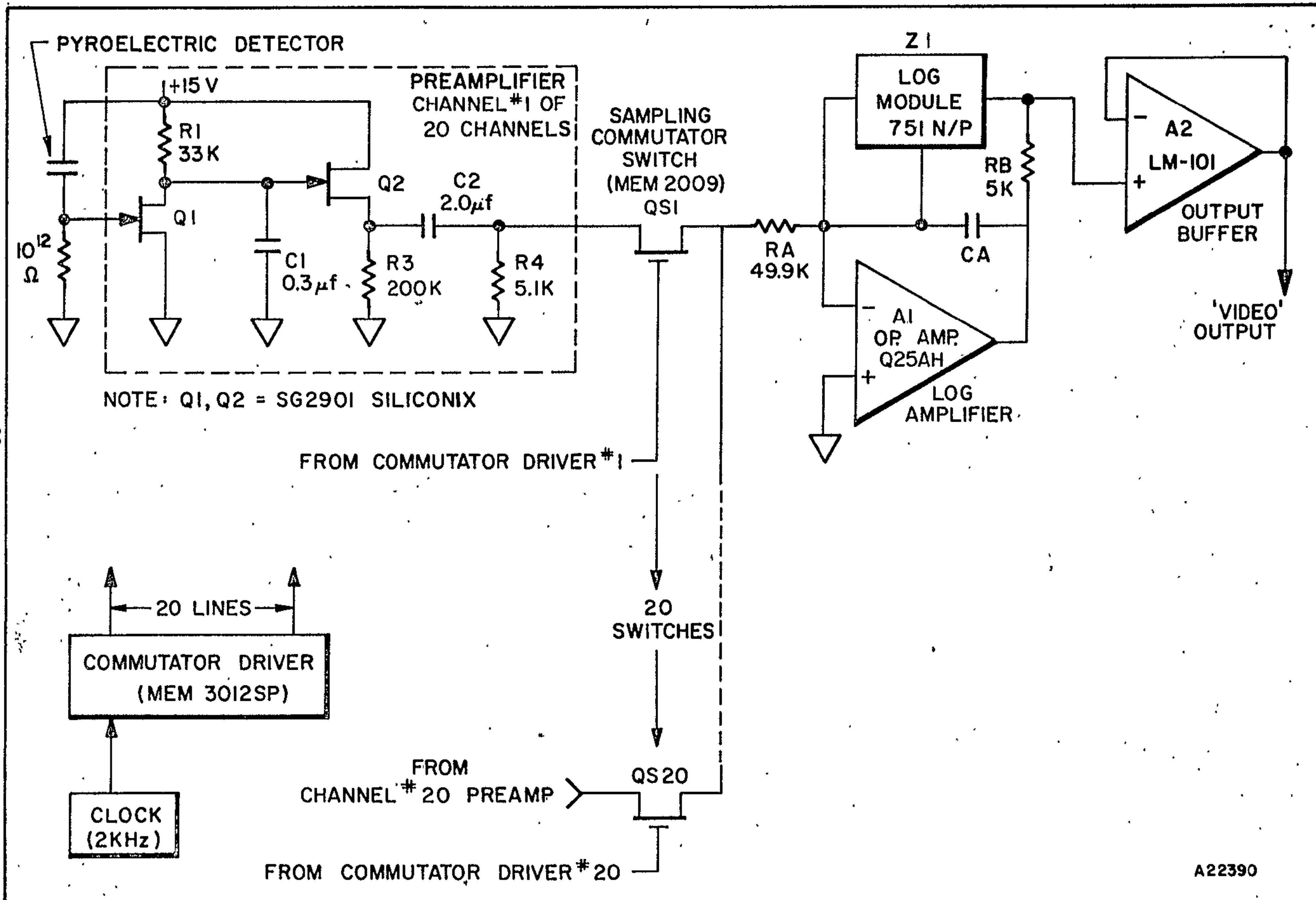

Figure 3.31. INFRARED YAW SENSOR SIGNAL PROCESSING

The output of each detector is fed into the high-impedance input of the first stage of the preamplifier. This first stage consists of a low-noise, high-gain, n channel FET (Q1). The amplified signal is taken at the drain of Q1 and is subsequently low-pass-filtered as a result of the configuration of resistor R1 and capacitor C1. The low-pass filter 3-db frequency is set at 16 Hz. This filtered signal is then fed into the buffer stage that consists of another FET between the output of each preamplifier and the input to the wide-band logarithmic amplifier, which will be described subsequently. Thus as each MOSFET switch is closed in sequence, the outputs of the 20 preamplifiers are presented in a serial fashion to the common source, which is the input to the log amplifier. These switches are driven in sequence from the 20 outputs of a commutator driver, which is discussed below. Each switch is closed in sequence for 500 microseconds; therefore, at the end of 10 milliseconds, each of the 20 preamplifier outputs is sampled once.

The values of components C2 and R4 in the preamplifier are selected so that the switching spikes appearing at the input to the log amplifier are at a level three times lower than the minimum expected output signal (which is equivalent to a planet radiance change of 0.5°C in a 100°K blackbody). Since the spikes are of such a low magnitude, their associated decays are also of no concern. Thus the switching transients produced by the commutator will not significantly affect the signal input to the logarithmic amplifier.

3.2.4.2 Commutator Driver

The commutator driver required to drive the 20 commutator switches described above consists of two General Instrument (MEM 3012 SP) shift registers. Application of a 2000-Hz clock to the input of the two registers, which are connected in series, produces the proper timing output to drive the commutator switch.

3.2.4.3 Clock and Power Supply

The power supply required to power all the electronics is of a conventional design and, therefore, not described in detail. The clock signal required to drive the shift registers is supplied by the BAI electronics.

3.2.4.4 Logarithmic Amplification

The output of the sampling commutator switch or multiplexer is fed into a five-decade logarithmic amplifier. This type of amplification is required because of the large dynamic range of the input radiation signal to the system.

Since the logarithmic amplifier input is a multiplexed version of the signals appearing at the outputs of the 20 preamplifiers, the logarithmic amplifier requires a bandwidth which extends from dc to 2000 Hz. A schematic of the proposed amplifier is also shown in Figure 3.31.

The logarithmic amplifier consists of a precision logarithmic device Z1 (Analog Devices Model 751 P/N) imbedded in the feedback loop of a high quality operational amplifier A1 (Philbrick Q25AH). The voltage input to this amplifier is converted to a current by resistor R_A. As a result, the amplifier has a transfer characteristic that is calibrated in steps of 1 volt per decade. Due to its configuration, the output of this amplifier is at a relatively high impedance, and is therefore fed into another stage that acts as a buffer. This buffer consists of an integrated operational amplifier such as the LM 102. The output of this buffer, A2, is the "video" output of the optical head.

Since the most critical portion of the logarithmic amplifier is the logarithmic device imbedded in the feedback loop, it is suggested that an Analog Device's Model 751 P/N precision logarithmic module be used. This selection is based on the fact that this module has a very wide dynamic range and is temperature compensated. The frequency response of the logarithmic amplifier is dictated by the bandwidth of the operational amplifier used in conjunction with the logarithmic device. The Q25AH is more than adequate to achieve the required 2000-Hz bandwidth.

3.3 STUDY OF SYSTEM PARAMETERS

3.3.1 Introduction

It is a truism to state that in any system in which information (in this case specifically, input data) is being processed, system sensitivity is a relatively simple, monotonic function of signal-to-noise ratio. As a result, a study of system parameters is properly a study of those factors contributing to improvement of signal-to-noise ratio.

The proposed yaw sensor consists of two separately analyzable sections: the IR front end with its optics, sensors, and immediately associated electronics as one section, and the video processor, system memory, and correlator with its associated integrators as the other section.

Appreciating this, the task assigned by BAI to Barnes specified a minimum allowable signal-to-noise ratio. The analysis made by Barnes showed system limitations (in terms of the absolute temperature of the terrain being examined and the expected ΔT) for a signal-to-noise ratio of 10:1, which was extrapolated for a 1:1 signal-to-noise ratio. Knowing that the video signal provided by the Barnes front end would be at a known signal-to-noise ratio, the study made by BAI was effectively heuristic rather than analytic, since our investigations in the past have determined that the BAI correlator cannot be analyzed accurately by any yet developed paper and pencil technique.*

The heuristic approach used is based on data that has been established on previous correlators and is dependent on the following relationships:

(1) Using the "standard" BAI scanning technique, the system sensitivity is maintained at one micron at the image plane at signal-to-noise ratios approaching 2:1.

(2) An analysis made in the original proposal for the yaw sensor (and summarized in Section 2.4 of this report) showed the expected deterioration of performance from the "standard" scanning system. This analysis was based on the parameters we now feel we can "freeze", that is, 20 elements in the IR array scanned at the rate of 100 scans per second. Therefore, the results of this analysis are as valid now as they were during the proposal phase of the program. This analysis predicted a reduction in system sensitivity at the image plane of a factor of 7.5, indicating that for a 20-element area subtending a total of $5^{\circ} \times 5^{\circ}$, system yaw sensitivity would be 0.25°.

Thus, it is immediately obvious that any improvement in the ability of the correlator system to accept a lower signal-to-noise ratio at the video input without a reduction in sensitivity will result in extended system performance. This extension of system performance can be taken advantage of in one of two ways. The increased sensitivity can be used directly to obtain thresholds of below $1/4^{\circ}$ of yaw, or it can be used to extend system operation so that terrain with even lower contrast and lower information content than that postulated in the Barnes analysis could be used to provide processible information to the system at thresholds of $1/4^{\circ}$ of yaw.

---

*Investigations have been made to determine the applicability of digital computer modeling to determining and predicting performance of the BAI correlator. As part of the Lunar Orbiter Program, experience by Eastman Kodak, using then in-house computers, showed that, whereas it was possible to approximate such a model for the correlator, the results could easily be in error by a full order of magnitude. BAI has discussed some of these problems further with Mr. Sam Pines of Astro Consultants, and as of early in 1968, Mr. Pines felt that the BAI correlator could be completely and accurately modeled on a general-purpose computer at a cost of about $65,000 for programming. In addition, many hours of time on a computer would be required. At the time of the estimate, Mr. Pines was thinking in terms of an IBM 7090. Later computers, now available, might simplify the task somewhat.

3.3.2 Memory Noise

The signal-to-noise ratio of the correlation portion of the system processing is controlled by two major factors. One is the repeatability or the validity of the information obtained from the system memory. Previous BAI systems employed a rotating drum memory. The information read from a stable non-jittering drum differs from that read into the drum due to variations in time constant of the reading and writing circuits and noise introduced by non-uniformity of the magnetic coating of the drum. While the effect of the variation of the time constant from the writing cycle to the reading cycle can be greatly diminished by the use of compensating time delays, there are second order residuals due primarily to temperature variations in the basic time controlling parameters and the corrections for them. Variations due to non-uniformity of drum coating can be reduced only by careful control of the manufacturing processes in making the drum and coating it. Because of this, BAI makes all of its own drums, and we feel that we have reduced variations due to coating noise to the minimum obtainable for a drum-type memory. It is our estimate that the contribution to uncertainty (i.e., system noise) attributable to drum non-uniformity and time constant variations between reading and writing are about equal and amount to somewhere between two and five parts per 100,000 each. Thus in a 10 millisecond scan, these noise sources introduce variations of from 200 nanoseconds to 500 nanoseconds each, a non trivial contribution when attempting to push toward maximum resolution.

A much more significant contribution to system noise by a drum-type memory results from the impossibility of obtaining a completely "smooth" rotational motion with a motor-driven drum. BAI has done extensive work in this area, particularly in the design and construction of test equipment for measuring high precision V/H systems where very high speed, high gain servos are used to control test systems in which large inertias are used for smoothing. Even under these tightly controlled circumstances, there are appreciable spurious signals generated by high time derivatives of the drum rotational rate. Since these higher derivatives are even greater when an open-loop, non-servo controlled motor is used, and further they are not repetitive due to bearing noise, etc., the information read from the drum is not identical to that written on the drum because of this uncontrolled jitter. (See next paragraph for a quantitative analysis of their effect.) For this and many other reasons, BAI intends to use an all-electronic memory for the proposed yaw sensor. (The original basis for the decision to use the all-electronic memory was elimination of mechanical rotating components and all of the lubrication and bearing problems associated with them in a space environment. Fortuitously, there is a strong additional advantage of reduction in system noise.) The proposed digital memory technique has the advantage of eliminating variations in memory output from one reading to the next, and reducing variations from input to output to less than the chosen time quantizing element. Since the size of this time quantizing element is within the control of the designer and can be made negligibly small with available building blocks at no appreciable sacrifice of system size or power, we can effectively eliminate noise contributions ascribable to the system memory by use of the proposed digital techniques. In an attempt to establish some numerical values for the improvement resulting from the use of a digital memory instead of a drum memory, we find the following:

The motor used to drive the memory drum in the Lunar Orbiter correlator was chosen primarily from the point of view of size, weight, and power. As a result, there was a large amount of jitter in the memory, much more than would be accepted on a ground-based, laboratory-type system. A much more meaningful comparison can be made with the jitter developed by the motor used for the memory drive in the system developed by BAI for the USGS. In this system there was no constraint on size, weight, or power; hence, we were able to reduce jitter to what we consider to be the lowest practicable value for an open loop system. This amounted to between 3 and 5 microseconds peak variation from one reading of the memory to the next.

Using a digital memory, the jitter from one reading to the next is reduced to the variation in the system clock rate; this is easily maintained in the low nanosecond region. For example, a one megacycle oscillator (which would be typical for a system of this sort) that varies by a few nanoseconds in 10 milliseconds (which would be a typical scan time) would be a very poor oscillator indeed. The state of the art today is appreciable better than this even for miniaturized oscillators.

The variation between information read into the memory and that read out is a function of the minimum time quantizing unit, and this can be reduced to almost any arbitrarily small size. A 5-megacycle system clock is readily available, and this would provide time quantizing elements of 200 nanoseconds each, meaning that the maximum variations between information read into a memory and that read out from the memory would be 200 nanoseconds maximum, with an average variation of about 100 nanoseconds.

3.3.3 Correlator Noise

The second source of processing noise is contributed by the correlator. Here again there are two sources of noise. The correlator requires the use of two matched delays, one in the video and the other in the reference channel. Any variations between these two delays introduces correlator noise. Although the two delays can be trimmed very carefully when the system is first built, drifts arise due to aging and temperature variations. The digital correlator that will be used on the yaw sensor substitutes a simple capacitor controlled delay for the original LC delay line. The tracking of the capacitors (when properly chosen) can be made appreciably better than that of the LC delay lines, which have inherent variation in core inductance and wiring tension, both of which are non-tracking and can introduce relatively large divergence between the two delay channels after temperature and time cycling. Past experience shows that these divergences can approach one microsecond with LC delays. The capacitor-controlled delays can be made to track to within 50 to 100 nanoseconds.

An equally important contribution to correlator noise results from the uncertainty of establishing the time position of leading and trailing edges of the pulses being compared in the correlator. The original correlator systems, which gave the basic data from which the parameters of one micron sensitivity at a signal-to-noise ratio of 2:1 were determined, had rise and fall times of approximately 500 nanoseconds. The newly developed digital correlator has rise and fall times of from 30 to 50 nanoseconds.

Each of these improvements contributes a reduction in signal-to-noise ratio that is approximately equal to the square root of the improvement ratio. Thus since each will effect an improvement of about a factor of 10, the reduction in signal-to-noise of each taken individually is about 3.3 times. The effect of two taken together must be determined experimentally, since there will undoubtedly be other residual contributions to noise that will limit the total improvement achievable in practice.

3.4 STUDY OF CROSS TALK DUE TO ROLL RATE*

3.4.1 Phase 1

In order to study the expected variations in yaw sensor image motion, a program was developed to simulate the motion of space vehicles for typical geocentric and lunar orbiter trajectories. This program obtained the position and velocity of a vehicle in closed form as a function of time, under the action of a central force field and a planetary oblateness perturbation. The program also generated the orientation of the vehicle body with respect to the local horizon, and periodically rotated the body axes, by means of impulses, to correct for pitch, roll, and yaw. The objective of this phase of the study was to determine the expected number of attitude corrections, and the time distribution of such corrections, for a perfectly stabilized vehicle.

In Phase II (which is described in Section 3.4.2), the program was modified to simulate the yaw sensor image motion due to vehicle side motion and roll rate. In addition, the attitude corrections were carried out in finite time (rather than with impulses) to obtain a more realistic body angle rate picture.

*Section 3.4 was prepared by Mr. Samuel Pines of Astro Consultants, Inc.

THE VEHICLE TRAJECTORY

We represent the motion of a vehicle in a rigidly rotating Kepler ellipse which simultaneously rotates about the planetary polar axis and about its instantaneous orbit plane normal vector.

We take as the defining parameters the initial position (R_{oo}) and velocity $(\dot{R}_{oo})$ vectors at the initial epoch (t_o). The simultaneous rigid rotation of these two vectors will represent the rigid rotations of our "mean" conic section.

The rotation of a vector, L, about a given unit vector, $\hat{M}$, through an angle, σ, is given by

$$L' = L + (1 - \cos\sigma)\hat{M} \times (\hat{M} \times L) + \sin\sigma \, \hat{M} \times L \tag{1}$$

The rotation is available as a matrix transformation also by

$$L' = A(\hat{M}, \sigma) L \tag{2}$$

where the elements of A are given by

$$\begin{aligned} a_{ij} &= \cos\sigma \, \delta_{ij} + (1 - \cos\sigma) m_i m_j + \sin\sigma \, m_k \delta_{ijk} \\ \delta_{ij} &= \begin{bmatrix} 0 & , & i \neq j \\ 1 & , & i = j \end{bmatrix} \\ \delta_{ijk} &= \begin{bmatrix} 0 & , & i = j \\ 1 & , & i \neq j \\ -1 & , & i \neq j \end{bmatrix} \begin{matrix} \\ \text{and cyclic with } 3,2,1 \\ \text{and cyclic with } 1,2,3 \end{matrix} \end{aligned} \tag{2a}$$

The advance of perigee about the instantaneous angular momentum vector may be represented by a rigid rotation of both the initial position vector, R_{oo}, and the initial velocity vector, $\dot{R}_{oo}$, through the same angle. The unit rotation vector is taken to be the unit initial angular momentum vector, $\hat{H}_{oo}$.

$$\hat{M}_1 = \hat{H}_{oo} = \frac{R_{oo} \times \dot{R}_{oo}}{h_o} = \begin{bmatrix} h_1 \\ h_2 \\ h_3 \end{bmatrix} \tag{3}$$

The mean rotation angle for the advance of perigee may be obtained following Brouwer[1] as

$$\sigma_1 = -\frac{3\, n_o\, \mu^2 (1 - 5 \cos^2 i_o)\, k_2 (t - t_o)}{2\, h_o^4} = s_1\, k_2 \tag{4}$$

where

$$n_o = \sqrt{\frac{\mu}{a_o^3}}$$

$$\frac{1}{a_o} = \frac{2}{r_o} - \frac{v_o^2}{\mu}$$

$$\cos i_o = h_3$$

k_2 = oblateness constant

μ = central mass constant

$t - t_o$ = transit time from initial time

$$r_o = |R_{oo}|$$

$$v_o = |\dot{R}_{oo}|$$

$$h_o = |R_{oo} \times \dot{R}_{oo}|$$

[1] Brouwer, D.; "Solution of the Problem of an Artificial Satellite Without Drag," Astronomical Journal, November 1959.

We have

$$
\begin{aligned}
R_o' &= A_1(\hat{H}_{oo}, \sigma_1) R_{oo} \\
\dot{R}_o' &= A_1(\hat{H}_{oo}, \sigma_1) \dot{R}_{oo}
\end{aligned}
\tag{5}
$$

The mean rotation of the ascending node may be represented by a rigid rotation of both R_o' and $\dot{R}_o'$ about the unit polar axis, $\hat{k}$. For this case, following Brouwer, we have

$$
\sigma_2 = - \frac{3 \mu^2 n_o \cos i_o \, k_2 (t - t_o)}{h_o^4} = s_2 \, k_2 \tag{6}
$$

The unit rotation vector is

$$
\hat{M}_2 = \hat{k} = \begin{bmatrix} 0 \\ 0 \\ 1 \end{bmatrix} \tag{7}
$$

$$
A_2(\hat{k}, \sigma_2) = \begin{bmatrix} \cos \sigma_2 & -\sin \sigma_2 & 0 \\ \sin \sigma_2 & \cos \sigma_2 & 0 \\ 0 & 0 & 1 \end{bmatrix} \tag{8}
$$

The desired result is given by a single matrix rotation, as follows.

Let

$$
C = A_2(\hat{k}, \sigma_2) \, A_1(\hat{H}_{oo}, \sigma_1) \tag{9}
$$

The elements of the matrix C are given below.

$$c_{11} = \cos\sigma_1 \cos\sigma_2 + (1-\cos\sigma_1)(h_1^2 \cos\sigma_2 - \sin\sigma_2\, h_1 h_2) - h_3 \sin\sigma_2 \sin\sigma_1$$

$$c_{12} = -\sin\sigma_2 \cos\sigma_1 + (1-\cos\sigma_1)(h_1 h_2 \cos\sigma_2 - h_2^2 \sin\sigma_2) - h_3 \cos\sigma_2 \sin\sigma_1$$

$$c_{13} = \cos\sigma_2 \sin\sigma_1\, h_2 + \sin\sigma_1 \sin\sigma_2\, h_1 + (1-\cos\sigma_1)(h_1 h_3 \cos\sigma_2 - h_2 h_3 \sin\sigma_2)$$

$$c_{21} = \sin\sigma_2 \cos\sigma_1 + (1-\cos\sigma_1)(h_1^2 \sin\sigma_2 + h_1 h_2 \cos\sigma_2) + \cos\sigma_2 \sin\sigma_1\, h_3$$

$$c_{22} = \cos\sigma_1 \cos\sigma_2 + (1-\cos\sigma_1)(h_2^2 \cos\sigma_2 + h_1 h_2 \sin\sigma_2) - \sin\sigma_1 \sin\sigma_2\, h_3 \qquad (9a)$$

$$c_{23} = \sin\sigma_1 \sin\sigma_2\, h_2 - \cos\sigma_2 \sin\sigma_1\, h_1 + (1-\cos\sigma_1)(h_1 h_3 \sin\sigma_2 + h_2 h_3 \cos\sigma_2)$$

$$c_{31} = h_1 h_3 (1-\cos\sigma_1) - \sin\sigma_1\, h_2$$

$$c_{32} = h_2 h_3 (1-\cos\sigma_1) + \sin\sigma_1\, h_1$$

$$c_{33} = \cos\sigma_1 + h_3^2 (1-\cos\sigma_1)$$

Then

$$\begin{aligned} R_o &= C\, R_{oo} \\ \dot{R}_o &= C\, \dot{R}_{oo} \end{aligned} \qquad (10)$$

The solution of the two-body problem is now available as

$$\begin{aligned} R(t) &= f\, C\, R_{oo} + g\, C\, \dot{R}_{oo} \\ \dot{R}(t) &= \dot{f}\, C\, R_{oo} + \dot{g}\, C\, \dot{R}_{oo} \end{aligned} \qquad (11)$$

The scalar functions f, g, $\dot{f}$ and $\dot{g}$ are given by the standard formulae:

$$f = 1 - \frac{G_2}{r_o}$$

$$g = \frac{r_o}{\sqrt{\mu}} G_o + \frac{d_o}{\mu} G_2 \tag{12}$$

$$\dot{f} = - \frac{\sqrt{\mu}\ G_1}{r_o\, r}$$

$$\dot{g} = 1 - \frac{G_2}{r}$$

Here, we have

$$d_o = R_{oo} \cdot \dot{R}_{oo}$$

$$r = |R| = G_2 + r_o G_o + \frac{d_o}{\sqrt{\mu}} G_1 \tag{13}$$

$$d = R \cdot \dot{R} = \sqrt{\mu}\ (1 - \frac{r_o}{a_o}) G_1 + d_o G_o$$

The G_i functions are the Stumpff series

$$G_i = \beta^i \left(\frac{1}{i\,!} - \frac{\beta^2}{a(i+2)!} + \frac{\beta^4}{a^2(i+4)!} \cdots \right) \tag{14}$$

The relationship between the regularizing eccentric anomaly β and the transit time, $t - t_o$, is given by

$$\sqrt{\mu} \left(1 - \frac{3\ \mu^{3/2}(1 - 3\ \cos^2 i_o) k_2}{2\ a_o^{1/2}\ h_o^3} \right) (t - t_o) = G_3 + r_o G_1 + \frac{d_o}{\sqrt{\mu}} G_2 \tag{15}$$

Here, the mean anomalistic period may be interpreted as a somewhat altered central body mass constant.

To obtain a solution of the two-body problem, we proceed as follows:

1. Given a fixed transit time, $t-t_o$, we solve the modified Kepler's equation (15) by Newton's method for the unknown anomaly, β.

$$\beta_i = \beta_{i-1} + \frac{\sqrt{\mu}\,(t-t_o)(1+s_3 k_2) - \left[G_3 + r_o G_1 + \frac{d_o}{\sqrt{\mu}} G_2\right]_{\beta_{i-1}}}{\left[G_2 + r_o G_o + \frac{d_o}{\sqrt{\mu}} G_1\right]_{\beta_{i-1}}} \qquad (16)$$

where

$$s_3 = -\frac{3\,\mu^{3/2}(1-3\cos^2 i_o)}{2\,a_o^{1/2}\,h_o^3}$$

2. For a converged β, compute the $G_i(\beta, \frac{1}{a})$ series

3. Compute $f, g, \dot{f}, \dot{g}$

4. Compute the rotation matrix C

5. Compute R and $\dot{R}$ from eq. (11).

VEHICLE ATTITUDE CONTROL

The vehicle $\hat{i}$ axis is pointed down range in the plane of the orbit. Rotation about $\hat{i}$ controls roll. The vehicle $\hat{j}$ axis is pointed normal to the orbit plane. Rotation about $\hat{j}$ controls pitch. The vehicle $\hat{k}$ axis is pointed vertically up in the direction along the radius vector from the center of the planet.

In a perfectly aligned vehicle, we have

$$\hat{i} = \frac{H \times R}{hr}$$

$$\hat{j} = \frac{H}{h} \qquad (17)$$

$$\hat{k} = \frac{R}{r}$$

To compute the pitch angle, we determine the angle that we must rotate the $\hat{i}$ axis about $\hat{j}$ to cause the rotated $\hat{i}'$ axis to be perpendicular to the position vector.

$$\hat{i}' \cdot R = 0 = \cos \sigma_p \, \hat{i} \cdot R - \sin \sigma_p \, \hat{k} \cdot R$$

$$\tan \sigma_p = \frac{\hat{i} \cdot R}{\hat{k} \cdot R} \qquad (18)$$

Similarly, the roll angle is the angle required to rotate $\hat{j}$ about $\hat{i}$ until $\hat{j} \cdot R = 0$.

$$\hat{j}' \cdot R = 0 = \hat{j} \cdot R \cos \sigma_r + \hat{k} \cdot R \sin \sigma_r$$

$$\tan \sigma_r = -\frac{\hat{j} \cdot R}{\hat{k} \cdot R} \qquad (19)$$

If we could determine yaw exactly, it would be the angle we must rotate the $\hat{i}$ axis about $\hat{k}$ in order to make the angle between $\hat{i}'$ and the unit $\frac{H \times R}{hr}$ vector a minimum. Find σ_y so that

$$\cos \alpha = \hat{i}' \cdot \frac{H \times R}{hr} = \cos \sigma_y \frac{H \times R}{hr} \cdot \hat{i} + \sin \sigma_y \frac{H \times R}{hr} \cdot \hat{j} = \min \tag{20}$$

or

$$\tan \sigma_y = \frac{\hat{j} \cdot H \times R}{\hat{i} \cdot H \times R}$$

As the vehicle proceeds along its trajectory, the three angles are computed and corrections are carried out whenever any angle exceeds $\pm .05^{\circ}$. The new body axes are given by

$$[\hat{i}', \hat{j}', \hat{k}'] = \begin{matrix} A_p(\hat{j}, \sigma_p) \\ A_r(\hat{i}, \sigma_r) \\ A_y(\hat{k}, \sigma_y) \end{matrix} [\hat{i}, \hat{j}, \hat{k}] \tag{21}$$

for pitch, roll and yaw, respectively.

COMPUTER STUDY RESULTS

Lunar Trajectory

Semi-major axis a	=	1100 miles = .275 Earth Radii
Eccentricity e	=	.003
Inclination i	=	3°
Flight Path Angle γ	=	0
Initial Radius r_o	=	$a(1-e)$

Oblateness Constant $k = 10^{-3}$

$\hat{i}_o = 0$

$\hat{j}_o = 0$

$\hat{k}_o = 0$

After 1.5 hours

pitch adjusts	roll adjusts	yaw adjusts
5400	2	3

Earth Orbit

$a = 4100$ miles $= 1.025$ Earth Radii

$e = .003$

$i = 40^o$

$\gamma = 0$

$r_o = a(1-e)$

k = Oblateness Constant, 10^{-3}

$\hat{i}_o = 0$

$\hat{j}_o = 0$

$\hat{k}_o = 0$

After .207 hours

pitch adjusts	roll adjusts	yaw adjusts
990	0	1

ANALYSIS OF THE RESULTS

A successful control system will require close control in pitch and roll in order to cut down the effects of cross-coupling in the pitch, roll and yaw degrees of freedom. If we desire a pitch control of $\pm .05^{\circ}$, we need to correct at an average rate of $360^{\circ}/1.5$ hours or $.067^{\circ}$/second in pitch for Earth orbit and $.05^{\circ}$/sec. for lunar orbits. For good pitch control, a figure of $.1^{\circ}$/sec. should prove adequate.

In the absence of pitch error, the yaw sensor image velocity is given by

$$\text{image vel} = \sigma_y v \cos\gamma + \dot{\sigma}_r \ell$$

where ℓ is the vehicle altitude and v is the vehicle speed. By integrating the image velocity, we get for the net lateral ground distance traversed

$$S = \sigma_y v \cos\gamma t + |\sigma_r(\text{max positive}) - \sigma_r(\text{min negative})| \ell$$

Thus, if we choose $\ell = 100$ miles, $\gamma = 0$, $|\sigma_r - \sigma_{r_o}| = 2\sigma_{r\,max}$, $v = 1.1$ miles/sec. for lunar orbits and 4.5 miles/sec. for Earth orbits, to control the yaw limits to the same limits set in roll and pitch ($\pm .05^{\circ}$), we need an integration time of 100 seconds in Earth orbit to be able to neglect the false yaw signal due to roll and 400 seconds in lunar orbit to be able to drown out the false roll signal. These time limits will be reduced linearly if the yaw limits are increased above $\pm .05^{\circ}$. The roll rate is not important in this study since it integrates out to give an oscillating signal whose maximum value is $2\sigma_{r\,max}$.

3.4.2 Phase 2

SUMMARY

This section contains the results of a simulation computer study of the BAI yaw sensor in typical geocentric and lunar orbits. Two possible feedback control schemes for limiting the vehicle yaw were investigated. The report shows that, with the use of a summation time of 30 seconds; the BAI yaw sensor can limit the true yaw excursion to $\pm 0.5^{\circ}$ for both earth and lunar orbits, with yaw and roll perturbations. Roll limit stops of $\pm 0.5^{\circ}$ do not adversely affect the BAI sensor in limiting yaw excursions to less than $\pm 0.5^{\circ}$.

INTRODUCTION

The Phase I study, described in Section 3.4.1, generated a computer program that produced realistic vehicle motions with perturbations in roll, yaw, and pitch to act as a test bed for building a simulation program for the BAI yaw sensor. This basic program was augmented to include the following:

a) A realistic, finite time correction scheme for the vehicle in pitch and roll to replace the impulsive correction mode used in Phase I.

b) A simulation for the BAI yaw sensor by producing a signal proportional to the net cross-track image distance traversed by the vehicle over the surface of the planet, including the effects of both yaw and roll rate.

c) A simulation of the BAI yaw sensor time delay in estimating the image motion.

d) A simulation of the BAI yaw sensor cross-track image measurement constraint of a maximum of $\pm 0.5^{\circ}$ of orbital central angle per image summation scan.

e) The program listed the estimated yaw as well as the actual yaw throughout the run. The components of the cross-track image motion due to roll rate are listed separately from the cross-track image motion due to yaw.

The program tested two options in yaw control as follows:

Option I: Estimated yaw is computed continuously and corrected at a linear rate of 0.02°/sec whenever the estimated yaw error is greater than $\pm 0.25^{\circ}$.

Option II: Estimated yaw is evaluated over a time arc of 30 seconds and corrected whenever the estimated yaw exceeds $\pm 0.25^{\circ}$ at a rate of 0.02°/sec. The accumulator is reset to zero every 30 sec. if the estimated yaw is less than $\pm 0.25^{\circ}$.

SIMULATION OF THE CROSS-TRACK IMAGE MOTION

Let the vehicle vector planeto-centric position in inertial Cartesian co-ordinates be $R(t)$, and the velocity vector be $\dot{R}(t)$. Let the planet surface radius be $\bar{r}$. Then the projected ground-speed across the planet surface is given by

$$v_{pgs} = v \cos\gamma \frac{\bar{r}}{r} \tag{1}$$

where $v = |\dot{R}|$, $r = |R|$ and γ is the flight path angle. The vector ground-speed is given by

$$V_{pgs} = \frac{(R \times \dot{R}) \times R}{r^2 v \cos\gamma} v_{pgs}$$

$$= \frac{\bar{r}}{r^3} H \times R \tag{2}$$

The cross-track image ground-speed for a stabilized vehicle, with zero roll rate, is given by the vector dot product of V_{pgs} into the lateral yaw sensor $\hat{j}$ axis.

$$v'_{ctim} = \frac{\bar{r}}{r^3} (H \times R) \cdot \hat{j} \tag{3}$$

The contribution of roll rate to the cross-track image motion is given by the product of the vehicle altitude above the ground and the roll rate.

$$v''_{ctim} = (r - \bar{r}) \dot{\sigma}_r \tag{4}$$

The net cross-track image velocity is given by the sum of the two factors

$$v_{ctim} = \frac{\bar{r}}{r^3} (H \times R) \cdot \hat{j} + (r - \bar{r}) \dot{\sigma}_r \tag{5}$$

The average value of this cross-talk image motion, taken over a one-second time interval is proportional to the BAI yaw sensor output. Since the yaw sensor wipes out its reference origin each time the vehicle covers a planetary central angle of 0.5°, the simulation must include this constraint.

An examination of Eq. (5) reveals that for small yaw angles, the contribution of the roll rate can give an erroneous yaw signal. In order to avoid this difficulty, it is proposed to integrate the BAI yaw sensor signal and take advantage of the roll-stop control to limit the fictitious yaw signal due to roll.

Integrating Eq. (5), we get the net cross-track image ground distance traversed

$$S(N) = \sum_{i=0}^{N} \left[\frac{\bar{r}}{r^3} (H \times R) \cdot \hat{j} \right] (t_i - t_{i-1}) + \sum_{i=0}^{N} (r - \bar{r})(\sigma_{r_i} - \sigma_{r_{i-1}}) \tag{6}$$

Since the roll angle is limited by the controlled roll-stops, we will obtain a yaw signal monotonic with time, over reasonably long time arcs. The method recommended in the study is to assume that the vehicle is at a constant yaw error over the summation time, with zero pitch and roll, and moving at circular velocity. Under these assumptions, the estimated yaw angle is given by

$$\sigma_{y_{est}} = \frac{S(N)}{\sqrt{\frac{\mu}{r}} \, (T_N - T_o)} \tag{7}$$

The control system is then triggered by the estimated yaw signal to wash out the estimated yaw error at a linear yaw correction rate of 0.02^{o}/sec whenever $\sigma_{y_{est}} > \pm 0.25^{o}$.

Since the true yaw error is not a constant over too long a time interval, it is necessary to determine the optimum length of time interval over which to integrate in order to get a good estimate of yaw error. A second problem which needs solving is to determine the magnitude of the trigger limit of yaw error in order to avoid obtaining an erroneous yaw signal due to roll rate. To study these questions, a series of computer runs were carried out for both geocentric and lunar trajectories with roll error-stops of $\pm 0.05^{o}$, $\pm 0.1^{o}$, and $\pm 0.5^{o}$. Two control options were tested. First, continuous summing between yaw corrections with estimated yaw corrected for yaw errors greater than $\pm 0.25^{o}$, and secondly, accumulating yaw sensor signals for periods of 30 seconds only, with corrections applied when the estimated yaw error is greater than $\pm 0.25^{o}$. The results are shown and discussed in the next section.

DISCUSSION OF TEST RESULTS

The initial conditions for lunar trajectory were:

semi-major axis a	=	1100 miles
average altitude $(r-\overline{r})$	=	100 miles
eccentricity e	=	.003
inclination i	=	3°
initial flight path angle γ	=	0°
initial radius r_o	=	$a(1-e)$

The initial vehicle orientation is

$$\hat{i}_o = \hat{j}_o = \hat{k}_o = 0$$

The initial conditions for the geocentric trajectory were:

semi-major axis a	=	4100 miles
average altitude $(r-\overline{r})$	=	100 miles
eccentricity e	=	.003
inclination i	=	40°
initial flight path angle γ	=	0°
initial radius r_o	=	$a(1-e)$

The initial body axes were taken as

$$R_o \cdot \hat{i}_o = R_o \cdot \hat{j}_o = (\hat{H} \times \hat{R})_o \cdot \hat{j}_o = 0$$

The yaw perturbations were sufficient to cause vehicle yaw of 5 arc-seconds per second.

The tables list the maximum true yaw deviation, the estimated yaw deviation at the beginning and at the end of each yaw correction. The time is in hours measured from the start of the yaw sensor experiment. The roll-stop limits, the yaw control option, and the central body are listed at the head of each table.

TABLE 1

Moon - Option I

Roll $\pm .05^{o}$

Time On Time Off hours	True Yaw deg.	Estimated Yaw deg.	Yaw Correction No.
.1508	-.283	-.283	
.1552	-.009	-.175	1
.2698	-.454	-.344	
.2750	-.129	-.216	2
.3560	-.424	-.268	
.3602	-.164	-.166	3
.8066	.450	.318	
.8116	.138	.197	4
.9064	.449	.261	
.9106	.186	.159	5

TABLE 2

Moon - Option I

Roll ±.10°

Time On Time Off hours	True Yaw deg.	Estimated Yaw deg.	Yaw Correction No.
.1322	-.239	-.250	
.1362	.007	-.160	1
.2578	-.463	-.250	
.2616	-.219	-.009	2
.2618	-.219	-.264	
.2658	.024	-.069	3
.4200	-.455	-.263	
.4242	-.190	-.159	4

TABLE 3

Moon - Option I

Roll ±0.5°

.1758	-.587	-.250	
.1796	-.349	.009	1
.1798	-.350	-.415	
.1860	.032	-.168	2
.3022	-.653	-.250	
.3060	-.414	.009	3
.3062	-.414	-.386	
.3120	-.055	-.148	4
.8188	.934	.250	
.8226	.691	-.009	5
.8228	.692	.591	
.8312	.136	-.004	6
.8314	.137	.279	
.8358	-.133	-.045	7

TABLE 4

Earth - Option I

Roll ±.05°

Time On Time Off hours	True Yaw deg.	Estimated Yaw deg.	Yaw Correction No.
.1970	-.300	-.250	
.2010	-.052	-.003	1
.2956	-.348	-.250	
.2996	-.103	-.219	2
.3772	-.366	-.341	
.3824	-.039	-.190	3
.4618	-.293	-.250	
.4658	-.045	-.150	4
.5690	-.302	-.265	
.5732	-.036	-.141	5
.9814	.360	.250	
.9854	.115	.232	6

TABLE 5

Earth - Option I

Roll ±.10°

.2016	-.340	-.250	
.2056	-.093	0	1
.3128	-.449	-.250	
.3166	-.203	.009	2
.3168	-.204	-.314	
.3216	.096	-.054	3
.4522	-.347	-.316	
.4570	-.045	-.176	4
.5582	-.293	-.257	
.5622	-.042	-.141	5
.9884	.414	.250	
.9922	.168	-.009	6
.9924	.169	.282	
.9968	-.103	.037	7

TABLE 6

Earth - Option I

Roll ±0.5°

Time On Time Off hours	True Yaw deg.	Estimated Yaw deg.	Yaw Correction No.
.2322	-.686	-.250	
.2360	-.445	.009	1
.2362	-.446	-.549	
.2442	.062	-.191	2
.3680	-.592	-.250	
.3718	-.352	.009	3
.3720	-.353	-.447	
.3786	.060	-.137	4
.5306	-.548	-.250	
.5344	-.297	.009	5
.5346	-.297	-.384	
.5404	.080	-.087	6
.9096	.632	.250	
.9134	.390	-.009	7
.9136	.391	.496	
.9210	-.077	.161	8

TABLE 7

Moon - Option II

Roll ±.05°

.1392	-.244	-.252	
.1430	.002	.006	1
.2294	-.322	-.260	
.2334	-.065	.014	2
.3196	-.404	-.268	
.3236	-.145	.005	3
.4344	-.452	-.254	
.4382	-.200	.005	4
.7378	.323	.259	
.7418	.080	.172	5
.8198	.398	.263	
.8240	.140	.169	6
.9264	.451	.253	
.9304	.200	.157	7

TABLE 8

Moon - Option II

Roll ±.10°

Time On Time Off hours	True Yaw deg.	Estimated Yaw deg.	Yaw Correction No.
.1392	-.262	-.266	
.1434	-.002	-.169	1
.2294	-.334	-.268	
.2336	-.077	-.175	2
.3196	-.411	-.272	
.3238	-.153	-.177	3
.4426	-.457	-.257	
.4466	-.203	-.157	4
.7296	.328	.269	
.7338	.071	.176	5
.8116	.382	.256	
.8156	.137	.167	6
.9182	.448	.252	
.9222	.198	.158	7

TABLE 9

Moon - Option II

Roll ±0.5°

.1064	-.239	-.259	
.1106	-.017	-.167	1
.1720	-.305	-.275	
.1764	-.043	-.185	2
.2458	-.332	-.256	
.2498	-.089	-.168	3
.3360	-.400	-.256	
.3400	-.151	-.162	4
.6804	.281	.264	
.6846	.023	.170	5
.7624	.362	.272	
.7666	.108	.181	6
.8444	.416	.263	
.8486	.156	.167	7

TABLE 10

Earth - Option II

Roll $\pm .05^{\circ}$

Time On Time Off hours	True Yaw deg.	Estimated Yaw deg.	Yaw Correction No.
.1884	-.276	-.265	
.1926	-.014	-.150	1
.2786	-.278	-.258	
.2826	-.032	-.153	2
.3524	-.281	-.253	
.3564	-.036	-.150	3
.4344	-.297	-.262	
.4386	-.036	-.150	4
.5410	-.317	-.274	
.5454	-.039	-.152	5
.9756	.279	.260	
.9798	.019	.148	6

TABLE 11

Earth - Option II

Roll $\pm .10^{\circ}$

.1802	-.277	-.266	
.1844	-.015	-.151	1
.2704	-.289	-.268	
.2746	-.030	-.158	2
.3524	-.300	-.272	
.3566	-.040	-.161	3
.4344	-.288	-.251	
.4384	-.042	-.149	4
.5328	-.292	-.252	
.5368	-.040	-.141	5
.9674	.289	.269	
.9716	.029	.158	6

TABLE 12

Earth - Option II

Roll ±0.5°

Time On Time Off hours	True Yaw deg.	Estimated Yaw deg.	Yaw Correction No.
.1392	-.278	-.265	
.1434	-.020	-.156	1
.2048	-.271	-.261	
.2090	-.009	-.144	2
.2868	-.272	-.250	
.2908	-.028	.148	3
.3606	-.297	-.266	
.3648	-.039	-.158	4
.4344	-.285	-.254	
.4384	-.038	-.146	5
.6066	-.296	-.255	
.6106	-.042	-.140	6
.8526	.283	.272	
.8568	.024	.162	7
.9182	.279	.258	
.9222	.038	.162	8
.9756	.280	.257	
.9796	.034	.156	9

Under Option I, true yaw deviations as high as .933 are possible. In addition, since this option estimates the yaw over a long summing time arc in a linear fashion, it tends to underestimate the true yaw. After reducing the yaw by $\frac{1}{4}$ of a degree, it immediately triggers the control again, realizing that the yaw deviation is not completely washed out. Option I is clearly not as good as Option II. Under Option II, which accumulates the yaw count over 30 seconds only, and re-initializes every 30 seconds, the BAI sensor does much better.

The maximum true yaw never exceeds 0.5° for either lunar or earth trajectories.

It appears that Option II is a possible mode of yaw control to limit the yaw deviation to less than 30°, with roll-stops as high as $\pm 0.5^\circ$.

3.5 STUDY OF TECHNIQUES TO ELIMINATE THE EFFECT OF ROLL RATE

3.5.1 Introduction

As indicated in Section 3.5, the analytic studies and computer simulation of Mr. Samuel Pines of Astro Consultants, Inc., (complemented by BAI investigations) have established that natural roll of the satellite under usual orbital conditions has a negligible effect on yaw sensor output. Only during the execution of a satellite roll correction (and perhaps not even then) is there a potential influence of roll rate on yaw sensor performance.

Hence, in view of the comparative infrequence and short duration of such correction, elimination of any potential roll rate effect would be most simply achieved by blanking the yaw sensor during roll-correction maneuvers. Provision for such blanking is shown in the preliminary system block diagram, Figure 4.6.

Prior to this analysis, it had been thought that roll effects would be a significant factor in yaw sensor performance. As a result, the contract statement of work called for an investigation of techniques for reducing such effects. As first outlined in Supplement 1 to our original Yaw Sensor proposal, three categories of techniques for reducing unwanted roll rate effects were considered:

(1) Use of an integrating time period wherein the + and - roll rates effectively cancel each other out.

(2) Use of a separate and additional IR yaw sensor instrument oriented obliquely to the basic yaw sensor.

(3) Exploration of other methods.

The results of these investigations are summarized below both for historical reasons, and, perhaps more importantly, to indicate potential solutions to the roll effect problem should the system ever be considered for use in orbit about a planetary body wherein the shape or mass distribution is significantly eccentric as to introduce appreciable roll effects.

3.5.2 Integration Time Period

Use of an integration time period was considered in quite some detail by both BAI and Astro Consultants. For this work, various parameter values and ranges were assumed. There was basic agreement on the relative merit of this method because of its simplicity, providing that the roll limit stop range and the maximum expected yaw rate values are compatible. It would appear that a 1/2-minute integration time period should reduce the roll rate induced error in the yaw data to less than 1/4-degree maximum, provided that $\pm 1/20$-degree roll stop limits are operative. This simple calculation assumes averaging of constant magnitude roll rates for a given lunar orbit. (An altitude of about 75 statute miles was assumed for this calculation.)

3.5.3 Second Oblique Yaw Sensor

BAI established basic parameters for a system that would use a second and independent IR yaw sensor to view the local surface obliquely from the main yaw sensor system. This method appears feasible for effectively eliminating roll rate induced error in the yaw sensor without integration under the following limitations:

A large oblique angle (α) is desired, $\sim 60^\circ$, since overall yaw detection sensitivity is a monotonically decreasing function of $\cos^2\alpha$.

Even for nominal 100-mi lunar orbit, a 60° angle seems practical with a resulting direct reduction in the overall system's yaw detectivity of about 30% due to the $\cos^2\alpha$ obliquity factor, and an indirect accuracy factor of $\sqrt{2}$ due to the use of two yaw sensor instruments in the system.

3.5.4 Other Methods

In this category the major attention was given to the use of a separate roll instrument that would independently and directly measure the vehicle's roll rate. The instrument considered was a solid-state (no-moving-parts) scanning device that would monitor the vehicle's space-coordinate roll rate relative to a randomly available star. This star-sensor approach seems particularly interesting and might well merit further study. The method appears to be accurate enough and at least no more complex than the use of a duplicate yaw sensor. Furthermore, it would degrade the yaw output of the overall system only as a secondary function of the uncertainties in the roll rate correction itself ($\sim \sqrt{2}$). The effective time constant required (1 to 5 seconds) is significantly less than the time required by the use of integration. This straightforward instrument does not require elaborate computers or star location information.

3.6 DESIGN OF BREADBOARD VISIBLE LIGHT FRONT END

A number of techniques were considered for simulating the array-multiplexer combination. Some of these would operate within the same frequency spectrum as the final system, that is, they would generate a video signal with maximum significant information between corners at 1 kc and 20 kc; others would operate at a much lower frequency and would require slow recording equipment to generate meaningful data (pen recorder or memo-scope type). Some of the techniques that were considered are:

(1) An array of simple visible light detectors such as cadmium sulfide and a simple multiplexer (perhaps even a relay or stepping switch type). A disadvantage of this system or any other that uses separate detectors is the great problem of balancing of the outputs of each detector.

(2) A shutter moving across the object simulating stepwise multiplexing. This would operate at much lower frequency than would the final system and therefore is not the most desirable way of building a breadboard for test stand operation. (Variations of this approach using rotating prisms in object space, etc., could conceptually operate at much higher speed.)

(3) A technique for moving the object in a stepwise fashion across a $5^{o} \times 0.25^{o}$ viewing angle. Conceptually this could be accomplished mechanically. A more promising approach would be to prepare a special motion picture film in which stepwise motion would be accomplished either by stopping the film as the relative position of the camera and object is changed or by suitably editing out the transitional phase of the step motion. The single aperture breadboard front end should then produce the same video signal when viewing a playback of this film that a multiplexed 20-step input system would produce viewing the original object.

(4) The use of a deflectable photomultiplier programmed to operate with 20 steps would combine the functions of the array and the multiplexer and eliminate first order problems associated with balancing. If a deflectable multiplier with a suitable aperture (one that subtends $5^{o} \times 0.25^{o}$) was not obtainable, a photomultiplier with a round aperture used in conjunction with an anamorphic lens to give the required intercepts was considered.

As a result of our study of the various potential techniques for simulating the detector array–multiplexer combination in the visible domain, it was concluded that the image dissector in the form of a deflectable photomultiplier was the most promising approach, since it gave the maximum of engineering information with a minimum of requirements for solving problems that are not inherently germane to the final engineering task required, namely, the design of an infrared yaw sensor. An ITT Model FW-130 photomultiplier with a rectangular aperture that has a nominally 20:1 aspect ratio was selected to be used in conjunction with a staircase generator that shifts the photomultiplier line of sight 20 discrete steps and then retrace the line of sight to the starting point. This arrangement simulates a multiplexed detector array composed of 20 $5^{\circ} \times 0.25^{\circ}$ staves. The staircase generator provides a 500-microsecond dwell time at each aperture position, 500 microseconds being the sampling time of each stave in the final system.

3.7 CORRELATOR DESIGN

The BAI correlator provides an error signal as a function of the phase difference between two given input waveforms, typically a video signal (V) and a reference signal (R).

Correlation is accomplished by delaying the V and R signals with individual delay components to obtain video delayed (V_D) and reference delayed (R_D) signals and then combining the four signals (V, R, V_D, R_D) in a prescribed manner.

The correlator output must not only reflect the amount of phase shift between R and V, but also the sense. If we arbitrarily assume that we desire a positive correlator output if R leads V, and a negative correlator output if R lags V, we obtain the following Boolean expressions for correlator action:

$$\text{R leads V} \equiv \emptyset_1 = (R + V_D)(\overline{RV_D})\overline{(R_D + V)(\overline{R_D V})} \quad (1)$$

$$\text{R lags V} \equiv \emptyset_2 = (R_D + V)(\overline{R_D V})\overline{(R + V_D)(\overline{RV_D})} \quad (2)$$

Physically, equations (1) and (2) state that if $\emptyset_1$ is a logic 1, the correlator output should be a positive voltage. If $\emptyset_2$ is a logic 1 the correlator output should be a negative voltage. $\emptyset_1$ and $\emptyset_2$ are mutually exclusive for a logic 1.

The correlation design previously used in BAI systems, typically on the Lunar Orbiter system, performed the logic functions by analog summation of quantized V and R signals. Units of current were injected into or removed from a nodal point. The inputs were the V, R, V_D, R_D

and the complements thereof: $\overline{V}$, $\overline{R}$, $\overline{V}_D$, $\overline{R}_D$. The residual voltage remaining at the node determined the correlator output sense.

In practice, this analog technique required considerable care in order to achieve successful circuit performance, since the nodal residual voltage was a function of the input signal amplitude, the summation resistor, the diode gate voltage drops, and the transistor V_{BE} variations. The input signals were both positive and negative with respect to ground. For proper summation, the plus and minus excursion had to be equal and matched to the other signal amplitudes. Loading the driver circuits had to be done symmetrically. Precision resistors were required for summation. Further, it is difficult, if not impossible, to guarantee diode tracking under all conduction conditions.

A redesign of the correlator using purely digital techniques has yielded a far superior circuit. (A breadboard unit was built and successfully tested. This unit is shown in Figure 3.32.) Integrated circuits perform the logic requirements of equations (1) and (2) above. Input signals are a logic 0 and a logic 1, obviating the analog summation problems. (In the circuit implementation used, the logic 0 can range $0^{\pm}0.9$v; logic 1 can range 1.2 to 5.5v.) The delay lines have been replaced with electronic delay circuits, facilitating adjustment, improving tracking, and reducing size, weight, and power requirements.

The integrated circuits with their inherently faster switching times than the previous circuitry have yielded great improvements in signal-to-noise ratio. With the previous correlator circuitry, signal race conditions would cause noise "whiskers" to appear in the output even though perfectly matching waveforms were applied as input signals. Eliminating these "whiskers" and precisely establishing the position of the leading and trailing edge of each pulse in the video and reference signal has resulted in an improvement in signal-to-noise ratio of 10 to 20 db. (See Section 3.3 for a discussion of the effect of this on system performance.)

3.8 DESIGN OF SYSTEM MEMORY

3.8.1 General Discussion

In examining the available approaches for an all solid-state memory, there are at least two generic types of design approaches that are available. The block diagrams shown as Figures 3.33 and 3.34 define these two approaches, a shift-register and a word-oriented memory, respectively. The shift-register memory is particularly appealing on first examination for two reasons. From the block diagram it would seem to be very simple and, as a result, very reliable, since there would seem to be so few components (but this is somewhat misleading as explained below).

Also, it is almost the direct time-quantized, solid-state analog of the magnetic drum memory with which BAI has had so much successful experience.

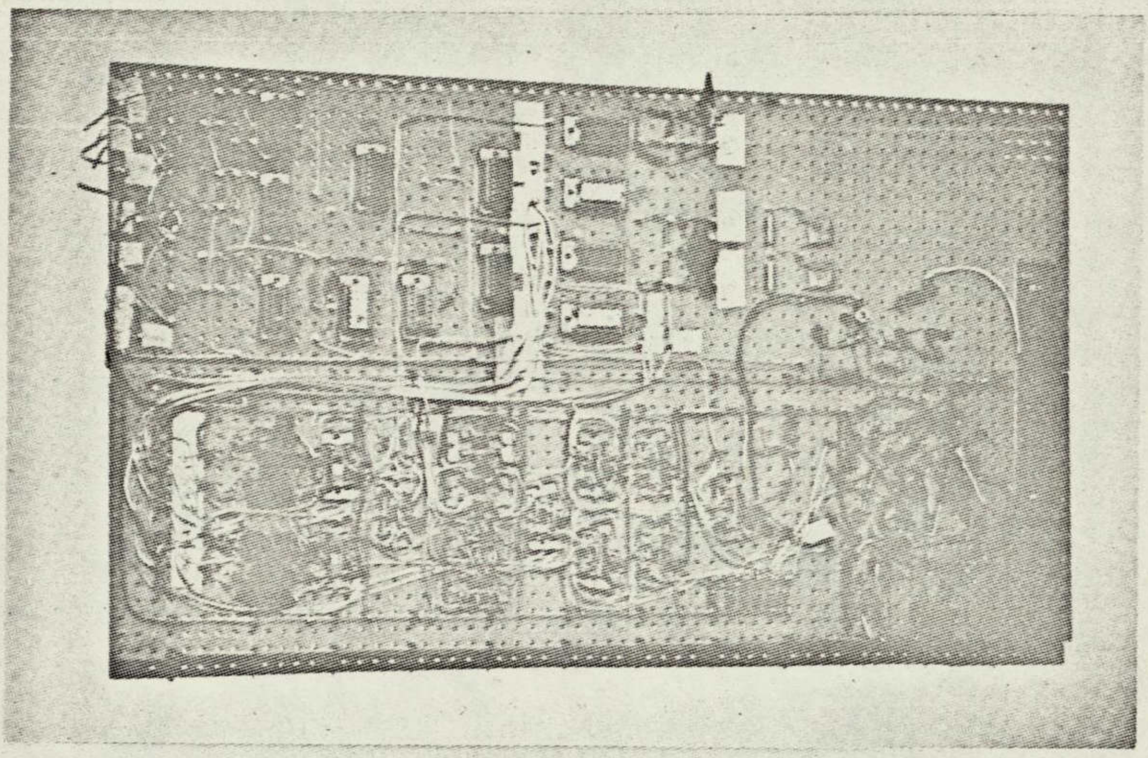

Figure 3.32 Breadboard Digital Correlator

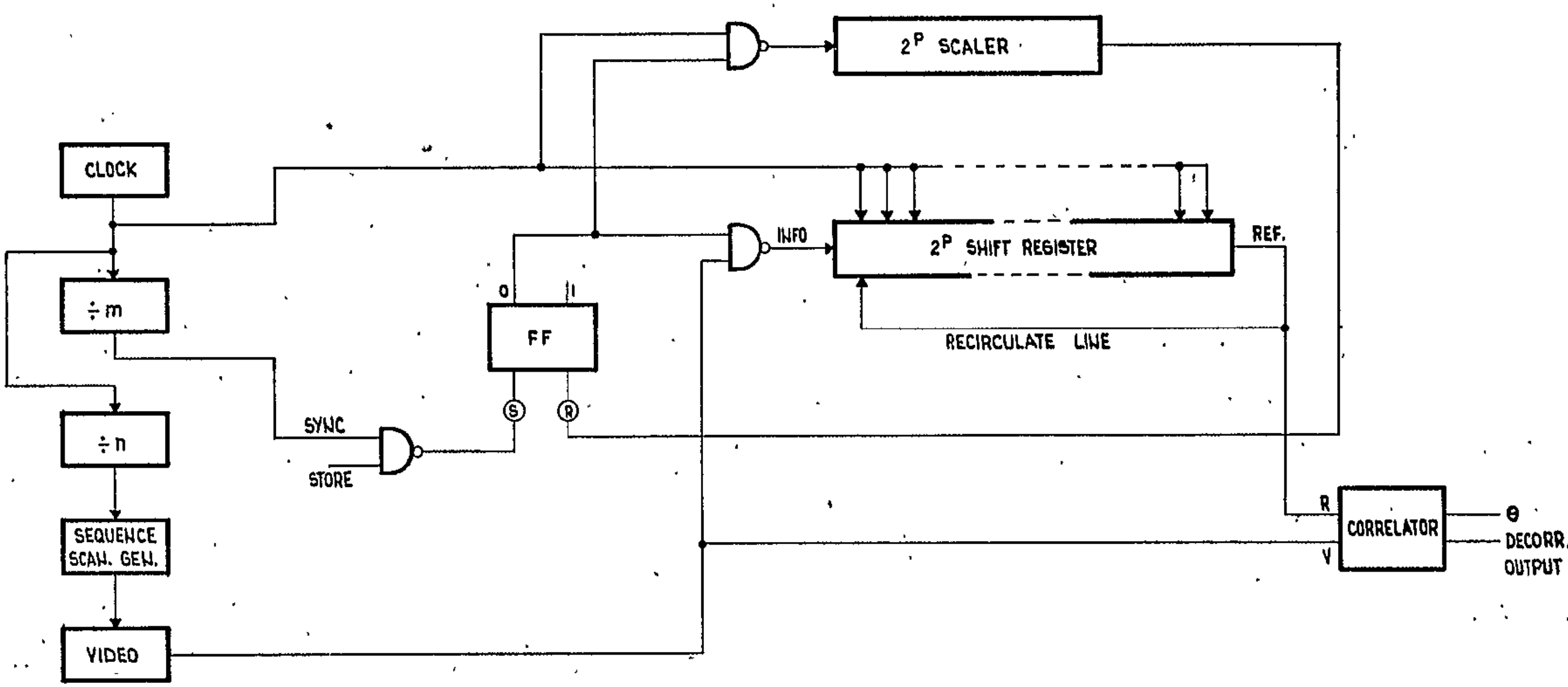

Figure 3.33 Solid-State, Shift-Register Memory

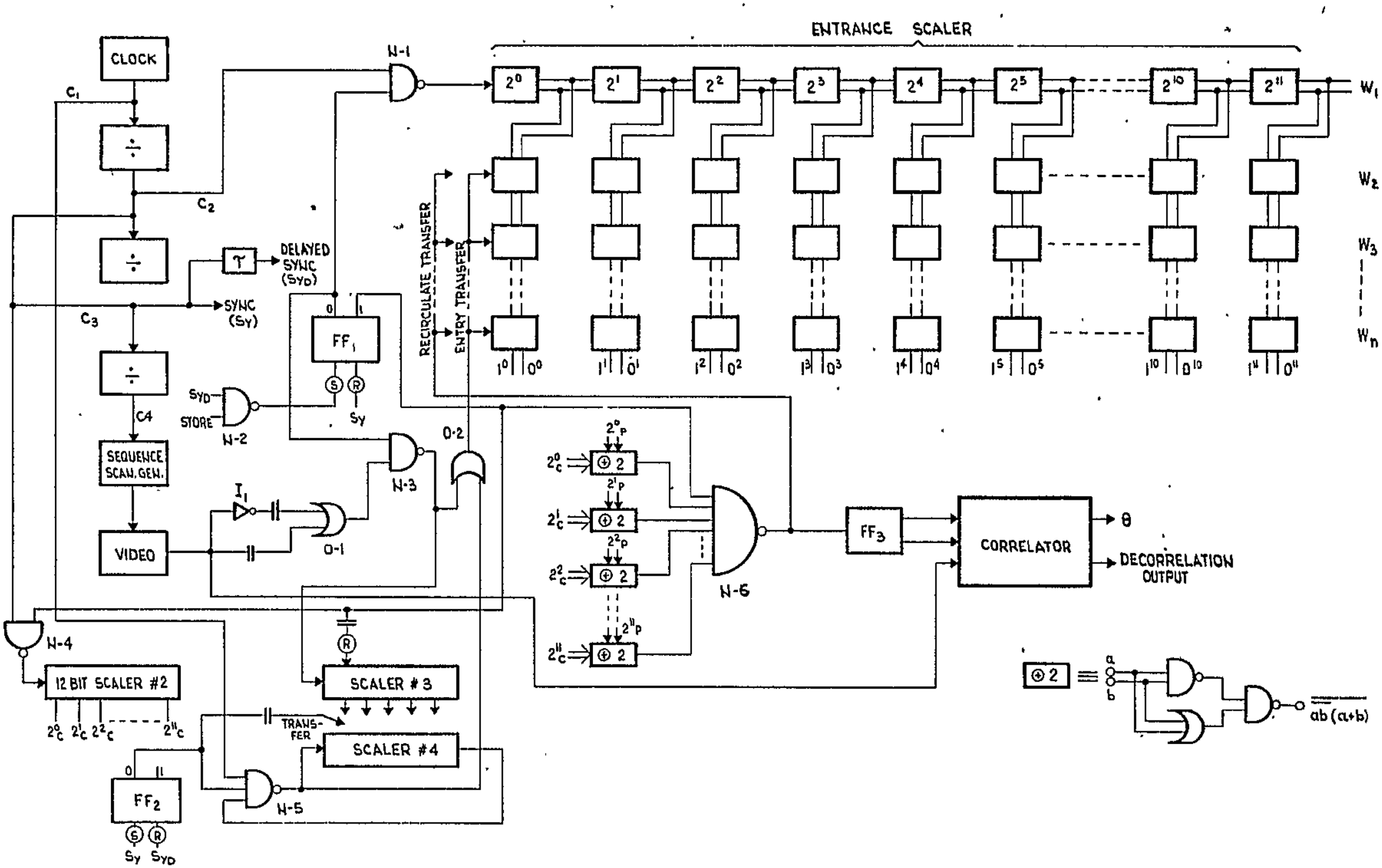

Figure 3.34 Solid-State, Word-Oriented Memory

Both the shift register and the magnetic drum are First In, First Out (FIFO) memories in which the programming and access are automatically controlled by the inherent FIFO nature of the basic design. The only external programming controls required are those necessary to choose between writing new information or continuing to circulate the old information.

When we examine the block diagram of the word-oriented memory, it appears to contain many more blocks and, therefore, many more components than the shift-register memory. In addition, without any question, the programming of the word-oriented solid-state memory is somewhat more complex because microprogramming is required for each of the steps of reading in information and then transferring it from one memory spot to another until it is ready to be read out. Peripheral scalers and counters are required to control all of this action.*

A proper choice between these two approaches should be based on their relative reliability and any logistical advantages that one might have over the other. In determining reliability, the primary factors that have to be considered are chip count and chip complexity. There is some literature extant that indicates that microcircuitry reliability is more directly a function of chip count than chip complexity; however, a preliminary reliability analysis** indicates that this may not be a valid assumption. Hence, at the present state of knowledge and experience with integrated circuits, both chip count and complexity must be considered and evaluated as meaningfully as possible. Possibly the most important difference between the two memories is that the shift register memory must use MOS devices whereas the word oriented memory uses bipolar devices. The MOS devices lend themselves to much higher packing densitites than the bipolar devices; however, the bipolar devices have the advantage of a much longer history of reliability studies, testing, and field experience.

In order to make this examination as meaningful as possible, the state of the art of today was considered to be a valid point from which to make the analysis. The argument for this is that the improvement in devices, both from the point of view of reliability and packing density, will probably be equal for the bipolar and MOS type chips. Therefore, for the most part, any data available today on chip complexity, packing density, and reliability probably indicates a trend that will continue over the next several years. Therefore, predictions based upon today's devices would be meaningful, since the fundamental ratios can be expected to remain relatively invariant.

---

*See Appendix 1 for a description of a word-oriented memory that "combines the best of both worlds" in that it eliminates most of this microprogramming.
**Reliability is discussed in greater detail in Section 3.8.2.

One of the very important points that is not immediately evident from the block diagram is that in the shift-register memory there has to be storage capacity for each of the "time slots" that we wish to maintain for a high resolution memory. Specifically, in the proposed system design of the yaw sensor, there will be 4,000 time slots required for the memory. Thus in the shift register approach there will necessarily be 4,000 separate shift-register storage elements.

Each storage element is at least comparable in complexity to a single flip-flop, and in actuality the configurations that are now available for these shift register memories use a storage element that is appreciably more complex than a single flip-flop. On the other hand, the word-oriented, solid-state memory uses the storage capacity of the memory much more efficiently. No storage capacity is maintained for "empty" information. One set of 11 memory elements is required for each of the edges that are expected to be found in a scanned area. Past experience has shown that we would not normally expect to have more than four edges of interest in a scanned area within the angular coverage and resolution of the proposed sensor. If we base our design of the word-oriented memory on accepting six edges (to be extremely conservative) we find that the total number of flip-flops and similar elements is less than 200.

With this established, the question remains to determine the chip count for the two types of approaches. For the shift register approach, it is possible today to get chips from several manufacturers carrying 100 shift register bits per chip, and there is at least one manufacturer providing 400 bits per single chip. However, past experience has shown that a component cannot be considered satisfactory for a high reliability program of this sort unless it is available from more than one source--at least three sources should be considered minimum. Therefore, to maintain a conservative approach, we will limit our analysis to components available today from several manufacturers. Thus, today we can pack 4000 bits for the proposed shift register into 40 100-bit chips, which are presently available from several sources.

The number of chips required for the word-oriented memory, again using components that are readily available from more than one manufacturer, will be order of magnitude of 50 individual chips at about four bipolar flip-flops per chip.

Finally we must consider the difference of the basic devices themselves. Only MOS devices provide the very high packing densities required for building the shift register memory in a 40 or 50 chip physical configuration. The word-oriented memory would use bipolar components. BAI has endeavored to determine relative reliability of MOS versus bipolar components for applications of this sort. We have referred to the standard MIL handbooks and discussed the matter with Rome Air Development Center and NASA Boston. As a result, we have found that the general consensus of opinion is that at present, and in the foreseeable future, the bipolar devices can be considered more reliable from several points of view. We are including herewith an analysis made by BAI's Director of Quality Assurance summarizing the results of our own in-house investigation (performed using the suggested reliability formulae) and also the results of the information that we have obtained from manufacturers and the two government agencies mentioned above.

As a result of this analysis, BAI's conclusion is that the bipolar type devices should be used in preference to the MOS devices, and the system be planned about a word-oriented memory. Since the available data seems to point this out so clearly, BAI proceeded to design, construct, and test a breadboard version of the word-oriented memory. (See Figure 3.35.)

3.8.2 Reliability Analysis*

3.8.2.1 Statement of Problem

To establish the relative reliability of integrated circuitry using MOS components versus reliability of "similar circuitry" using bipolar components. The specific purpose of the investigation is to determine proper solid-state memory design for the yaw sensor being built for NASA MSC, giving maximum weight to reliability consideration.

3.8.2.2 Data

Two solid-state memories were considered. Block diagrams and components count information are available for each. The two designs are as follows:

(1) A word-oriented memory that utilizes only bipolar type microcircuitry.

(2) A shift-register memory utilizing MOS type integrated circuits.

3.8.2.3 Reliability Considerations

(1) Reliability Notebook RADC-TR-67-108 (Volume II, Section XII, "Microelectronics") provides techniques for applying to microcircuits the reliability concepts ordinarily used for conventional component parts. The principles

*This section contains the reliability analysis that resulted in a decision to develop a word-oriented memory. The reliability of the total yaw sensor system is discussed in Section 4.5, below.

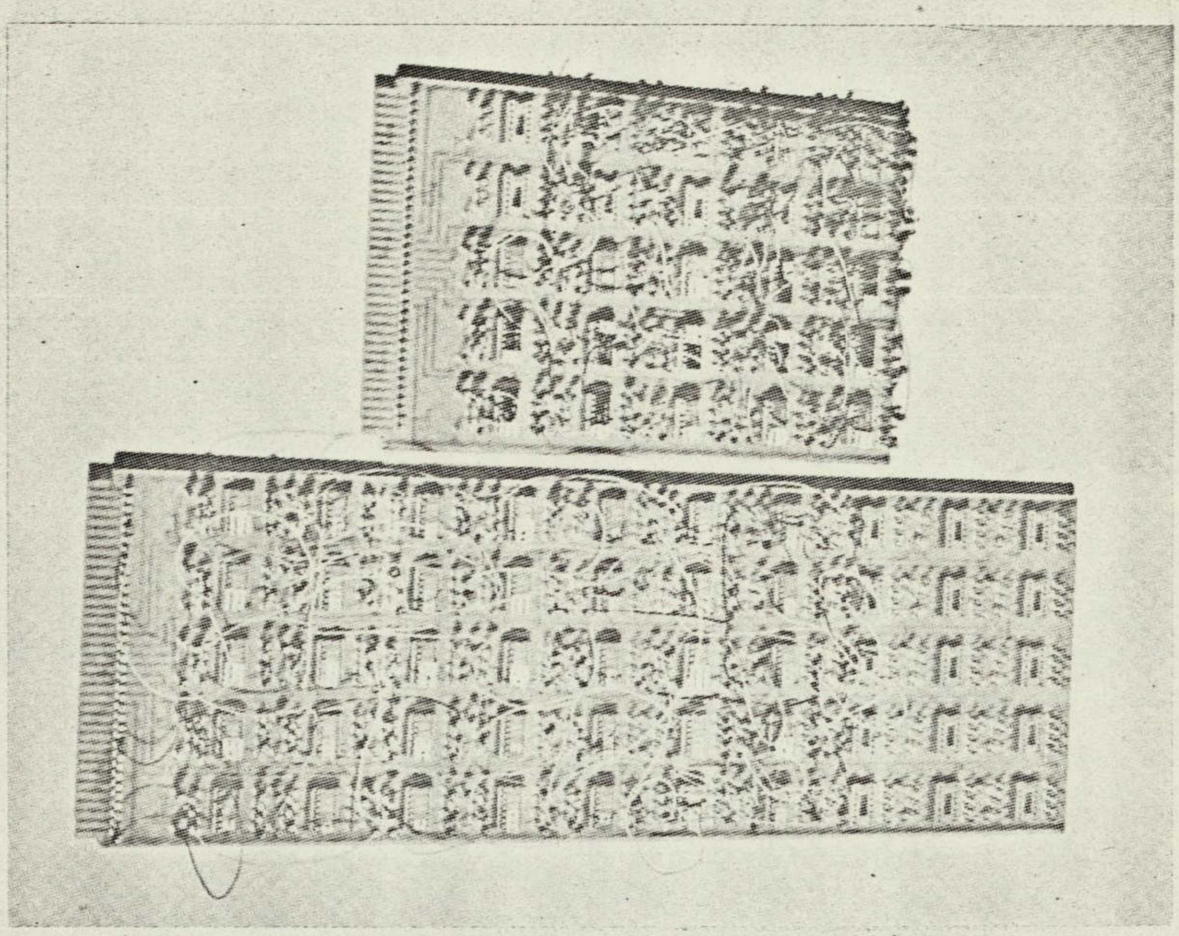

Figure 3.35. Breadboard Solid-State Word-Oriented Memory

and theory of microelectronic reliability presented therein leads to the conclusion that the failure rates that have been claimed by various microcircuit suppliers cannot be considered as valid measurement parameters. This is due to the variety of proprietary processes involved, the rapid rate at which the state-of-the-art is progressing, and the lack of standards for microcircuit types, functions, and performance.

The RADC Document suggests a Failure Rate Model for microcircuits which, as in the case of semiconductor devices, is basically the Arrhenious Model (or "Law of Thermal Degradation").

This Mathematical Model is expressed as:

$$\lambda_{\mu} = [\lambda_b \pi_c \pi_p \pi_E \pi_Q]$$

where λ_{μ} = microcircuit failure rate (in % per 1000 hrs.)

λ_b = basic failure rate (function of temperature)

π_c, π_p, π_E & π_Q = complexity, package, environmental, and quality factors

Use of the above mathematical model will not yield any quantitative results, since the complexity and package factors cited in this document do not take into account the differences in the manufacturing processes between bipolar and MOS devices.

The most important point raised in the RADC Reliability Handbook is that, contrary to suppliers' claims, the complexity of a given microcircuit has a bearing on its failure rate.

This was established when the modes of failure of various microcircuits were investigated.

(2) MIL-HDBK-217A "Reliability Stress and Failure Rate Data for Electronic Equipment" Section 7.14, has a brief discussion on microelectronic reliability. This section recognizes the limitations of the available failure rate data and recommends the use of 4 failures per 10^6 hours (or 0.4% per 1000 hours) as an acceptable failure rate for all microcircuits until more meaningful information becomes available. It is noteworthy that the MIL-HDBK-217A, which has precedence over RADC-67-108 as far as the DOD and NASA are concerned, gives no adjustment factors (use, complexity, etc.).

3.8.2.4 Conclusions

Since the "standard" techniques for determining microcircuit reliability have not been definitized by any of the cognizant government agencies, it is not possible to employ any universally acceptable analyses to show relative reliability of the two types of memories. Neither the MIL-HDBK-217A (the most acceptable and authoritative source for failure rate data) nor the methods of the RADC Reliability Notebook will yield any quantitative results for meaningful comparison.

Furthermore, it is not advisable to use "raw" failure rates supplied by various manufacturers before the military has had a chance to review, check, and accept such data.

The only statement that can be made with the information available at the present time is that the consensus among reliability and component engineers in the trade is that the bipolar devices should be considered preferable from both the reliability and maintainability standpoint when compared with the MOS devices because:

(1) They contain less elements per chip and are therefore less "complex" from manufacturing point of view.

(2) They have been in use longer and therefore they are closer to the "standardized" stage.

(3) There are more manufacturers of bipolar microcircuits, supplying a greater variety of types -- a very important logistics factor in case a certain device used in the design of yaw sensor memory exhibits any reliability problems.

3.8.3 Notes on the Operation of the Word-Oriented Memory*

The word-oriented memory shown in Figure 3.34** is composed of a clock, a count-down circuitry that derives the sync and delayed sync signals, a video

---

*BAI has recently developed an improved solid-state memory suitable for use in the yaw sensor. The new memory employs parallel read-in and read-out to simplify the circuitry, thereby enhancing reliability, reducing noise, and reducing power consumption. This new memory system is briefly described in Appendix 1.

**A breadboard word-oriented memory was built and successfully tested. This unit is shown in Figure 3.35.

signal that is sequentially sampled in synchronization with the clock; a memory composed of a twelve-bit entry scaler, and a twelve-by-N, static-storage register. Each bit of the static-storage register is composed of a JK flip-flop with parallel and serial input and output capabilities. In addition, there is peripheral control electronic circuitry and a correlator to compare the incoming video with the stored reference to derive yaw error signals. In this type of system the video word is not stored in the memory, per se, rather the positions of the video edges are stored in conjunction with the clock. We count the clock into the entrance scaler, and when a video edge appears, we take the stored binary number from the entrance scaler, W_1, and transfer it into the first storage register, W_2. Similarly, when subsequent video excursions occur, the binary number content of each register is shifted into the subsequent register until one scan period has elapsed. At the end of that time, we have stored in the memory the positions of the video edges with respect to clock time. This is accomplished in the following manner: the application of a store pulse is applied to N2. A delayed sync pulse is applied to the other leg of N2 to gate the store pulse in sync time to the SET input of flip-flop 1. Flip-flop 1 will gate clock C2 into the entrance scaler via N1, a 2-input NAND gate.

The reception of a video pulse of either polarity is ac coupled to O1, the output of which is applied to one leg of N3; the other leg of N3 is enabled by Flip-Flop 1, and therefore, video excursions pass through N3, through 02, and are applied to the entry transfer line of the storage matrix. When that pulse occurs, whatever number is stored in the entrance scaler is transferred into W2. The contents of W2 are transferred to W3, etc. At the next video excursion, a transfer pulse occurs again, and the process is continued until we complete one scan time. At the end of that time, the position of each video excursion in binary equivalent of clock time has been stored in the memory. Since we have no control over the number of video edges that may be present in any given target, we must then step the binary contents of the register to the final output register W_n. The output of N3 is also coupled to Scaler No. 3. It is the function of Scaler No. 3 to count the number of video excursions that have occurred in one scan cycle during the store mode in order that at the conclusion of store time, Flip-Flop 2 is put into the SET mode. The leading edge of the Flip-Flop 2 excursion transfers the contents of Scaler No. 3 into Scaler No. 4. The high frequency clock C1 is counted through N5 into Scaler No. 4 until the storage register has been filled to the Nth row. At that time, the output of Scaler No. 4 is fed back and disables N5. The contents of Scaler No. 3 have not been altered. In this manner, the positions of the video edges have been stepped along to the final output stages so that they can be compared with the incoming video on subsequent scan periods. The system is now ready to correlate the stored information with incoming video. This is accomplished in the following manner:

The Clock C2 is counted through N4 into twelve-bit Scaler No. 2. The output of this scaler is compared with the output lines of the Nth register in memory. Comparison is performed by an exclusive OR compliment. When all bits of the twelve-bit Scaler No. 2 correspond to all bits of the Nth register, we can then say that we have located the position of the first video edge. At that time, the output of N6 will go to a logic 1. This will accomplish two functions. First, it will toggle Flip-Flop 3. Secondly, it will generate a recirculate transfer pulse such that the contents of W_N will be transferred into W_2. The content of W_2 will be transferred into W_3, the contents of W_3 to W_4, etc. This constitutes the recirculation of the reference information. The output of Flip-Flop 3 is applied to the correlator and compared with the incoming video information. The NRZ output of the correlator will be an indication of the degree of mismatch between the stored reference and the video. If the output of the decorrelation circuit (considered here as part of the correlator) increases to some preset limit due to mismatch, a new store signal will be generated, which will then store the positions of the new video edges into memory as previously described. At the end of one scan time, the process of pushing the edge positions down to the readout row is repeated via Flip-Flop 2, Scalers 3 and 4. Note that Scaler 3 still retains the number of excursions that have transpired in any given scan until Flip-Flop 1 is set upon application of the store pulse. When the new store pulse is applied to N2, the ac excursion of Flip-Flop 1 will reset Scaler No. 3 so that it is in a position to accept the new number of bits in a video scan.

3.9 SYSTEM TESTING: PHILOSOPHY AND INSTRUMENTATION

3.9.1 Test Philosophy

The program of testing of the breadboard visible-light front end involved a careful step-by-step program of testing the front end first by itself, viewing both indealized and random targets under ideal conditions, and then testing the front end in combination with breadboard versions of the other major system components (primarily the memory and correlator), carefully introducing one at a time the several parameters that influence system performance.

A test program was developed and instrumentation built up to follow this step-by-step philosophy. Throughout this part of the effort, there was an implied (though never explicitly stated) goal of demonstrating system sensitivity at the specified $1/4^{\circ}$ threshold. Our preliminary calculations, based on the postulated noise of the front end and processing circuitry, had indicated that this would be the order of the performance to be expected from the system. Our measurements have shown that we were much too conservative. As measured, the system threshold sensitivity is about $\pm 1/8^{\circ}$. More importantly, this threshold was not determined by the noise of the simulated front end or the processing circuitry, but rather by test-bed memory noise (in the form of uncertainty of the reference video edges); this noise level would have been completely satisfactory for a $1/4^{\circ}$ system, but is sufficiently large to be the controlling factor limiting the measured system sensitivity to approximately $1/8^{\circ}$.

Because of this very happy but unexpected result of the testing, BAI felt that some of the test effort should be diverted to establish a better measure of "true" system threshold. This could be done with only the comparatively modest effort required to improve the noise characteristics of the test-bed rotating memory. Such an effort could be supported on the existing static test setup, since the sensitivity and resolution of the X-Y table has sufficient reserve to provide meaningful measurements down well below $1/8^{\circ}$. Dynamic operation can then be determined analytically from the static data, the required calculations being easily made and amply substantiated by past hardware experience. (Dynamic testing at this level of sensitivity cannot presently be accomplished since the dynamic test stand was designed with resolution capabilities predicated on a $1/4^{\circ}$-sensitivity system in mind.)

Thus, a four-stage program was established to determine system operation and threshold:

(1) Study of the performance of the deflectable photomultiplier-staircase generator combination when viewing an idealized target and a random target (aerial photograph).

(2) Determination of system performance with target displacement in the X (yaw) direction only.

(3) Determination of system performance with target displacement in the X (yaw) direction when there is accompanying displacement in the Y (forward) direction.

(4) Determination of dynamic system performance.

From the results of this program (and studies of overall system parameters, the infrared front end, and the roll effect problem), BAI was then in a position to establish a preliminary block diagram and layout, make preliminary size, weight, and power estimates, and establish parameters for the interface between the infrared front end and the balance of the system, preparatory to undertaking the design and fabrication of a flyable breadboard satellite yaw sensor.

3.9.2 Test Instrument Setup

The following instrument setups were employed:

(1) The first stage of testing (study of the performance of photomultiplier-staircase generator) used an instrument setup consisting of the photomultiplier (stepped by the staircase generator) viewing a target (back-lit by a light box) through a relay lens. The video output from the photomultiplier was monitored by an oscilloscope.

(2) The second and third stages of testing (static testing with only X displacements and with X displacements in the presence of Y displacement) used the test setup shown in Figure 3.36. An illuminator back-lit the target. An X-Y table was used to introduce precisely controlled X and Y target displacement. A variable band-pass filter allowed study of the effect of changes in video bandpass on system performance. (Further testing, using an improved rotating memory, with reduced noise, will provide more precise static sensitivity measurements under a variety of conditions, permitting calculation of dynamic performance. The results of this testing, as soon as available, will be the subject of a supplement to this report.)

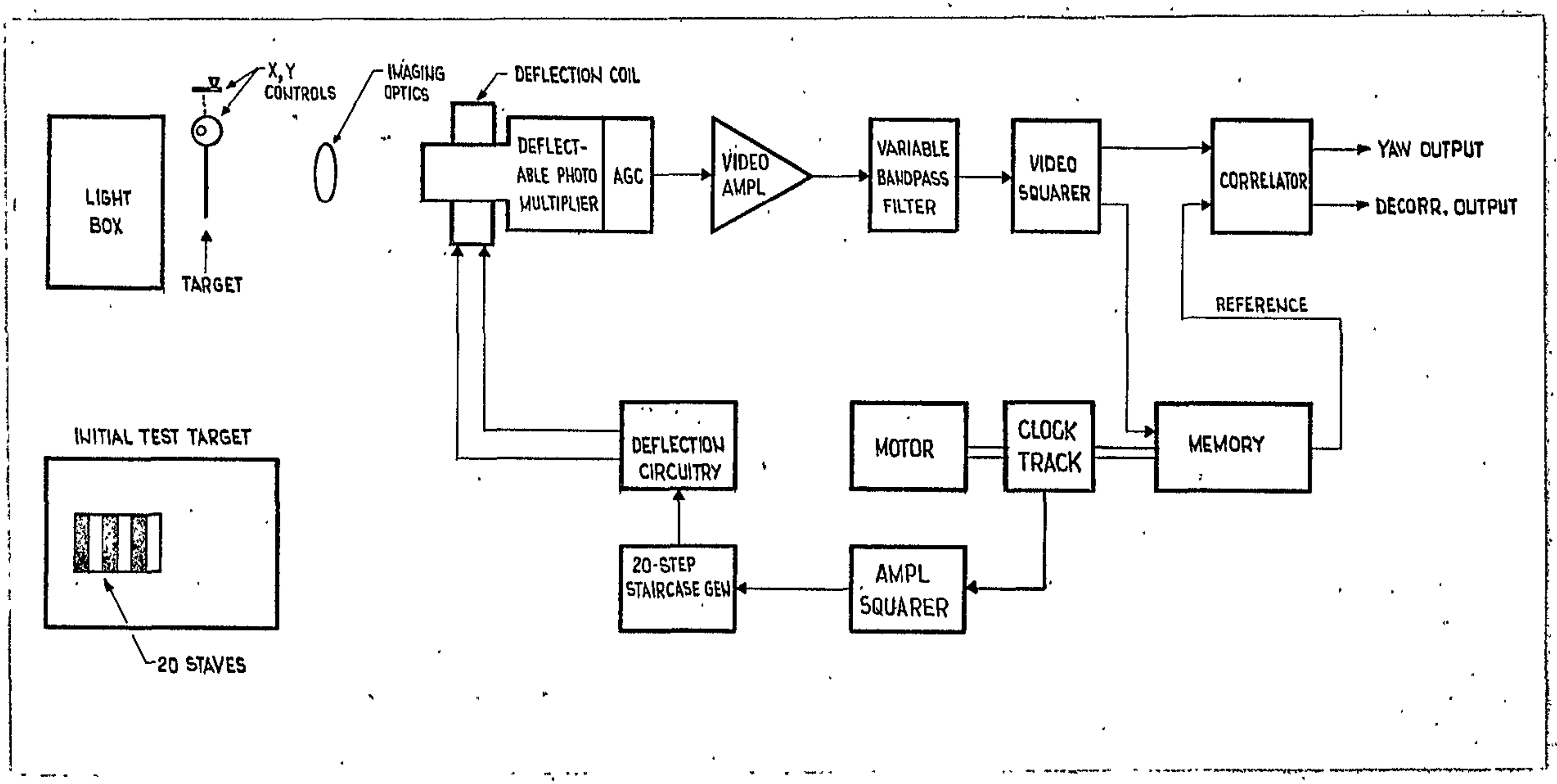

Figure 3.36. Static Test Setup, Block Diagram

3.9.3 Static Test Stand Design

The static test stand designed and built for this program (Figure 3.37) represents a significant refinement over previous units. The stability and resolution required to measure the performance of the visible-light breadboard was achieved, in part, by use of a well aged machine tool base and the use (for X and Y target travel) of precision cross-slides of the sort used in toolmakers' microscopes. (The cross-slide was used at maximum resolution; it does not bear any of the load.) A micrometer, spring-loaded to prevent backlash, is used to provide target rotation accurate to 6 minutes of arc. The use of machined step etalons in conjunction with standard off-the-shelf, inexpensive dial indicators provided 50-microinch direct reading of X and Y with several inches of permissible travel. Pin-located target holders permitted rapid, but highly repeatable, changing of test targets.

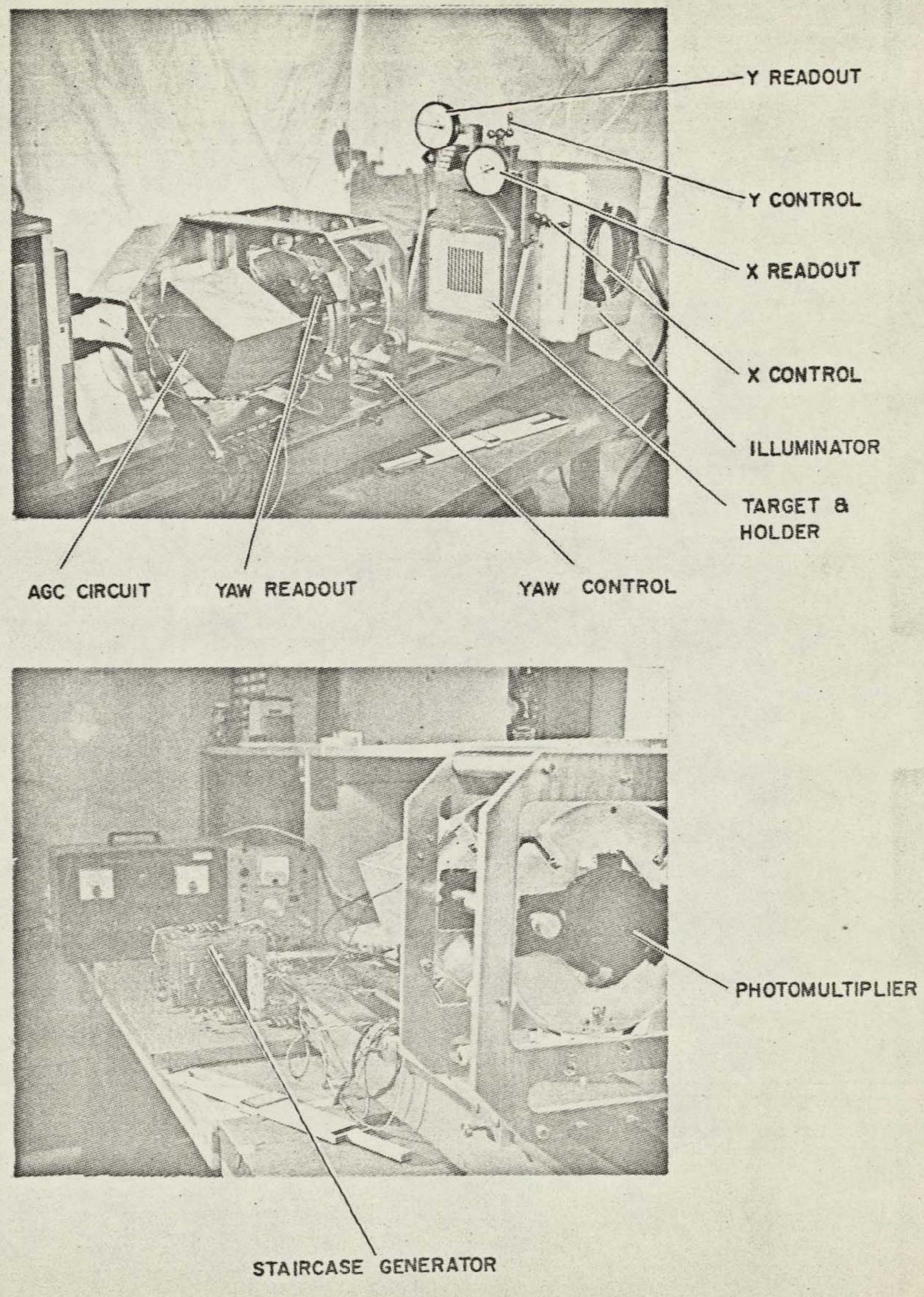

Figure 3.37. Visible-Light Breadboard Mounted in Static Test Stand

SECTION 4

SUMMARY OF RESULTS, PRELIMINARY DESIGN, AND CONCLUSIONS

4.1 BREADBOARD TESTING

4.1.1 Test Program

The following three-phase test program to determine the performance of the visible-light breadboard was established:

(1). Video Response of Photomultiplier

First the video response of the photomultiplier (stepped by the staircase generator) viewing an idealized target would be determined as a basis for comparison for later tests. Then, the standard photomultiplier-staircase generator response when viewing first an idealized and then a random target would be determined. The video output of the photomultiplier with AGC for various degrees of modulation over the dynamic range of light level would be determined.

(2) Static System Study With Only Yaw Deflection

Tests would be conducted to establish system threshold and gain for target displacement in the X (yaw) direction (error voltage output versus displacement). The effect of video bandwidth change would be determined. System sensitivity as a function of information content of the target would be determined.

(3) Static System Study with Yaw and Forward Displacement

Tests would be conducted to establish a family of curves of system threshold and gain for target displacement in the X direction in the presence of Y (forward) displacement for a number of different values of Y. The amount of forward displacement that can be introduced without degrading performance would be determined.

Tests would be run with both idealized and random targets.

A family of curves of system sensitivity would be obtained for a number of signal-to-noise ratios at the video input to the system.

Calculations would establish the dynamic performance of the system with a moving target.

4.1.2 Test Results

(1) Photomultiplier Tests

Figure 4.1 represents the video response obtained viewing a target that consisted of backlighting an opaque surface containing a hole in the field of view. This figure also indicates the output of the staircase generator.

This then showed that the proposed technique for simulating the 20-element array by means of a stepped aperture in a deflectable photomultiplier was feasible. The next step was to determine whether this simulated sensor could be made to operate over a large dynamic range. This was accomplished by substituting the standard BAI photomultiplier AGC (PMAGC) circuit for the resistor string at the photomultiplier dynode connections. (There was a possibility that the transients introduced by stepping the photomultiplier aperture would interact in an undesirable manner with the standard BAI PMAGC. However, the tests showed that this was not the case. Very little trimming was required to produce the required signal-to-noise ratio at the video output.)

The front end, with this configuration, was first checked with a high contrast random target, as shown in Figure 4.2b. Changing the contrast of the target by simultaneously reducing the backlighting and introducing front lighting to "wash out" the contrast did not measurable deteriorate the quality of the video signal.* Having demonstrated this operation, and further demonstrated that the video signal from sample aerial photographs was of comparable quality, it was decided that the bulk of the data should be taken with the artificial random target in order to introduce as few uncontrolled variables as possible. Where appropriate, rechecks could be made with selected aerial photographs to insure that the data obtained from the artificial random target was being properly extrapolated.

(2) System Tests

Tests were conducted to establish system sensitivity. The results of these tests are shown in Figures 4.3, 4.4, and 4.5. Figure 4.3 indicates

*These would be the expected results with the standard BAI PMAGC and a "standard" BAI scan on a deflectable photomultiplier. It was felt necessary to confirm that the same results would be obtained with a scan that departed from our standard as greatly as does the staircase.

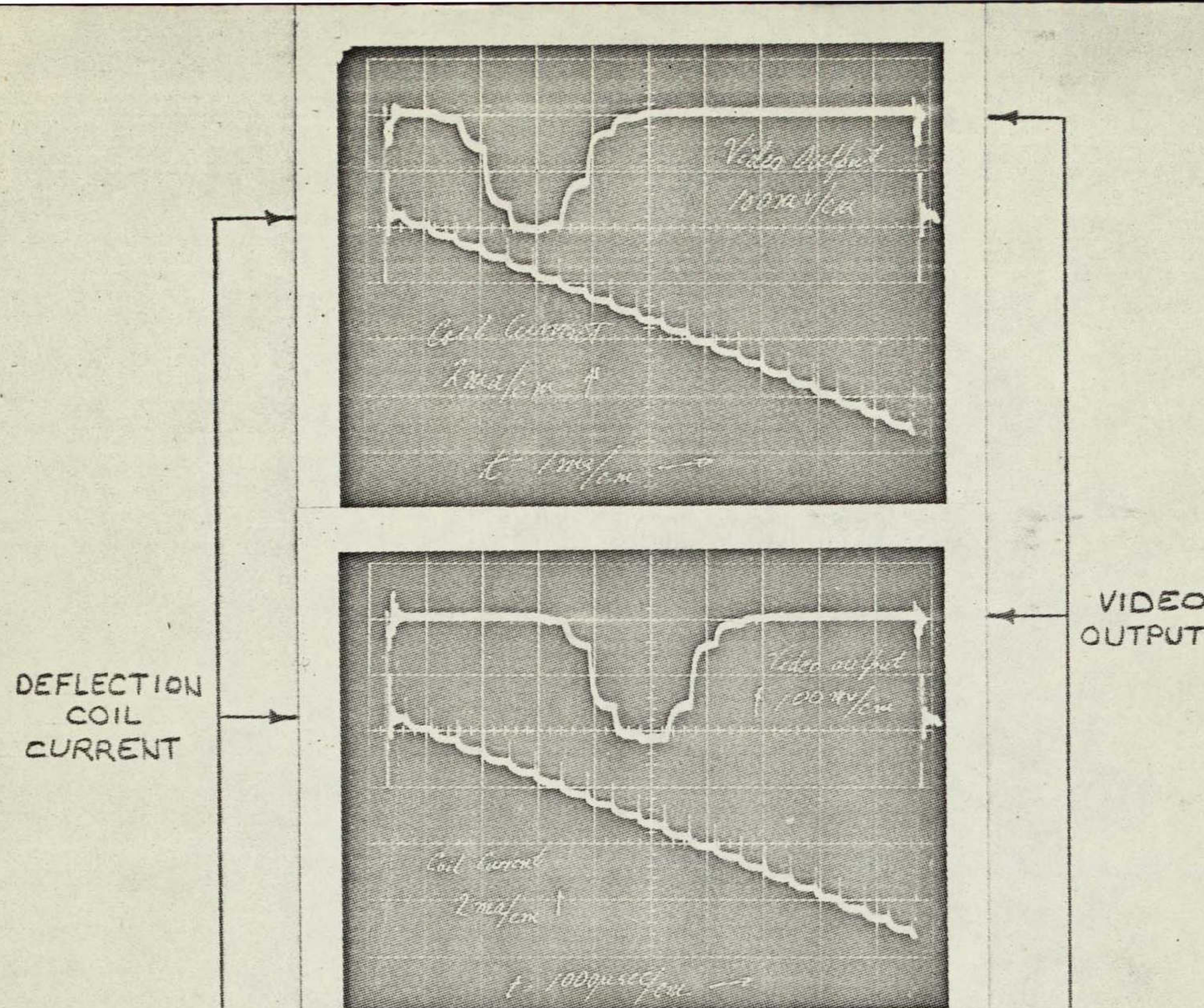

Figure 4.1. Video Output With Deflectable Photomultiplier Viewing a Hole in Various Positions (Upper Trace) and Staircase Generator Output (Lower Trace)

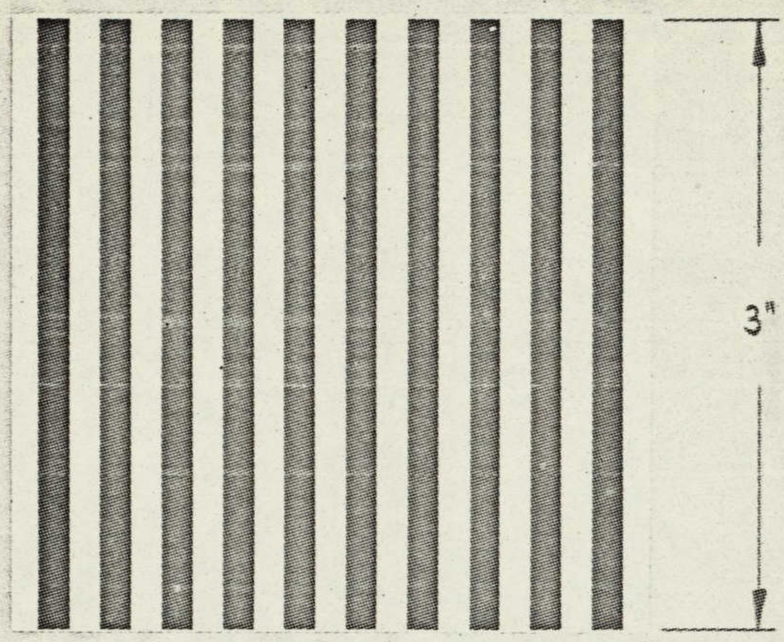

Figure 4.2a. Idealized (Bar) Target

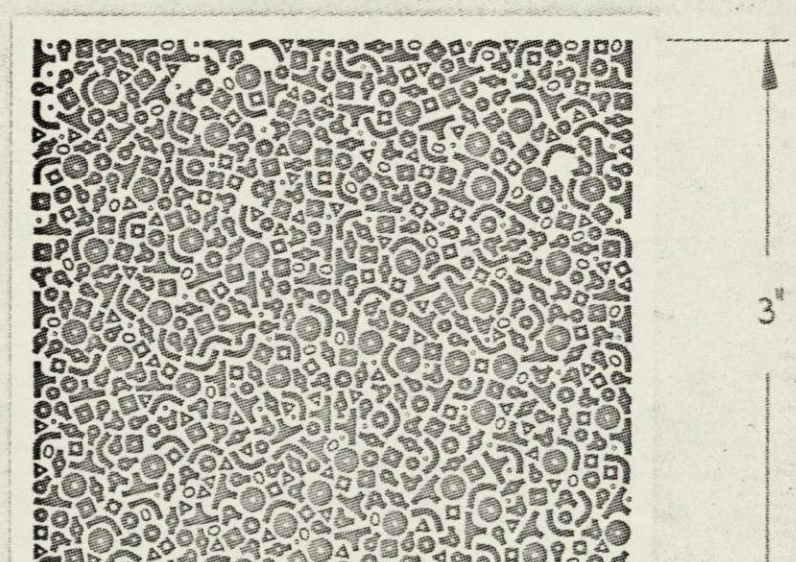

Figure 4.2b. Random Target

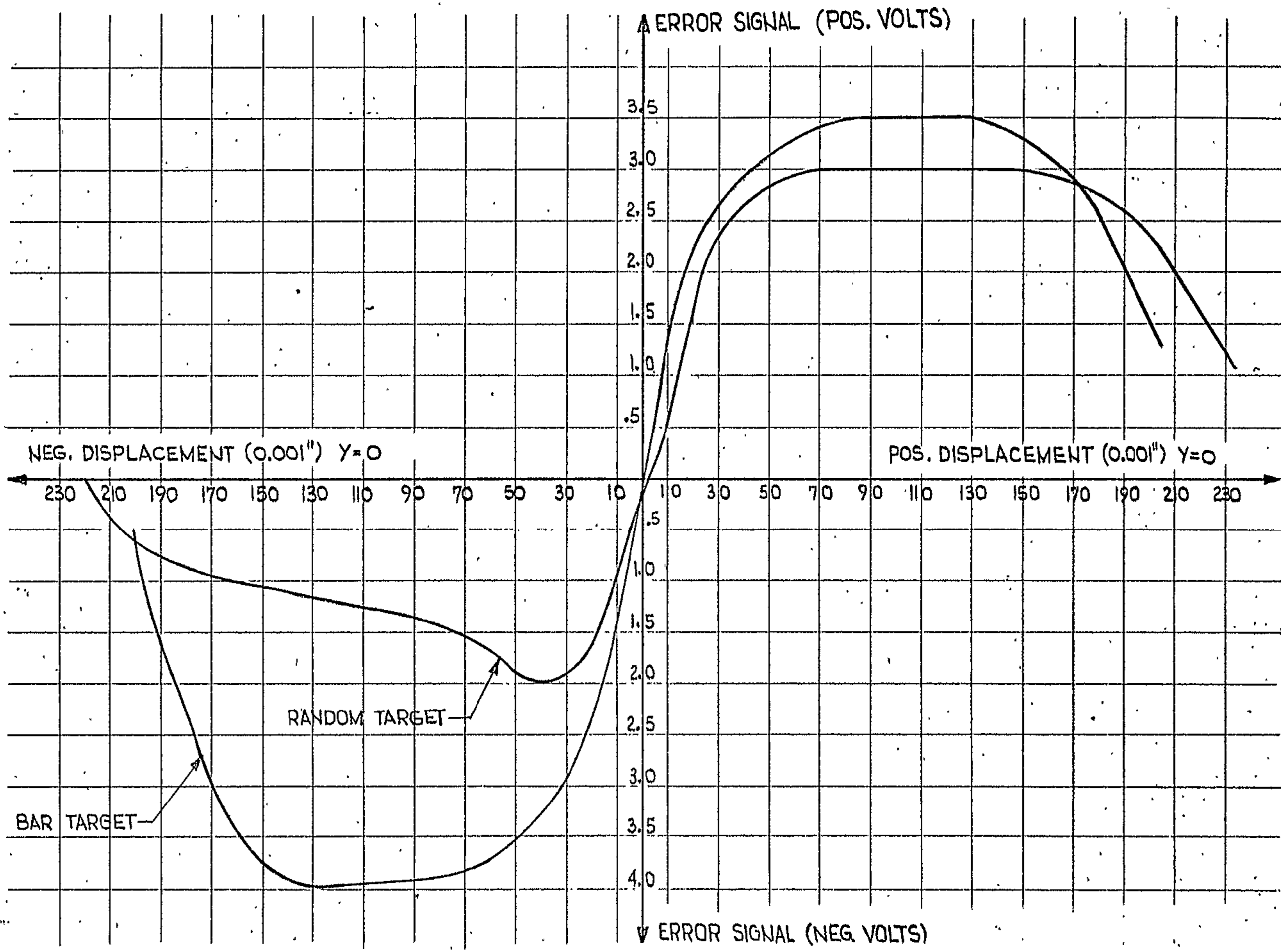

Figure 4.3. Error Signal Output vs. Horizontal (X) Displacement

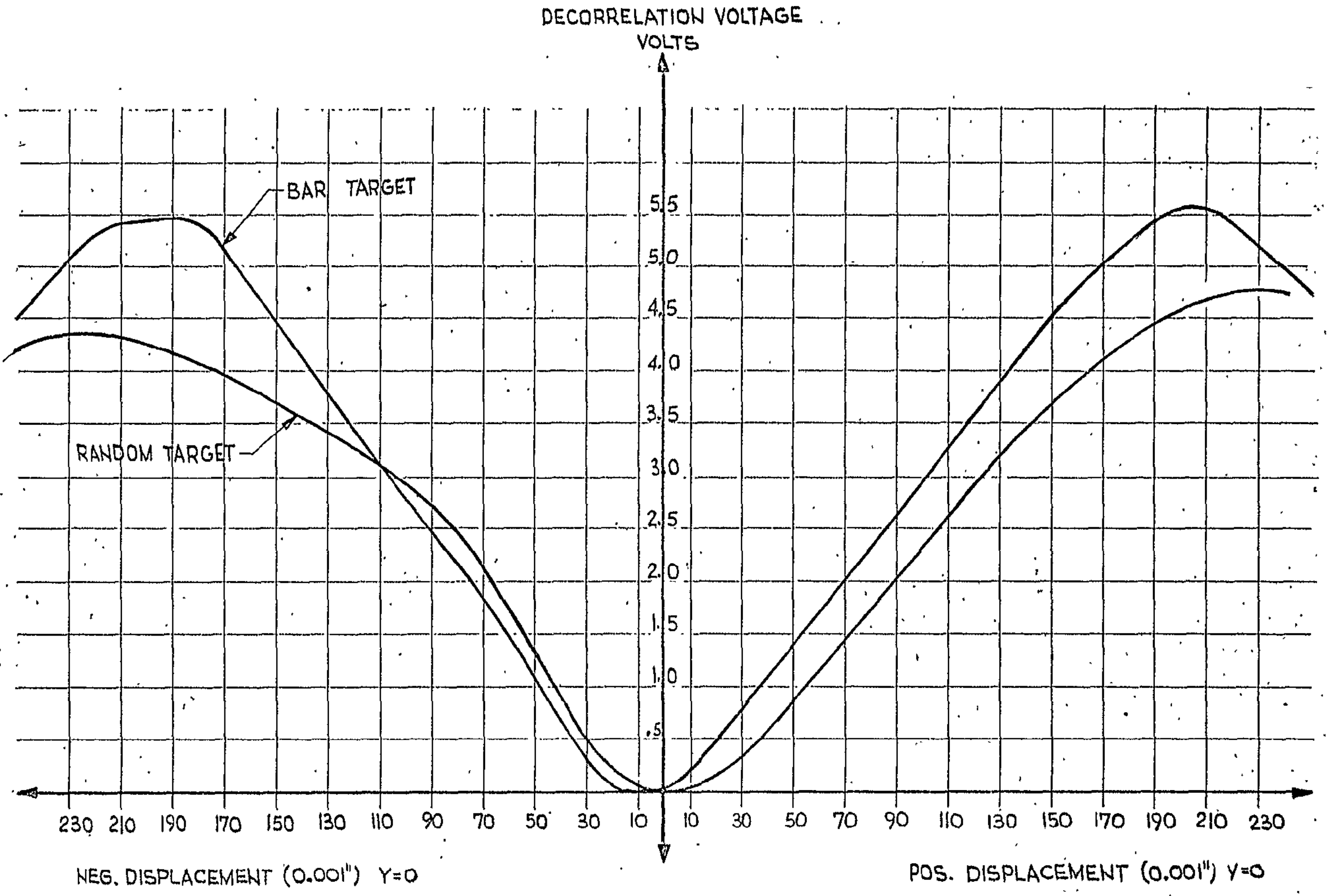

Figure 4.4. Decorrelation Output vs. Horizontal (X) Displacement

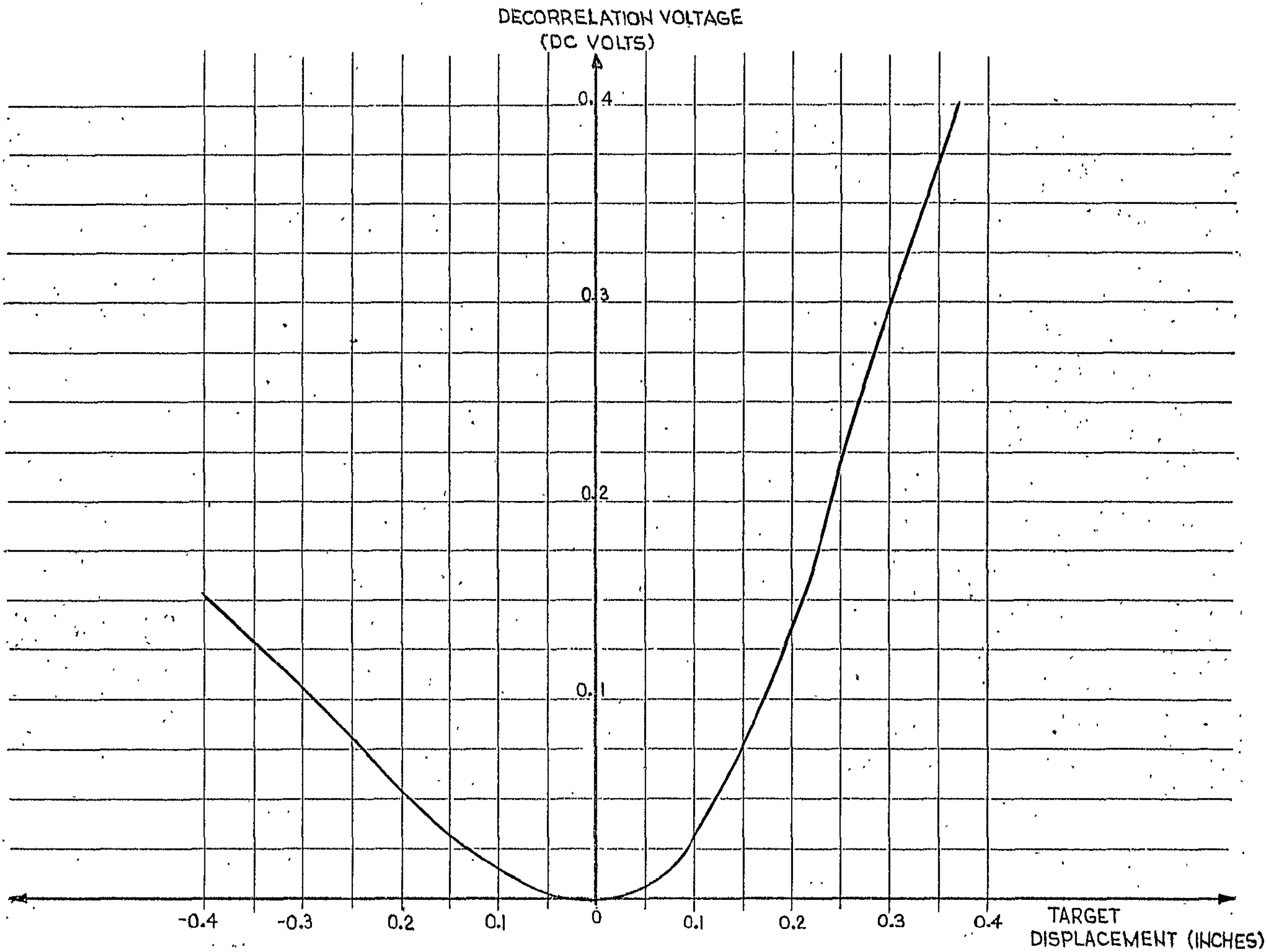

Figure 4.5. Decorrelation Output vs. Vertical (Y) Displacement

error output voltage as a function of horizontal (X) image displacement using both the bar and random targets. Figures 4.4 and 4.5 indicate the decorrelation voltage output as a function of displacement, horizontal displacement in the case of Figure 4.4 and vertical displacement in the case of Figure 4.5. Comparison of Figures 4.4 and 4.5 indicates the fact that, as predicated, the system is extremely insensitive to vertical displacement.*

Tests to establish proper video bandwidth were performed. At the time the tests were originally planned, it was thought that this would involve some significant engineering effort. However, the availability of a Krohn-Hite variable filter made the matter of setting suitable corner frequencies for the video band a matter of a few minutes' work. Such a procedure for establishing the proper corner frequencies would now be standard on future phases of the yaw sensor development program. (It should be noted that the bandwidth used in Phase I tests is not extensible to future systems, since the visible light breadboard in respect to noise, which is critical to setting video bandwidth, is not representative of the IR system. In particular, there are several noise sources that are peculiar to the breadboard unit: (1) noise associated with stepping the photomultiplier and photomultiplier retrace, cross-talk between the horizontal and vertical photomultiplier deflection coils, and inductive effects of the deflection coils; (2) noise introduced by the memory drum.)

---

*The decorrelation voltage indicates the degree of mismatch between the memorized reference image and the real-time image. When this mismatch becomes sufficiently large, a new reference must be memorized. Typically, a decorrelation voltage of approximately 1 volt indicates a mismatch large enough to require recording of a new reference. Figure 4.5 indicates that a 0.35-inch vertical image displacement results (corresponding to a displacement of 10% of the viewed area) results in a decorrelation output of only about 0.4 volts, a very high degree of insensitivity to vertical displacement indeed.

It should be noted that several planned tests have not as yet been conducted since noise (jitter) of the present drum memory obscures certain of the test results,* in particular, tests to establish:

(1) Sensitivity as a function of information content of the target

(2) The amount of forward displacement that could be introduced without degrading performance

(3) Sensitivity with different input video signal-to-noise ratios.

A new low-noise drum memory is under construction; upon completion these tests will be performed and reported in a supplement to this final report.

4.2 PRELIMINARY BLOCK DIAGRAM

A preliminary system block diagram appears as Figure 4.6. Operation of the system and its individual major blocks have already been discussed in Sections 2 and 3.

The Barnes-BAI electrical interface is discussed in Section 3.2.4 and consists of a logarithmically compressed "video" waveform (from Barnes to BAI) that is the result of sampling the output of the 20-element pyroelectric array at a 2-kc rate plus the clock signal developed by BAI and supplied to Barnes, suitably counted down to 2 kc at "standard" SUHL levels.

4.3 PRELIMINARY LAYOUT

A preliminary layout of the system (less the BAI electronics) if a thermistor detector is used is shown in Figure 3.21. Since the BAI electronics can be contained in approximately 100 cubic inches, a most modest increase in the height of the cylinder will be sufficient to provide the space required for the BAI electronics.

A preliminary layout for the system if a pyroelectric detector is used (also less the BAI electronics) is shown in Figure 3.24. Again, the 100 cubic inch requirement for the BAI electronics is easily satisfied.

4.4 PRELIMINARY SIZE, WEIGHT, AND POWER ESTIMATES

4.4.1 Size

As can be seen in Figure 3.24 (assuming use of the pyroelectric detector, the larger of the two types), the yaw sensor optical head itself can be housed within external dimensions of 9.25" x 11.75" x 10.5", which includes approximately 52 cubic inches that can be used for the BAI electronics. The BAI electronics require an estimated 100 cubic inches. Hence, only a modest increase in size is required to accomodate the BAI electronics.

*Problems associated with drum jitter are discussed in some detail in Section 3.3, above.

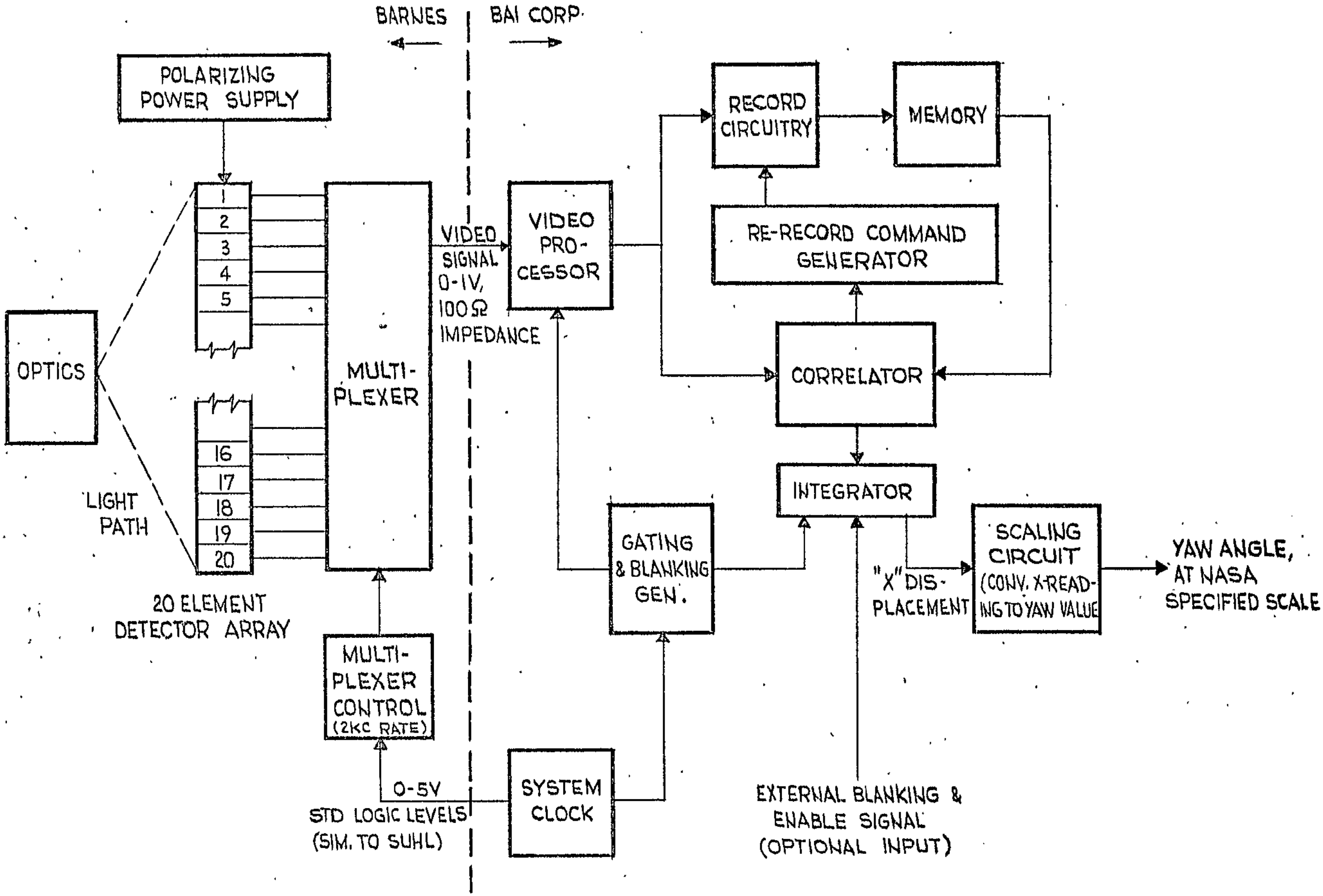

Figure 4.6. Preliminary System Block Diagram

4.4.2 Weight

A weight estimate breakdown for the yaw sensor, assuming use of a pyroelectric detector, is as follows:

Yaw Sensor Component	Weight (lbs.)
Housing (Aluminum)	5.1
Sheet Metal Covers (Aluminum)	1.3
Primary Mirror (Aluminum)	1.8
Folding Flat Mirror (Aluminum)	1.5
Detector Array Assembly	0.6
BAI Electronics	2.0
Total	12.3

4.4.3 Power Consumption

(1) Optical Head

If we assume that the yaw sensor will not be required to operate at a temperature higher than 45°C, the only power consumption in the optical head will be in the electronic processing. A conservative estimate of the expected power consumption of the Barnes-supplied circuitry is less than 1 watt. In the event that the yaw sensor must operate above the temperature of 45°C, a single stage thermoelectric cooler will be required for the detector array. The estimated additional power consumption for this cooler would be 1.0 watt, and this additional power consumption would only occur when the ambient temperature of the optical head exceeded 45°C.

Insofar as survival of the pyroelectric detector array is concerned, if the ambient termperature of the yaw sensor exceeds 45°C, the pyroelectric detector array will depole. However, tests have shown that once the ambient temperature of the pyroelectric detector array goes below 45°C, the biasing circuitry automatically repoles the array and full output is reached in approximately one hour.

(2) BAI Electronics

Estimated power consumption of the BAI electronics is 1 watt.

4.5 PRELIMINARY RELIABILITY ANALYSIS

4.5.1 Detector

Reliability data for the pyroelectric detectors is being generated by Barnes as part of an on-going program.. Ten pyroelectric detector elements have been on life test for over a year, and there have been no failures; in fact there has been no measurable degradation on any of the elements.

Barnes is at present under contract with NASA-Goddard (Contract NAS 5-11500) to space-qualify the pyroelectric detectors. The requisite environmental tests, etc., will be performed to obtain the necessary data for such qualification.

As a result of these efforts, plus other work that Barnes expects to be accomplishing on the pyroelectric detectors in the near future, reliability data and other associated information necessary for space use of the pyroelectric detectors will be available well before they will be needed for the final phases of the Yaw Sensor program.

4.5.2 Electronics

As part of its study for the system memory, BAI made an investigation to determine the best (or at least the most acceptable) way of determining the reliability of that part of a system built primarily from integrated circuits, using the best available techniques for design, assembly, and post-assembly protection* At the time of this study, a great deal uncertainty existed concerning the proper method for calculating the required data.

Since that time, significant effort has been expended by the government, in particular through the program under Joseph B. Brauer, Chief of the Solid State Application Section, Rome Air Development Center. As recently as June 1969, the Air Force asked industry's view of a plan to enforce an all-service high-reliability standard for testing microcircuits.

A draft of a specification giving screening and qualification test procedures for use in procuring monolithic and hybrid microcircuits was sent to thousands of industry vendors and users.

The specification MIL-M-38510 "General Specification for Microcircuit Quality and Reliability Assurance," applies the test methods and procedures of the microelectronics reliability standard MIL-STD-883.

*See Section 3.8 and in particular Section 3.8.2.

An accompanying questionnaire asking comments from vendors and users is due back at the Reliability Branch, Rome Air Development Center, by August 10, 1969. Two new methods T5004 (screening procedures) and T5005 (lot qualification inspection) were given in Notice I, dated 20 May 1968, of MIL-STD-883. When the comments are returned, RADC will seek full coordination (NASA, Army, Navy, and Air Force) of MIL-M-38510.

Since no standardized techniques have yet been established, the comments on reliability made in our memory study and repeated in Section 3.8.2 are still valid.

It is worth stating, though, in passing that now that a basic design and instrumentation approach for the yaw sensor has been determined, with most of the pertinent component type and parameters defined, it is possible to make a "best guess" estimate of the probable Mean Time Between Failures. This "best guess" is an extrapolation from the data and calculations that were used to determine the MTBF of the Lunar Orbiter V/H system, where the major contributors to "unreliability" were the motors, large capacitors, and filters. Eliminating the effect of these and making the very simple assumption that the remaining failure rate is a function only of number of external connections to active devices, our approximate extrapolations indicate a MTBF of something in excess of 10,000 hours.

BAI appreciates of course that such a best guess based on estimated extrapolations will have to be fully confirmed by acceptable procedures before a space hardware design can be undertaken. Judging by the rate at which data is being accumulated under the RADC effort, it is our belief that a preliminary reliability calculation procedure will be released within the next nine to twelve months, and a final version of this firmed up within eighteen months. This will allow preliminary calculations of reliability to be made during the next phase of this program in what will then be the approved manner.

4.6 PRELIMINARY IR SENSITIVITY CALCULATIONS

The Noise Equivalent Power Density (NEPD) of the yaw sensor is given by:

$$\mathrm{NEPD} = \frac{\sqrt{A_d \, \Delta f}}{A_o \eta \, D^*}$$

where:

A_d	=	Area of pyroelectric detector element
	=	0.066 cm x 1.4 cm = 0.0092 cm^2
Δf	=	Noise bandwidth of the system = 16 cps
A_o	=	Aperture area = 1.6 cm x 19.4 cm = 31 cm^2
η	=	Optical efficiency (Average of 5 gold-plated mirror reflections) = $(0.98)^5 = 0.90$
D*	=	Measured detectivity of pyroelectric detector element below 16 cps = 4.5×10^8 cm-$cps^{1/2}$-$watt^{-1}$

$$NEPD = \frac{\sqrt{16 \times 0.0092}}{31 \times 0.9 \times 4.5 \times 10^8}$$

$$NEPD = 3 \times 10^{-11} \text{watt/cm}^2$$

The irradiance (ΔH) produced by a 1^oC temperature difference in a 100^oK blackbody subtending $0.25^o \times 1^o$ (or 1/5 of the elemental field of view of the yaw sensor), when passed through the silicon field lens, which will have a spectral transmission shown in Figure 4.7 is given by the integral Planck blackbody radiation equation multiplied by the silicon field lens spectral transmission $[\tau(\lambda)]$, or:

$$\Delta H = \frac{\Omega}{\pi} \int_0^\infty C_1 \lambda^{-5} \left[(e^{C_2/\lambda T_1} - 1)^{-1} - (e^{C_2/\lambda (T_1 - 1^o)} - 1)^{-1} \right] \tau(\lambda) \, d\lambda$$

where:

T_1	=	100^oK
Ω	=	elemental target solid angle
	=	$1^o \times 0.25^o = 7.6 \times 10^{-5}$ ster
$\therefore \Delta H$	=	2.72×10^{-10} W/cm^2

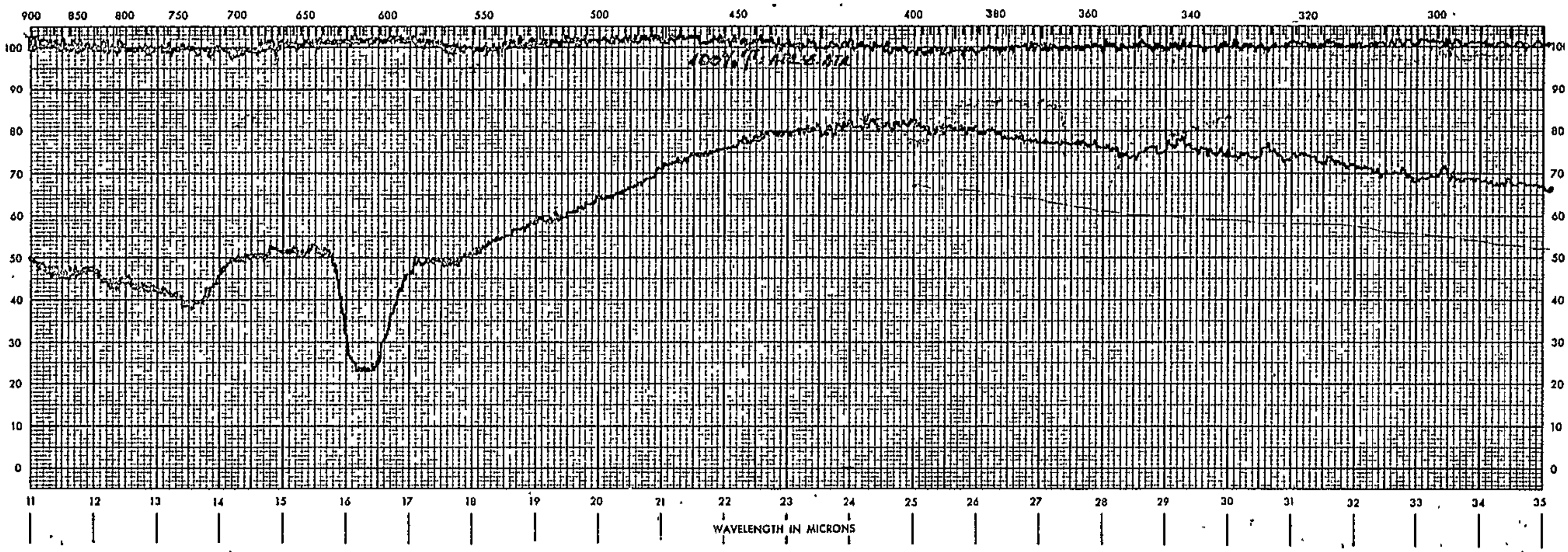

Figure 4.7. SPECTRAL TRANSMISSION OF SILICON FIELD LENS FOR INFRARED YAW SENSOR

Therefore the calculated Noise Equivalent Temperature Difference (NEΔ T) for the yaw sensor using the pyroelectric detector array is:

$$NE\Delta T = \frac{NEPD}{NEH} = \frac{3 \times 10^{-11}}{2.72 \times 10^{-10}} = 0.11^{\circ}C \text{ RMS}$$

This NEΔ T is a factor of 9:1 better than that which was calculated in the Yaw Sensor proposal.

4.7 WEIGHT AND SIZE VERSUS IR SENSITIVITY TRADE-OFF

The design of the yaw sensor discussed herein is based on using an existing pyroelectric detector array that has elemental dimensions of 0.026" x 0.056". This detector array results in an entrance aperture dimension of 0.63" x 7.5". As is shown in Section 4.6, this provides an adequate sensitivity for the operation of the yaw sensor. Increased sensitivity can be obtained by increasing the 0.027" dimension of the detector, which in turn will result in a directly proportional increase in the 0.63" aperture dimension. Since the instrument NEΔT varies as $\sqrt{A_d}/A_o$ (see Section 4.6), an increase in detector area by a factor of 4 will decrease the NEΔT by a factor of 2 without significantly affecting the size, weight, or power of the yaw sensor.

Alternatively, the overall size and weight of the yaw sensor can be reduced without sacrificing sensitivity by increasing the 0.027" dimension of each detector element, while at the same time proportionately decreasing the 7.5" dimension of the entrance aperture. These modifications would, of course, involve additional design and development for a new pyroelectric detector array.

4.8 CONCLUSIONS

This program represents Phase 1 of a program leading to the development of an infrared yaw sensor capable of operating in lunar and earth orbit, day and night, wherein Phase 1 is a feasibility study and Phase 2 involves the design and construction of a flyable breadboard system.

As suggested in Section 1, the present feasibility study sought to answer four questions relating to the adequacy of thermal gradients in the real world and the efficacy of the proposed design. An evaluation and analysis of best available information indicates the adequacy of thermal gradients even under worst case conditions (over the earth's oceans and just before lunar dawn). The effect of roll rate has been analyzed and shown to be easily overcome. The IR sensitivity (NE Δ T) has been calculated to be 9 times better than that calculated in the original proposal for Phase 1. The yaw angular sensitivity of the system has been demonstrated, on the basis of testing of a breadboard operating in the visible domain, to be at least two times better than that calculated in the proposal without taking advantage of improvement in NE Δ T.

Thus, on the basis of the results of the Phase 1 feasibility study, there does not appear to be any technical reason not to proceed to Phase 2, the design and construction of a flyable breadboard unit.

APPENDIX 1

IMPROVED SOLID-STATE MEMORY FOR BAI SCANNER-CORRELATOR

INTRODUCTION

As part of BAI's continuing effort to improve the performance of its correlator systems, BAI has recently developed an improved solid-state memory that has many advantages over the memory system designed for MSC under the Phase I study for the Yaw sensor. This new memory system uses a set of individual scalers, whose input is disabled at the appropriate time, to store the digital information representing the time slot number of each video transition. This allows parallel entry and readout, which proves to be a very great advantage.

The first memory system being built with the parallel in-out provision is capable of storing information to define a video signal with up to 30 transitions, each transition being determined with a resolution of about one part in 2^{15}. An addition redundant bit is stored to indicate the sense of the transition. Thus the memory is organized into 30 words, each containing 16 bits. This memory is briefly described below; it represents the configuration BAI would recommend for all future solid-state memories.

The solid-state storage techniques previously developed by BAI used a method whereby the clock counted into a single scaler. Upon receipt of a video excursion, the contents of the scaler was parallel dumped into a second register. Additional video excursions dumped the contents of each register into a succeeding register until all excursions were time-slot located. If we assume provision for thirty edges*, we would then have a storage system of 16 bits x 30 edges = 480 flip-flops. However, if an incoming video signature contains less than 30 edges, the final registers do not receive information. In order to read out the stored information, we must know which register contains the first edge, or we must "jam" the contents of all registers to a final output register such that the first edge is contained in this register. This jam function must be performed in a short period of time prior to sync to avoid possible dead time problems. Each edge, after use, must then be recirculated back to a previous storage register in order to maintain the continuous generation process required for the reference signal.

In either case, the logic required to perform the reference reconstruction has been considerably simplified by the new technique of parallel entry. As a result, system reliability has been greatly increased; there has been an elimination of possible "race" conditions; requirements on noise threshholds and timing sensitivity for each flip-flop and its associated gates are reduced; storage is static during all readouts, completely eliminating the possibility of transfer

*This represents the configuration now being built for photogrammetric applications errors. Noise generates only transient errors, which do not continue in memory as they would with the previous design.

Further, with the use of parallel entry storage:

Lower speed elements can be used, reducing system power requirements and consequently increasing reliability.

More densely packed IC's are available at these speeds and power levels, reducing external connections required and chip count.

As a final advantage, system checkout and maintenance is greatly simplified, since the operation of a static storage register is much easier to test and evaluate with simple oscilloscope tests than is a dynamic register, where testing usually requires artificially generated "worse case" signals with constant recirculation and monitoring of possible noise growth under limit conditions.

OPERATION OF THE PARALLEL-ENTRY SOLID-STATE MEMORY

A block diagram of the system is shown in Figure 1. The Interface Unit (IU) accepts information from the scaler memory. This information is in 16-bit-binary form, representing the time slot of a video transition with respect to an arbitrary synchronization time, t_o. The time slots are determined by a high frequency oscillator generating a clock train for system timing. The scaler memory contains 30 binary numbers, each number containing 16 binary bits. Each 16-bit number represents a video transition; therefore, in its present state the system can accept up to 30 video edges. The 16^{th} bit is redundant and represents the transition sign. At t_o, the memory scaler output representing the first video edge is presented to the IU. A 15-bit synchronous scaler counts the high frequency clock C_1. When the binary number in the counting scaler corresponds to the binary number stored in column 1 storage scaler, the comparator generates a recognition signal. This signal drives the reference word generator to reconstruct the first video transition in its proper time slot. A second clock, C_2, symmetrically interstitial with C_1, is used in conjunction with the comparator pulse to cause the Edge Select Circuit for the memory to choose the memory output defining the time slot for the second video transition. When the counting scaler output corresponds to this information, a second comparator pulse is generated, repeating the above process, thereby reconstructing (in serial output form) the reference word stored in digital memory.

The method used to store these video edge locations in the scalers is as follows. The application of a Store Command causes the generation of a record gate (G).

This gate is synchronized to the system by the sync output of the 15-bit main scaler in the mode logic circuit. A signature store gate (SSG) is generated which allows the video to enter the video edge gate generator (VEGG). The VEGG output consists of 30 enable gates (Γ_{1-30}) which allow C_1 to be counted by all 30 scalers in the storage circuit. The first incoming video transition disables Γ_1, thereby removing the clock from scaler 1. The first scaler therefore contains the binary number time slot representation of video edge 1. At the second video transition, Γ_2 is disabled, thereby causing scaler 2 to stop its count at the binary representation of video edge 2. It is obvious how additional video edge locations are stored in the scaler circuitry. At the conclusion of one scan period, a digital representation of a signature has been stored and a regenerated signature from this information contained in the scaler is indistinguishable from the video signal that was originally encoded, with the exception of the almost negligible effects of quantizing errors, which can be held to appreciably less than one part in 10^5. This information will remain in storage until power is removed from the circuit or a re-record command is generated.

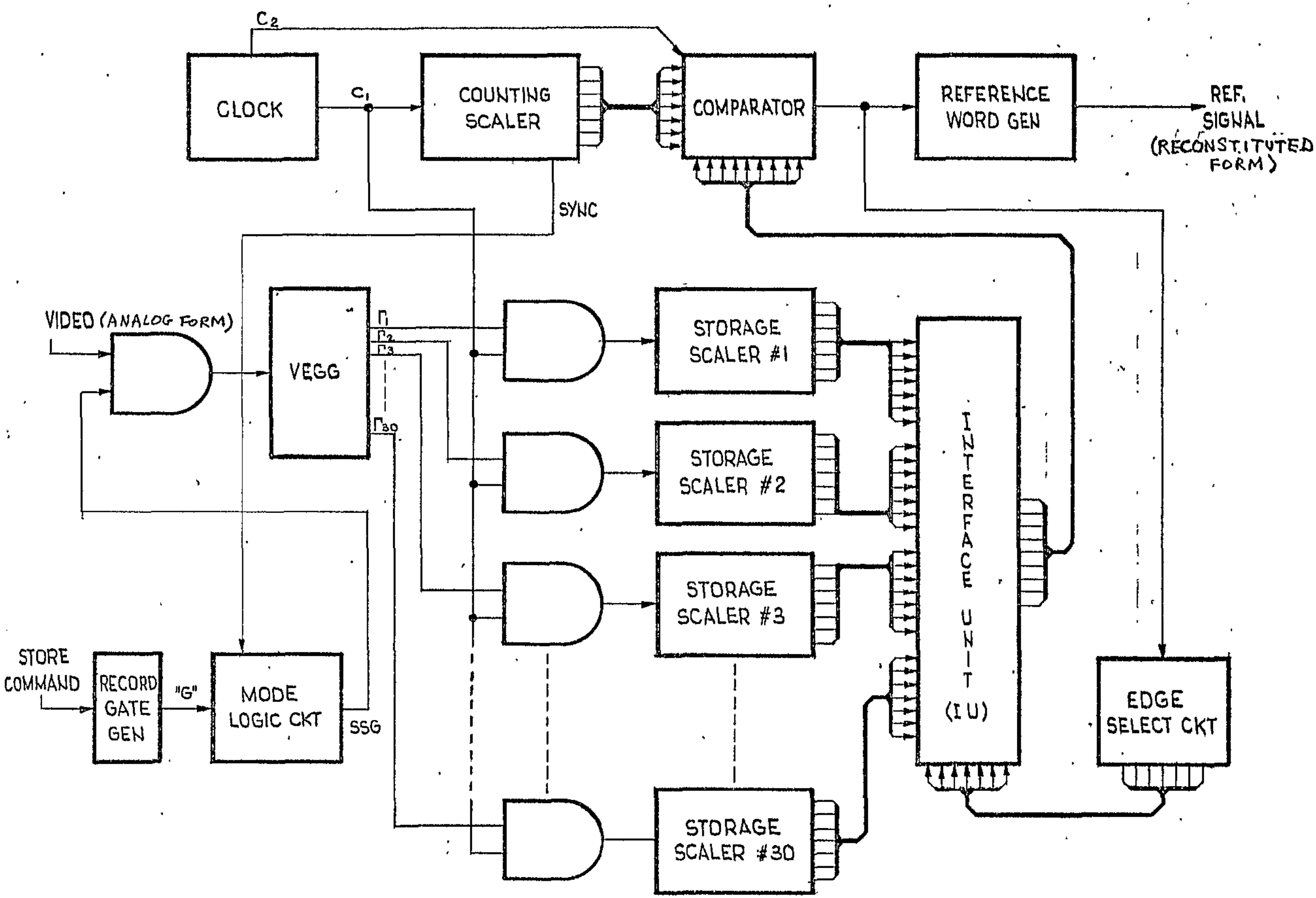

Figure 1. Parallel-Entry, Solid-State Memory. Analog In - Analog Out - Digital Store.

APPENDIX 2

MANPOWER HOURS EXPENDED ON PROGRAM (To 27 June 1969)

	Hours Allocated	Total Hours Expended
Task 1 - Study System Parameters		
Engineering	160	163.5
Task 2 - Study Crosstalk due to Roll		
Engineering	120	161.5
Task 3 - Study Systems for Elimination of Roll Rate Effect		
Engineering	100	184
Task 4 - Design and Fabrication of Visible Light Front End		
Engineering (including Reliability)	270	369.5
Design Engineering	80	80.5
Technician	100	108.5
Shop	120	24.75
Task 5 - Test Stand Design and Fabrication		
Engineering	120	250
Design Engineering	100	178.50
Technician	132	48.75
Shop	100	243.50
Task 6 - Test Visible Light Front End		
Engineering	170	350.25
Technician	175	154.25
Shop	100	23.5
Task 7 - Preliminary Block Diagram and Layout		
Engineering	20	16
Task 8 - Preliminary Size, Weight and Power	10	5
Task 9 - Establishment of Parameters for Interface		
Engineering (including Reliability)	40	25
Task 10 - Final Report		
Engineering and Technical Writing	240	156

APPENDIX 3

OPTIMUM OPTICAL DESIGN WITH OBLONG* FIELDS OR DETECTORS

M. G. Dreyfus, Chief Scientist

INTRODUCTION

The BAI satellite yaw sensor has a $5^{\circ} \times 5^{\circ}$ field of view divided into twenty $1/4^{\circ} \times 5^{\circ}$ adjacent strips. Each strip is viewed by one infrared detector. The commonly available infrared detectors are either squares or rectangles with an aspect ratio close to unity. The instantaneous field viewed by each detector has an aspect ratio of 1:20.

We will show in the following discussion that the optimum system aperture stop under these operating conditions is a rectangle with an aspect ratio of 20:1 in the case of a square detector (and close to 20:1 with a detector aspect ratio close to unity) and will derive a general theorem governing the optical design of systems with rectangular stops.

DISCUSSION

Assume an optical system consisting of a series of p thin lenses (or mirrors) in air with one lens located at each aperture stop or field stop alternately: assume that this lens system is terminated by an anamorphic radiation-condensing system** optimized to deliver the flux to a radiation detector; assume that the field of view of the optical system consists of an angle ϕ_1 in the horizontal plane and an angle θ_1 in the vertical plane as viewed from the center of the first thin lens; let the linear dimensions of the m^{th} lens be X_m in the horizontal plane and Y_m in the vertical plane; define the aspect ratio r_m of the m^{th} lens as $r_m = Y_m/X_m$. Similarly define the aspect ratio r_D of the detector D as $r_D = Y_D/X_D$.

<u>Theorem</u>: $r_1 r_2 = r_D$ for $p \geq 1$

<u>Proof</u>: The image generated by a thin lens in air can be delineated by projection of straight lines through the geometric center of the lens from the edges of the field of view in the object plane to the corresponding image points in the conjugate focal plane. These straight lines form similar triangles satisfying the following relationships:

$$\frac{Y_1}{X_1} = \frac{\theta_2}{\phi_2} = \frac{Y_3}{X_3} = \frac{\theta_4}{\phi_4} = \ldots\ldots$$
$$\frac{\theta_1}{\phi_1} = \frac{Y_2}{X_2} = \frac{\theta_3}{\phi_3} = \frac{Y_4}{X_4} = \ldots\ldots \qquad (1)$$

*The term oblong here denotes an elongated shape having an aspect ratio substantially differing from unity.

**"Wedge-Immersed Thermistor Bolometer" by M. G. Dreyfus; Applied Optics, Vol. 1, pages 615-619, September 1962.

In a similar vein we have the Lagrange invariant theorem*which states that $n_i Y_i \theta_i$ is a constant at any image plane in an optical system.

$$\therefore \quad \frac{n_1 Y_1 \theta_1}{n_1 X_1 \phi_1} = \frac{n_2 Y_2 \theta_2}{n_2 X_2 \phi_2} = \cdots = \frac{n_p Y_p \theta_p}{n_p X_p \phi_p} \tag{2}$$

From Equations (1) and (2) above, we see that:

$$\begin{aligned} r_n r_{n+1} &= \frac{Y_n}{X_n} \cdot \frac{Y_{n+1}}{X_{n+1}} = \frac{\theta_{n+1}}{\phi_{n+1}} \frac{Y_{n+1}}{X_{n+1}} = \frac{\theta_{n+2}}{\phi_{n+2}} \frac{Y_{n+2}}{X_{n+2}} \\ &= \frac{Y_{n+3}}{X_{n+3}} \cdot \frac{Y_{n+2}}{X_{n+2}} = r_{n+2} \cdot r_{n+3} \end{aligned} \tag{3}$$

Assume that a radiation detector with an aspect ratio r_D and an optimized anamorphic condensing system (yielding $\theta_D = \phi_D$) are inserted in place of the $(p+1)^{st}$ lens (i.e., at the next focal plane after the plane of the p^{th} lens). Then the anamorphic condensing system is located at the stop plane numbered $(p + 1)$ and the detector D is located at the stop plane numbered $d = p + 2$.

$$\text{If } p \geq 1 \text{ (i.e., } d \geq 3) \text{ then } (r_{d-2})(r_{d-1}) = \frac{n_D Y_D \theta_D}{n_D X_D \phi_D} = r_D \tag{4}$$
$$= \frac{n_1 Y_1 \theta_1}{n_1 X_1 \phi_1} = r_1 r_2$$

$$\therefore \quad r_1 r_2 = r_D$$

CONCLUSION

The above discussion shows that for maximum sensitivity, the asymmetry of one optical stop must be compensated by the asymmetry of another stop, and that maximum sensitivity in an electro-optical instrument with an oblong field of view requires the use of compensating oblong lenses and/or an oblong detector.

In particular, the rectangular shape of the primary mirror used in the BAI satellite yaw sensor is a well-engineered example of the general principles of compensating stop asymmetries discussed above.

---

*"The Principles of Optics" by A. C. Hardy and F. H. Perrin; McGraw Hill Book Company, N.Y., 1932; see pages 43 and 93.